This is to certify that the
thesis entitled

POPULATION AND SAMPLE BURNED AREA ANALYSES FOR NEAR LIMIT FLAMES IN A SIMULATED LOW GRAVITY ENVIRONMENT OVER THIN CELLULOSIC FUELS

presented by

KARIN LAKSMI ADITJANDRA

has been accepted towards fulfillment
of the requirements for the

M.S. degree in Mechanical Engineering

Major Professor's Signature

September 15, 2005

Date

POPULATION AND SAMPLE BURNED AREA ANALYSES FOR NEAR LIMIT FLAMES IN A SIMULATED LOW GRAVITY ENVIRONMENT OVER THIN CELLULOSIC FUELS

By

Karin Laksmi Aditjandra

A THESIS

Submitted to
Michigan State University
in partial fulfillment of the requirements
for the degree of

MASTER OF SCIENCE

Department of Mechanical Engineering

2005

ABSTRACT

POPULATION AND SAMPLE BURNED AREA ANALYSES FOR NEAR LIMIT FLAMES IN A SIMULATED LOW GRAVITY ENVIRONMENT OVER THIN CELLULOSIC FUELS

By
Karin Laksmi Aditjandra

The National Aeronautical and Space Administration (NASA) Glenn Research Center in Cleveland, Ohio, has been conducting combustion research in a microgravity environment in order to increase space mission fire safety. The research program ATHINA (Analysis of Thermodiffusive and Hydrodynamic Instabilities in Near-extinction Atmospheres) was a flight definition project related to that mission. Before this research program was to be sent to the International Space Station (ISS) for further work ATHINA had to meet specific scientific requirements. To fulfill the requirements, many earth bound experiments were conducted in the NASA microgravity facilities (Drop Towers) and the MSU microgravity simulator called the SMFT. The results of these experiments were studied in this thesis.

The experimental flamelet study conducted at MSU produced results similar to and compatible with the NASA facility. Flamelet propagation on a cellulosic fuel sample is a form of fuel rich combustion. Flamelets propagate at a nearly constant rate over the sample. The flamelet spread rate is proportional to the velocity of the oxygen supply. To reach a steady state (a condition when flamelet continues to propagate indefinitely) it is required that at least half of the total flamelet population be "productive". The flamelet population study included the development of a computer program to simulate the cumulative population of flamelets using biological population measures and the logistic model.

To Gabriel, Hyacintha,

Paulus, and Antonius

for their love.

ACKNOWLEDGEMENT

I would like to thank my academic advisor Dr. Indrek Wichman, for all his insights, guidance and support throughout my graduate years. I also thank him for giving me the chance to work on this excellent opportunity with NASA.

I would also like to thank Dr. Sandra Olson and Dr. Fletcher Miller of NASA Glenn Research Center at Lewis Field for all the advices and assistance in this project.

Lastly, I would like to thank my family and Bryan Burkhart for their love, support and assistance. Thanks to all my fellow graduate students for their support and assistance.

TABLE OF CONTENTS

LIST OF TABLES viii

LIST OF FIGURES ix

NOMENCLATURE xiv

CHAPTER 1
INTRODUCTION 1
1.1 Experiments in the MSU Microgravity Facility 3
1.2 Experimental Data 6
1.3 Flamelet Study 8

CHAPTER 2
PREVIOUS WORK AND LITERATURE REVIEW 10
2.1 Overview 10
2.2 MSU Flame Rig 10
2.3 Simulated Microgravity Flame Tunnel 13
2.4 Experimental Procedure 16
2.5 Literature Review 17

CHAPTER 3
FLAMELET POPULATION ANALYSIS 21
3.1 Background 21
3.2 Approach 22
3.3 Flamelet Population 24
3.3.1 Experiments in the Normal Position 24
3.3.2 Experiments in the Inverted Position 28
3.3.3 Flamelet Population Summary 30
3.4 Flamelet Lifetime 35
3.4.1 Experiments in the Normal Position 35
3.4.2 Experiments in the Inverted Position 37
3.4.3 Flamelet Lifetime Summary 39
3.5 Flamelet Census 43
3.5.1 Experiments in the Normal and Inverted Positions 43
3.5.2 Flamelet Census Summary 46

CHAPTER 4
FLAMELET BIFURCATION ANGLE ANALYSIS 50
4.1 Background 50
4.2 Approach 51
4.3 Results and Discussion 52
4.3.1 Experiments in the Normal Position 53

4.3.2 Experiments in the Inverted Position....53
4.3.3 Summary of Bifurcation Angles....54

CHAPTER 5
FUEL SAMPLE BURNED AREA ANALYSIS....56
5.1 Overview....56
5.2 Fuel Sample Area Burned Fraction....56
5.2.1 Approach....56
5.2.2 Experiments in the Normal Position....57
5.2.3 Experiments in the Inverted Position....60
5.2.4 Flamelet Region in the Burned Fraction Curve....63
5.3 Flamelet Spread Rate....64
5.3.1 Approach....64
5.3.2 Experiments in the Normal Position....65
5.3.3 Experiments in the Inverted Position....67
5.4 Per-Flamelet Heat Release Across Sample....68
5.4.1 Approach....68
5.4.2 Experiments in the Normal Position....69
5.4.3 Experiments in the Inverted Position....70
5.5 Oxygen Consumption Rate....71
5.5.1 Approach....71
5.5.2 Experiments in the Normal Position....74
5.5.3 Experiments in the Inverted Position....75
5.5.4 Discussion....76
5.6 Stoichiometric Ratio....78
5.6.1 Approach....78
5.6.2 Results and Discussion....79
5.7 Flamelet Power....80
5.7.1 Approach....80
5.7.2 Results and Discussion....81

CHAPTER 6
FLAMELET ANALYSIS....82
6.1 Background....82
6.2 Approach....83
6.3 Average Number of Flamelets....85
6.4 Flamelet Diameters, Gap Between Flamelets, and Quench Distance....87

CHAPTER 7
POPULATION MODEL....88
7.1 Background....88
7.2 MATLAB Code....90
7.3 Factors of Accuracy....90
7.4 Time Lag....93
7.5 Vibration Analyses....96
7.6 Temporal Perturbation of the Population Equation....98

7.7 Comparison with Experimental Data 102
7.8 Carrying Capacity and Time Lag 103
7.9 Intrinsic per Capita Growth Rate 107

CHAPTER 8
FLAMMABILITY MAP AND MODIFICATION TO THE APPARATUS 108
8.1 Flammability Map 108
8.2 Modification on the SMFT 109

CHAPTER 9
CONCLUSION AND FUTURE WORK 111

APPENDIX A 114

APPENDIX B 116

BIBLIOGRAPHY 124

LIST OF TABLES

Table 1. List of tests analyzed for various tunnel heights and final air velocities 7

Table 2. Average flamelet population, bifurcation rate, and extinction rate 31

Table 3. Average flamelet lifetime for mothers, infants, spinsters, and survivors 39

Table 4. Summary of flamelet census for both normal and inverted tests 47

Table 5. Summary of the average bifurcation angles for experiments in the normal and inverted positions at various tunnel heights and final air velocities 55

Table 6. Input variables to predict the oxygen consumption rate 74

Table 7. Summary of predicted unconsumed oxygen rate 77

Table 8. Summary of the average global stoichiometric ratio 80

Table 9. Summary of flamelet power 81

Table 10. Summary of flamelet diameters, gap spacing, and quench distance 87

Table 11. Error norm table 92

Table 12. Sample calculations of the population equation 94

Table 13. Log decrement 98

Table 14. Average carrying capacity 105

Table 15. Average time lag 106

LIST OF FIGURES

Images in this thesis are presented in color

Figure 1. Side view sketch of the MSU microgravity facility test section tunnel. 3

Figure 2. Flame-front to flamelets transformation. 4

Figure 3. Example of flamelets finger-like patterns. 5

Figure 4. Terminology diagram of the new naming arrangement of the test. 8

Figure 5. MSU Flame Rig. 11

Figure 6. MSU Flame Rig airflow system diagram 11

Figure 7. MSU Flame Rig/SMFT test section setup. 13

Figure 8. Simulated Microgravity Flame Tunnel (SMFT). 14

Figure 9. SMFT airflow system diagram 16

Figure 10. Flammability Map [4]. 18

Figure 11. Flamelet bifurcation, starting with one flamelet and ending with two. 22

Figure 12. Flamelet extinction, starting with three flamelets and ending with two. 22

Figure 13. Example of flamelet population plot with 3 mm tunnel height in normal position of the test facility. 25

Figure 14. Example of flamelet population plot with 4 mm tunnel height in normal position of the test facility. 26

Figure 15. Example of flamelet population plot with 5 mm tunnel height in normal position of test facility. 26

Figure 16. Example of flamelet population plot with high extinction rate in the middle of the experiment. 27

Figure 17. Fingering pattern of a test with high extinction rate in the middle of the experiment. 28

Figure 18. Example of flamelet population plot with 3 mm tunnel height in inverted position of the test facility. 29

Figure 19. Example of flamelet population plot with 4 mm tunnel height in inverted position of the test facility. 29

Figure 20. Example of flamelet population plot with 5 mm tunnel height in inverted position of the test facility. 30

Figure 21. Average number of flamelet population versus final airflow test velocity. 32

Figure 22. Bifurcation rate versus extinction rate. 32

Figure 23. Number of flamelets for various tunnel heights with the same final air velocity (2.5 cm/s for normal position and 3.5 cm/s for inverted position). 33

Figure 24. Plot of number of flamelets versus the product of tunnel height and air velocity. 34

Figure 25. Example of flamelet lifetime plot with 3 mm tunnel height in normal position of the test facility. 35

Figure 26. Example of flamelet lifetime plot with 4 mm tunnel height in normal position of the test facility. 36

Figure 27. Example of flamelet lifetime plot with 5 mm tunnel height in normal position of the test facility. 36

Figure 28. Example of flamelet lifetime plot with 3 mm tunnel height in inverted position of the test facility. 37

Figure 29. Example of flamelet lifetime plot with 4 mm tunnel height in inverted position of the test facility. 38

Figure 30. Example of flamelet lifetime plot with 5 mm tunnel height in inverted position of the test facility. 38

Figure 31. Average lifetime for flamelet mothers versus final air flow velocity. 40

Figure 32. Average lifetime for flamelet infants versus final air flow velocity. 40

Figure 33. Average lifetime for flamelet spinsters versus final air flow velocity. 41

Figure 34. Average lifetime for flamelet survivors versus final air flow velocity. 41

Figure 35. A fingering pattern of a test with higher lifetime of flamelet spinsters. 42

Figure 36. A fingering pattern of a test with higher lifetime of flamelet survivors. 43

Figure 37. Example pie charts for results of experiments in the normal position of test facility with tunnel heights of 3, 4, and 5 mm. 44

Figure 38. Example pie charts for results of experiments in the inverted position of test facility with tunnel heights of 3, 4, and 5 mm. 45

Figure 39. Percentage of flamelet mothers versus final air flow velocity. 47

Figure 40. Percentage of flamelet infants versus final air flow velocity. 48

Figure 41. Percentage of flamelet spinsters versus final air flow velocity. 49

Figure 42. Fingering pattern with tunnel height of 5 mm and final air velocity of 2.5 cm/s in the normal position of the test facility. 50

Figure 43. Fingering pattern with tunnel height of 3 mm and final air velocity of 5.5 cm/s in the normal position of the test facility. 50

Figure 44. Picture of fingers with different bifurcation angles. 51

Figure 45. Measuring angle of bifurcation. 52

Figure 46. Bifurcation angle versus tunnel height for normal position of test facility 53

Figure 47. Bifurcation angle versus tunnel height for inverted position of test facility. 54

Figure 48. Average bifurcation angle versus tunnel height. 55

Figure 49. Measuring fuel sample burned area. 57

Figure 50. Area fuel burned fraction plot that represents results in the normal position of the test facility with tunnel heights 3, 4, and 5 mm and various final air velocities. 58

Figure 51. Three regions of test RampDown_5mm_26.7-2.5_8.07(6)c. 59

Figure 52. Burned fraction for experiments in the normal position. 60

Figure 53. Fuel area burned fraction that represents the results in the inverted position of the test facility with tunnel heights 3, 4, and 5 mm and various final air velocities. 61

Figure 54. Average fuel burned fraction for experiments in the inverted position with tunnel heights 3, 4, and 5 mm and various final air velocities. 62

Figure 55. Burned fraction with its fingering pattern superposed on top. 64

Figure 56. Measuring flamelet spread rate. 65

Figure 57. Flamelet spread rate for experiments in normal position of test facility with various tunnel height and final air velocities. 66

Figure 58. Flamelet spread rate for experiments in the inverted position of the test facility for various tunnel heights and final air velocities. 67

Figure 59. Per-flamelet heat release per unit length across the sample that represents the results in the normal position of the test facility for various tunnel heights final air velocities. 69

Figure 60. Per-flamelet heat release per unit length across the sample that represents the results in the inverted position of the test facility for various tunnel heights final air velocities. 70

Figure 61. Predicted oxygen consumption rate plot that represents the results in the normal position of the test facility with various tunnel heights and final air velocities. 74

Figure 62. Predicted oxygen consumption rate plot that represents the results in the inverted position of the test facility with various tunnel heights and final air velocities. 75

Figure 63. Predicted unconsumed oxygen rate with unusual occurrence. 78

Figure 64. Fingering pattern segment showing the quantities q, g, and r (N = 7 and W* = 17.8 cm). 84

Figure 65. Line following process. 84

Figure 66. Average number of flamelets for 3 mm tunnel height. 85

Figure 67. Average number of flamelets for 4 mm tunnel height. 86

Figure 68. Average number of flamelets for 5 mm tunnel height. 86

Figure 69. Non-dimensional population with delta = 0.1, 0.01 and 0.001 using Euler, Modified Euler and 4th Order Runge-Kutta methods. 92

Figure 70. Population with time lag = 0.9 and 1.0 95

Figure 71. Population with time lag = 1.2 and 2 95

Figure 72. Settling time peak. 97

Figure 73. Population with ε = 1.5 and 1.0. 99

Figure 74. Population with ε = 0.5 and 0.01. 100

Figure 75. Population with $\omega = \pi/4$ and $\pi/2$. 101

Figure 76. Population with $\omega = \pi$ and $3\pi/2$. 101

Figure 77. Population experimental data. 102

Figure 78. Experimental data with its numerical solutions 103

Figure 79. Flammability Map. 108

Figure 80. Diagram of the new airflow system with dehumidifier. 109

Figure 81. New airflow system with dehumidifier. 110

Figure A1. Flame spread rate [9]. 114

NOMENCLATURE

Arabic

a(t)	Bifurcation as function of time
A	Fuel burned area (m^2)
b(t)	Extinction as function of time
c_p	Constant-pressure specific heat (J/kg*K)
D	Diffusivity (m^2/s)
$\frac{dA}{dt}$	Fuel burned area rate (m^2/s)
d_f	Fractal dimension
f	Fraction burned or frequency (Hz)
g	Gap between flamelets (m)
h_f^o	Enthalpy of formation (J/kg)
H	Enthalpy (J/kg)
H^*	Oxygen consumed height (m)
L	Fuel burned segment (m)
m	Mass (kg)
$\dot{m}$	Mass flow rate (kg/s)
MW	Molecular weight (kg/kmol)
N	Number of particle in a cluster or number of flamelets
$\dot{O}_2$	Oxygen consumption rate (kg/s)
q	Quench distance (m)
$\dot{q}$	Flamelet instantaneous heat release (J/s)

Q	Flamelet energy production (J)
r	Clutter's radius or flamelet radius (m) or intrinsic per capita growth rate (s^{-1})
$\Re$	Ratio of the fuel burned area and the number of flamelet
t	Time (s)
T	Temperature (K)
u	Average flamelet spread rate (m/s)
u(t)	Flamelet population as function of time
v	Velocity (m/s)
W	Sample width (m)
W^*	Oxygen consumed width (m)
x	Distance (m)
Y	Mass fraction

Greek

β	Stoichiometric oxygen coefficient
δ	Log decrement of two consecutive peaks
Δh	Enthalpy change (J/kg)
Δx	Increment (m)
ε	Perturbation variable
κ	Carrying capacity
ρ	Density (kg/m^3 or kg/m^2)
$\rho(t)$	Non-dimensional population as function of time
τ	Time lag (s)

ω	Frequency (radiant)
ζ	Damping ratio

Subscripts

∞	Ambient
1	At distance x = 0
avg	Average value
A	Air
$C_6H_{10}O_5$	Cellulose
f	Flame
F	Fuel
in	Inward direction
O_2	Oxygen
s	Surface
o	Initial condition
x	At distance x

CHAPTER 1
INTRODUCTION

Spacecraft fire safety is a very important issue for the National Aeronautical and Space Administration (NASA). To increase spacecraft fire safety, NASA Glenn Research Center at Lewis Field in Cleveland, Ohio, has been developing a research program in microgravity combustion. This research is important and challenging because fire does not behave in the same manner when it is in a 1-g (9.81 m/s^2) as it does in a microgravity environment. ATHINA, an abbreviation for Analysis of Thermodiffusive and Hydrodynamic Instabilities in Near-extinction Atmospheres, is a project conducted by NASA Glenn Research Center. This project is a study of the propagation of an unstable flame over a fuel in a low oxygen microgravity environment. In a low oxygen environment, an unstable flame breaks into small separate flames that are called flamelets. Flamelets are near-extinction flames that propagate in a unique style resulting in finger-like patterns. Flamelets are hard to detect and their presence is dangerous because when the environment becomes favorable, (i.e. oxygen concentration increases, or airflow into the region increases, etc.) flamelets can transform into flames again, resulting in a fire.

This thesis performs "behavioral" studies of flamelet, and experimental data collection is thus required. To perform experimental research in microgravity combustion on earth, NASA Glenn Research Center has two microgravity facilities that are known as Drop Towers. The first drop tower is capable of creating a 10^{-4}-g environment for 2.2 seconds; and the second drop tower is capable of creating a 10^{-5}-g environment for 5 seconds. Compared to the 10^{-6}-g environment in the space, the 10^{-4}-g and 10^{-5}-g environments created in drop towers are considered quite good. These facilities though,

require a group of experienced staff and engineers as well as heavy machines and hardware to perform experiments in the drop towers. NASA staff can conduct three experiments on average per day in the 2.2-second drop tower. Moreover, NASA staff can conduct one experiment on average per day in the 5-second drop tower. Because of this limitation, NASA, along with the Michigan State University combustion group has come up with a new idea to build an apparatus that is able to simulate a microgravity environment that doesn't require a group of experienced staff and heavy machines every time performing an experiment.

The MSU combustion group had designed and constructed an apparatus that is capable of simulating a microgravity environment by suppressing the buoyant force in narrow width of the low-speed wind tunnel. This technique is adopted from an apparatus that is known as the Hele-Shaw cell. The apparatus was reconstructed; therefore it is capable of conducting experiments in the inverted position.

The apparatus was designed carefully so that the tunnel height is adjustable over a small range of approximately 1 mm to 7 mm. As shown in Figure 1, the tunnel height is the distance from the quartz top window to the sample and from the sample to the copper backing. For this thesis, the tunnel heights above and below the sample were the same for each experiment. In [10] it was estimated that within 1 mm to 7 mm range the effect of the buoyant force may be neglected. The range of the tunnel height was estimated by calculating the Raleigh number, Ra, which was calculated based on the Prandtl number, Pr, and Grashof number, Gr, for a heated plate; even though the heating provided by the flamelets in the experiments was localized. Nevertheless, as a start the heated-plate calculation of Ra shall be used until a better estimate of the gravitational influence can be

devised (including upside-down tests). When the Rayleigh number is critical, the atmosphere becomes thermo-diffusively and hydro-dynamically unstable.

A side view sketch of the MSU microgravity facility test section tunnel is shown in Figure 1. The heights above and below the sample were always equal. For this thesis, the heights for each side of the sample were either 3-3, 4-4 or 5-5 mm. The air flows in the opposite direction of the flame. In addition, the MSU microgravity apparatus is equipped with a controllable airflow system. This airflow system is capable of producing a low airflow rate to establish a near extinction atmosphere.

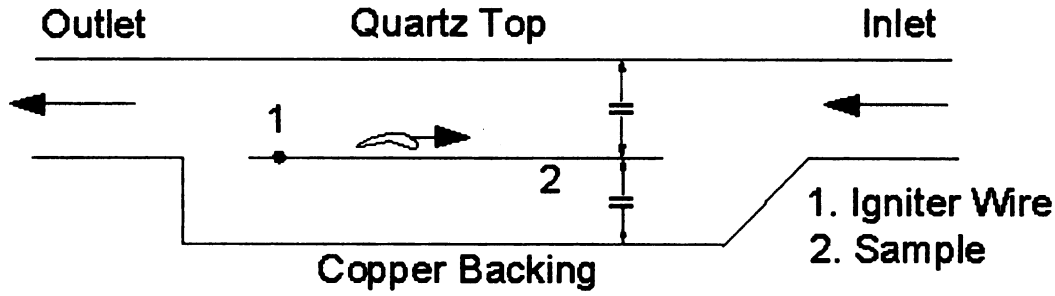

Figure 1. Side view sketch of the MSU microgravity facility test section tunnel.

1.1 Experiments in the MSU Microgravity Facility

There are many experiments conducted in the MSU microgravity facility both in the normal and in the inverted positions of the test facility. One example of the experimental sequence from one of the tests conducted in the MSU microgravity apparatus can be seen in the set of pictures in Figure 2. There are seven pictures that show the transformation of a flame-front into flamelets until the end of the test. Picture A shows when the ignition took place. Picture B shows that a linear flat flame-front occurred as a result of the ignition. The flame-front would travel and consume the sample in the direction opposite to the airflow, which came from the right toward the left in Figure 2. The flame-front thus

propagated from left to right. As soon as a flat flame-front was obtained, the flow control system was programmed to reduce the airflow rate. The result can be seen in picture C. This picture shows that the intensity of the flame-front diminished due to the airflow reduction. The lack of oxidizer forced the flame-front to become unstable and it would start to bulge at some points along the flame-front while regressing at others. These

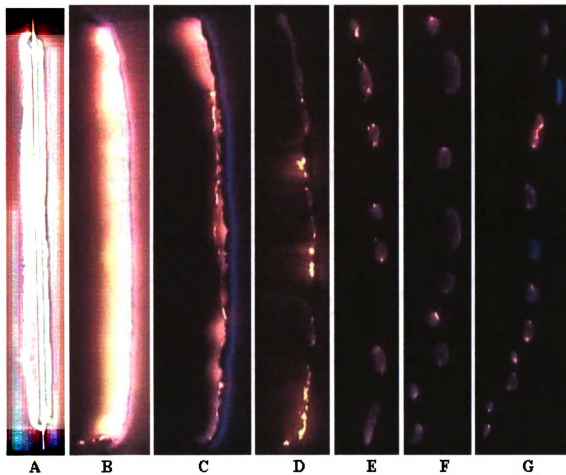

Figure 2. Flame-front to flamelets transformation.

bulges would eventually split into several small flamelets as shown in picture D. Picture E shows the initial distinct and separate flamelets. In this case there were seven initial flamelets. Picture F shows a sample of the flamelet propagation. As can be seen from

pictures E to F, the number of flamelets had increased from seven to nine and the spaces between flamelets had changed. Essentially, the changes occurred because of the flamelet bifurcations and extinctions. Notice in picture F, there are two slightly larger flamelets, numbers two and four from the top. These are flamelets that were about to bifurcate. Picture G shows the end of the experiment, when the flamelets reached the end of sample. In this picture the number of flamelets had increased substantially. This may happen because of the flow change effect at the end of the sample. The finger-like patterns, results of flamelet propagation, are shown for the burned-out sample in Figure 3.

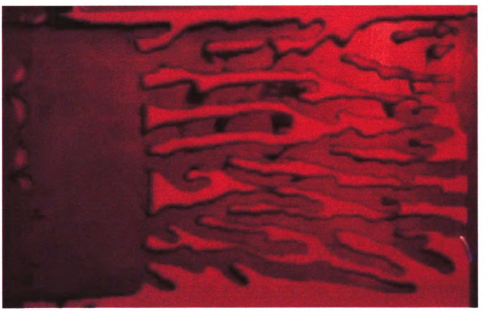

Figure 3. Example of flamelets finger-like patterns.

Since the main objective of this thesis is to study the behavior of flamelets, the finger like patterns such as shown in Figure 3 are very valuable. A list of the total number of experiments used for this thesis is given in the next section.

1.2 Experimental Data

All of the experiments that were conducted in the MSU microgravity facility were recorded with a digital camera. From the camera, each video file was transferred, compressed and saved as *.avi* file in a computer. For this thesis, the experiments employed were those with flamelets both in the normal and inverted positions of the test facility. The normal position is when the apparatus is right side up: that is, when the quartz top is at the upper side. The inverted position is when the apparatus is rotated 180 degrees, so that the quartz top is at the bottom side. Flamelets occur mostly in tunnel heights of 3, 4 and 5 mm with different low final air velocity ranges for different tunnel height. These experimental data were employed in the subsequent discussion in this thesis. Table 1 in the following page outlines the total number of tests for each tunnel height with different air velocities. The total number of tests that were analyzed is 49. Each of these 49 tests was performed by different laboratory personnel at different time, before, and after the reconstructions and modifications.

Each of these tests is named and throughout this thesis, there are two types of naming arrangements. The t-35-25c and t-40-25c are the only two tests use the old naming arrangement, and the remaining tests use the new naming arrangement. The new naming arrangement began when the MSU microgravity apparatus was modified. The old naming arrangement is short and simple but it is difficult to understand the conditions of the experiment. Conversely, the new naming arrangement is longer but it is very easy to understand the conditions of the experiment. It mentions the type of the experiment, the position of the apparatus, the tunnel height, the air velocity range, and the deceleration rate.

Table 1. List of tests analyzed for various tunnel heights and final air velocities

Position	Tunnel Height (mm)	Air Velocity (cm/s)	Number of Tests Analyzed
Normal	3	2.5	1
		3.5	1
		5.5	4
		12.5	1
	4	2.5	4
		3.0	6
		3.5	2
		4.0	1
		5.0	2
	5	2.5	2
		3.5	1
		5.0	2
		7.5	1
		10.0	1
Inverted	3	3.5	1
		4.5	2
		5.1	1
		8.5	1
	4	2.5	1
		3.0	3
		3.5	2
		4.0	1
		5.0	1
		7.5	1
	5	2.5	3
		3.5	1
		4.5	1
		5.0	1

To better explain the terminology of the new naming arrangement, consider Figure 4 on the following page. The terminology of the old naming system is as follows. The letter 't' is an abbreviation for the word 'test'. The number in the middle following letter 't' is the test series number. The last two numbers are the fuel type and the tunnel height. The letter 'c' is to indicate that the video file has already been compressed. The fuel type that has been used for all these experiments was Whatman™ 44 research grade ash-less filter paper.

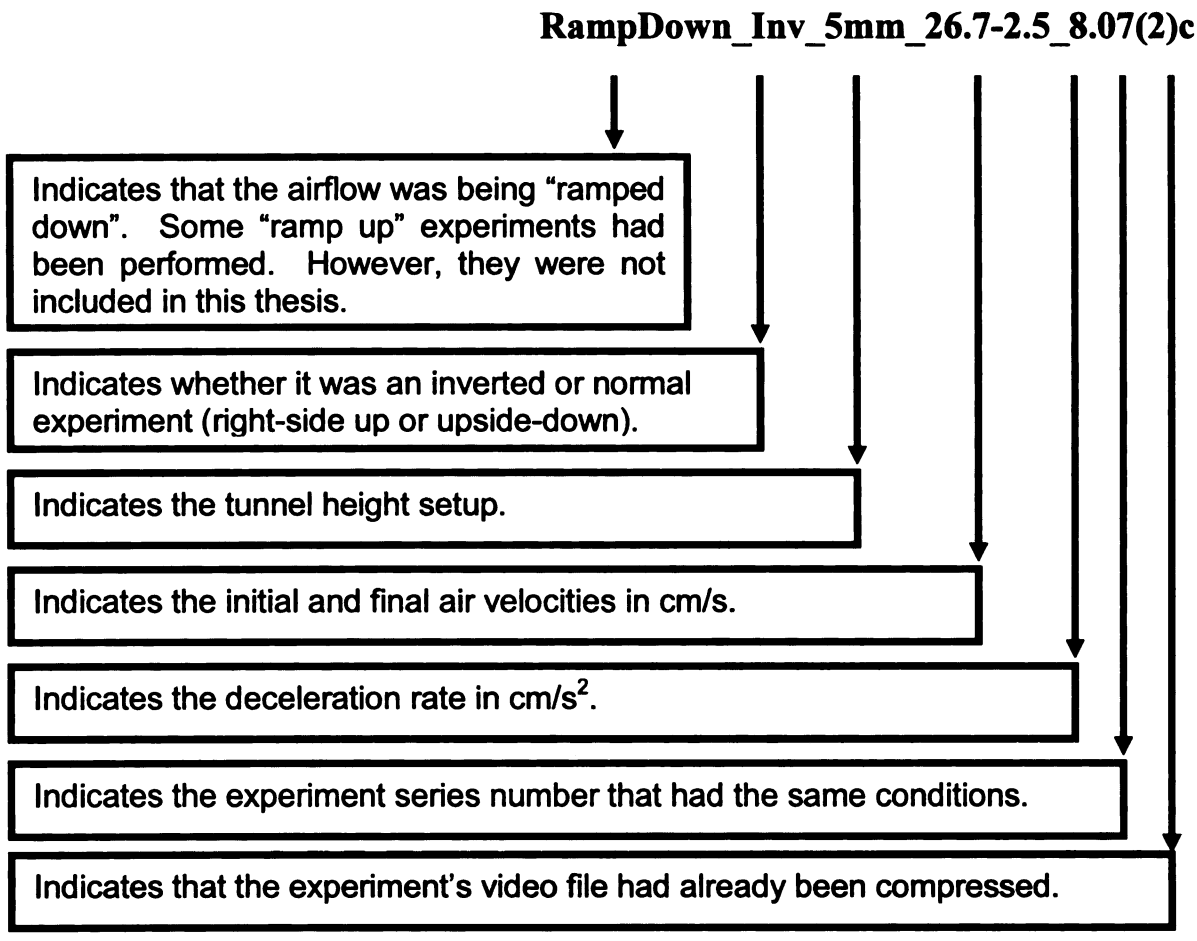

Figure 4. Terminology diagram of the new naming arrangement of the test.

1.3 Flamelet Study

This thesis focuses on the flamelet "behavior". This flamelet study includes detailed examination of the flamelet population. It consists of: (1) evaluations of the bifurcation and extinction rates of the flamelet, (2) flamelet number count or census data, and (3) flamelet lifetime measurements. The flamelet population examination will be discussed in Chapter 3. Chapter 4 discusses the flamelet bifurcation angle using the fingering pattern.

Another study that employs the fingering patterns of the flamelet is the sample area burned measurement. This measurement is important because the sample area burned serves as an estimate for the amount of oxygen consumed by the flamelet during combustion. This study can also estimate the flamelet energy production as well as the air-to-fuel ratio of the reaction. In addition to the estimation of the oxygen consumption rate, the flamelet spread rate was measured. The sample area burned measurement study is presented in Chapter 5.

Chapter 6 discusses a study that accounts for the size of the flamelets as well as other measurable properties. This analysis includes measurements of the gaps between flamelets, and the quenching distance, as well as the flamelet diameter.

The flamelet population study continues by developing a computer program that models the flamelet "population demographics". The model uses biological measures and the logistic model. The solutions are found quantitatively using the numerical solution for a differential equation. Some of the results will be compared to the study that was done at NASA. This topic will be covered in Chapter 7. Lastly, Chapter 8 discusses the flammability map of the MSU microgravity apparatus as well as the addition of the dehumidifier to the MSU microgravity apparatus.

CHAPTER 2
PREVIOUS WORK AND LITERATURE REVIEW

2.1 Overview

This chapter describes the previous research efforts by the MSU combustion group on the NASA-funded ATHINA project. The first part of these efforts by the MSU combustion group was to design and construct the apparatus that produces conditions resembling those of a microgravity environment. This apparatus was called the MSU Flame Rig. The second part of the effort was to modify the apparatus such that it is able to perform experiments up side down. The modified apparatus was called the SMFT (Simulated Microgravity Flame Tunnel). The last section of this chapter discusses some related research on the opposed flow effect, microgravity combustion and branching mechanism.

2.2 MSU Flame Rig

The MSU Flame Rig was designed and constructed carefully with safety in mind. The detail of the design and construction of the MSU Flame Rig can be found in [10]. The MSU Flame Rig was constructed mostly by employing non-flammable materials such as aluminum. A picture of the MSU Flame Rig can be found in Figure 5 (picture does not show the airflow system).

The MSU Flame Rig airflow system consists of air filter, pressure regulator, rotameter, orifice and needle valve. A diagram of the airflow system can be seen in Figure 6. The airflow system allowed controllable clean air to flow from the source to the test section. Air flowed from the building air supply to a 5-micron air filter. The clean air then flowed to a pressure regulator. From the pressure regulator, air flowed through the

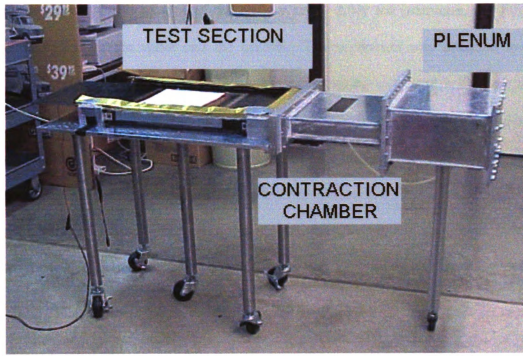

Figure 5. MSU Flame Rig.

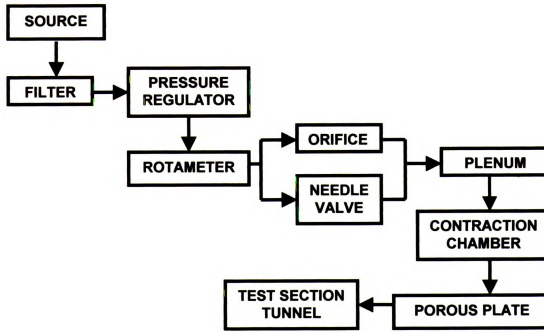

Figure 6. MSU Flame Rig airflow system diagram.

rotameter, which allows control of the airflow rate. After the rotameter, the flow was separated to the needle valve and the orifice. The separation was intended to allow accurate control of the air mass flow rate. From the needle valve and orifice, air flowed into the plenum chamber. In the plenum chamber was a 2-inch diameter pipe with holes facing the back wall. The purpose was to produce a uniform flow. From the plenum chamber, air flowed to the contraction chamber. In this section a ramp was placed for the air to be compressed, smoothed and prepared to enter the test section. Just before air entered the test section, a porous plate was located after the ramp so the air that flowed into the test section tunnel was a uniform, slug flow.

The test section tunnel of the MSU Flame Rig was designed so that the height was variable. Below the test section holder there was a set of aluminum bars and shims to adjust the tunnel height. To produce different tunnel heights, different sets of aluminum bars and shims were used. In the tunnel, attached to the bottom test section were mica strip, copper backing, and terminals to hold the igniter wire. The mica strip acted as the sample holder as well as an insulator. The copper backing acted as a heat sink to the flame. The igniter wire was designed carefully so it laid flat on the sample paper and was able to generate a flat flame front. This setup was the same setup as in the NASA's microgravity facility. A picture of the MSU Flame Rig test section setup is shown in Figure 7.

The camera stand of the MSU Flame Rig was a separate piece. It resembled a tall table where the four legs were about twice the height of the test section. On the top of the table was a bar with a screw to mount the camera. There was also a hole that is just enough for a small portion of the camera to slot into. The four sides of the camera stand were covered with a black cloth so there was no light entering during experiment. The covering

during experiments provided a maximum visual contrast of the flame, as it was difficult to see the flame in the light. Also attached to the camera stand was a red light, which was activated during experiments. The red light acted as an indicator when the airflow rate was reduced at the beginning of the test, besides being a background to obtain a better contrast of the flame.

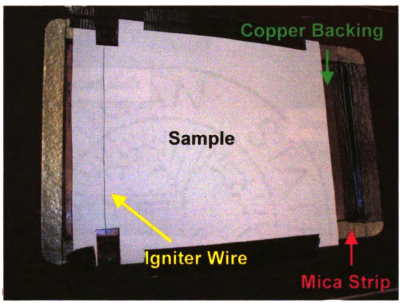

Figure 7. MSU Flame Rig/SMFT test section setup.

2.3 Simulated Microgravity Flame Tunnel

The MSU Flame Rig was modified and called SMFT, short for Simulated Microgravity Flame Tunnel [12]. SMFT was the invertible version of the MSU Flame Rig. Most part of the SMFT was the same with the MSU Flame Rig. There were five major modifications that were done to the apparatus. This first modification was the addition of a long shaft or spine that stretched from the plenum chamber to the test section tunnel. A steel frame held the body of this wind tunnel at both ends of the shaft. A picture of the SMFT can be seen in Figure 8. At one of the ends of the shaft (the one near the plenum end) was a large size bolt that locked the shaft from rotating.

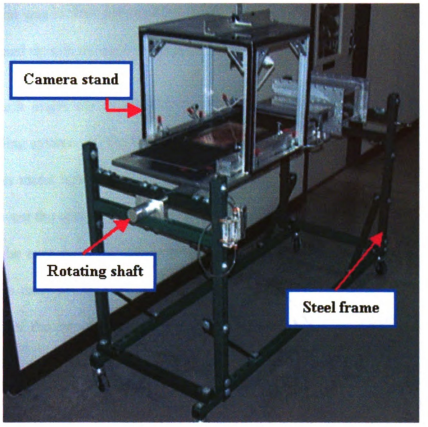

Figure 8. Simulated Microgravity Flame Tunnel (SMFT).

The second modification to the MSU Flame Rig was the spacers system that adjusts the tunnel height. The spacers system was not applicable to the invertible SMFT because they would fall when running experiment up side down. The new design to adjust the tunnel height was to replace the aluminum bars and shims using a screw system. The tunnel height can be adjusted by adjusting the screws connected to the test section holder. This screw system was also employed to adjust the distance between the sample and the copper backing.

The third modification was done on the camera stand. On the top of the camera stand crossed a bar with a screw to mount the camera. The camera stand of the old design was cut into at least half of the original length and put together in a more compact size.

The camera stand was locked with clamps on the test section holder. Therefore, when the apparatus is turned up side down, the camera is too.

The fourth major modification to the MSU Flame Rig included the quartz glass holder, the sealing system and the lighting system. In the old design, the quartz glass was held with a thin metal holder that was glued with duct tape and putty to the test section holder. To prevent the quartz glass from falling off the holder when the apparatus is turned upside down, the new design of the quartz glass holder locked it safely to the body with three clamps on each side against a strip of rubber that acts as a compression seal. The sealing system of the new design was better than the old one. In the old design, a large quantity of putty and duct tape were consumed to seal the test section. It required a long time to place the putty and duct tape for each test. In place of the putty and the duct tape, in the new design, weather strip and rubber seal were used to stop leakage. The red bulb on the MSU Flame Rig was replaced with four red LEDs on every corner of the camera stand. The red bulb in the MSU Flame Rig frequently glared on the quartz glass, which often yielded a poor photographic image. The LED display prevented glare and yielded better images.

The fifth modification was done to the airflow system. A mass flow controller was added to the airflow system of the MSU microgravity facility. The new airflow system started from the building air supply, flowed to a pressure regulator, then to a mass flow controller through a pressure relief valve. From the mass flow controller, air flowed through a series of rotameters, then to the plenum chamber. From the plenum, air flowed to the contraction chamber. From there, air flowed through a porous plate to the test

section tunnel. The mass flow controller was connected to a power supply as well as a voltmeter. The power supply was connected to a computer with a software program called LabView™ that gave commands to the power supply and voltmeter to control the airflow rate. The desired initial and final air velocities were entered in the initial and final voltages input boxes, and the desired ramp down times were entered in the times input boxes. As LabView™ works in volts, the conversion spreadsheets from volts to cm/s are available in the laboratory. The diagram of the new airflow system can be seen in Figure 9.

The pressure relief valve and the mass flow controller replaced the orifice and needle valve system. With this new airflow system, the air velocity can be automatically controlled; therefore the percent accuracy of the airflow rate is higher. Note on Figure 9, the black arrows indicate the airflow direction. The white arrows indicate the connection between two components.

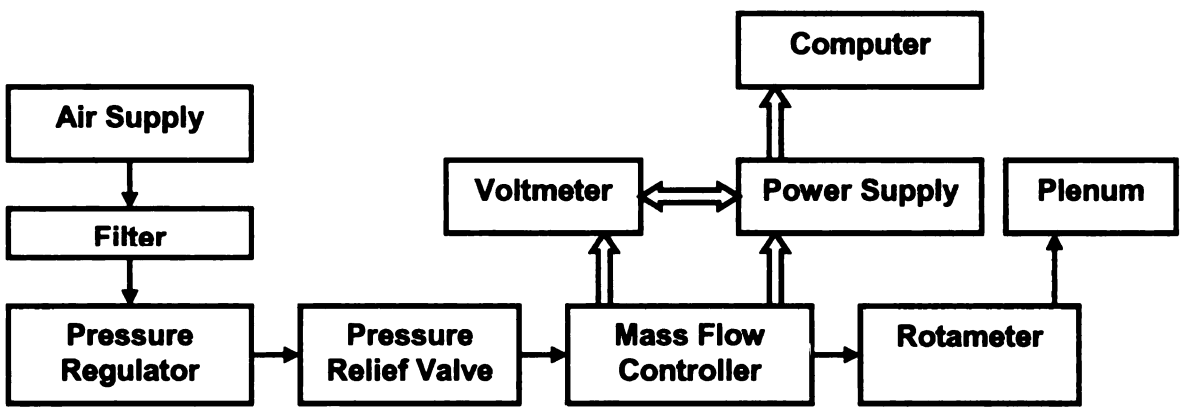

Figure 9. SMFT airflow system diagram.

2.4 Experimental Procedure

A complete experimental procedure to run the MSU microgravity apparatus can be found in [12]. The experimental setup for the SMFT was the same as for the MSU Flame

Rig (Figure 7). The following is a brief experimental procedure. First, a thin cellulosic fuel sample is glued to the mica insulator. An igniter wire is installed on one side of the fuel sample (the downstream side). The airflow approaches from the other side (upstream), so that the flame propagates in the opposite direction of the airflow. This opposed flow configuration is important to prevent any combustion products such as smoke from blocking the flames.

Before running the experiments, a camera is mounted on top of the test section tunnel to record the experiments. The initial and final voltages as well as the ramp down times are entered in the input boxes in the computer. When everything is ready, the 'Record' button on the camera is pressed and the igniter wire is turned on until a linear flat flame-front occurs. The LED is turned on. Then simultaneously 'Run' the LabView™ computer program and turn off the LED. (The LED indicates when the process of ramping down the air velocity starts.) The computer automatically reduces the airflow to the desired rate, and this occurs three seconds after the LED is turned off.

2.5 Literature Review

Many studies have been made on microgravity combustion over thin cellulosic fuels as well as the effect of opposed flow. One article by Olson [5] focuses on the testing of the forced opposed flow effect in microgravity flames, including considerations of the mechanisms of flame spread over opposed flow and the influence of oxygen concentration. A thin solid fuel (5 cm x 15 cm) with composition 99% cellulose was used for testing. The results showed that the opposed flow strongly affected the appearance of a microgravity flame. When the oxidizer velocities were low, the affect appears as a dark zone between the fuel and flame. This was an indication of fuel rich combustion. The oxygen

concentration was varied to determine in the flame spread behavior as well as the transition temperatures at which the change from fuel preheating to pyrolysis temperature occurred. The transition temperatures range from 600 K to 675 K. This temperature range was higher when the oxygen concentration was reduced.

A similar study by Olson, Ferkul and T'ien [4] focused on the microgravity flame behavior of a thin cellulosic fuel in a forced opposed flow environment. An examination of the flame behavior was carried out over a wide range of oxidizer velocities. As a result, a flammability map was obtained in the form of a bowl shape curve with three major regions, as shown in Figure 10. The first or leftmost region is the quenching region, where insufficient oxidizer caused the flame to extinguish. The second region is the flame region.

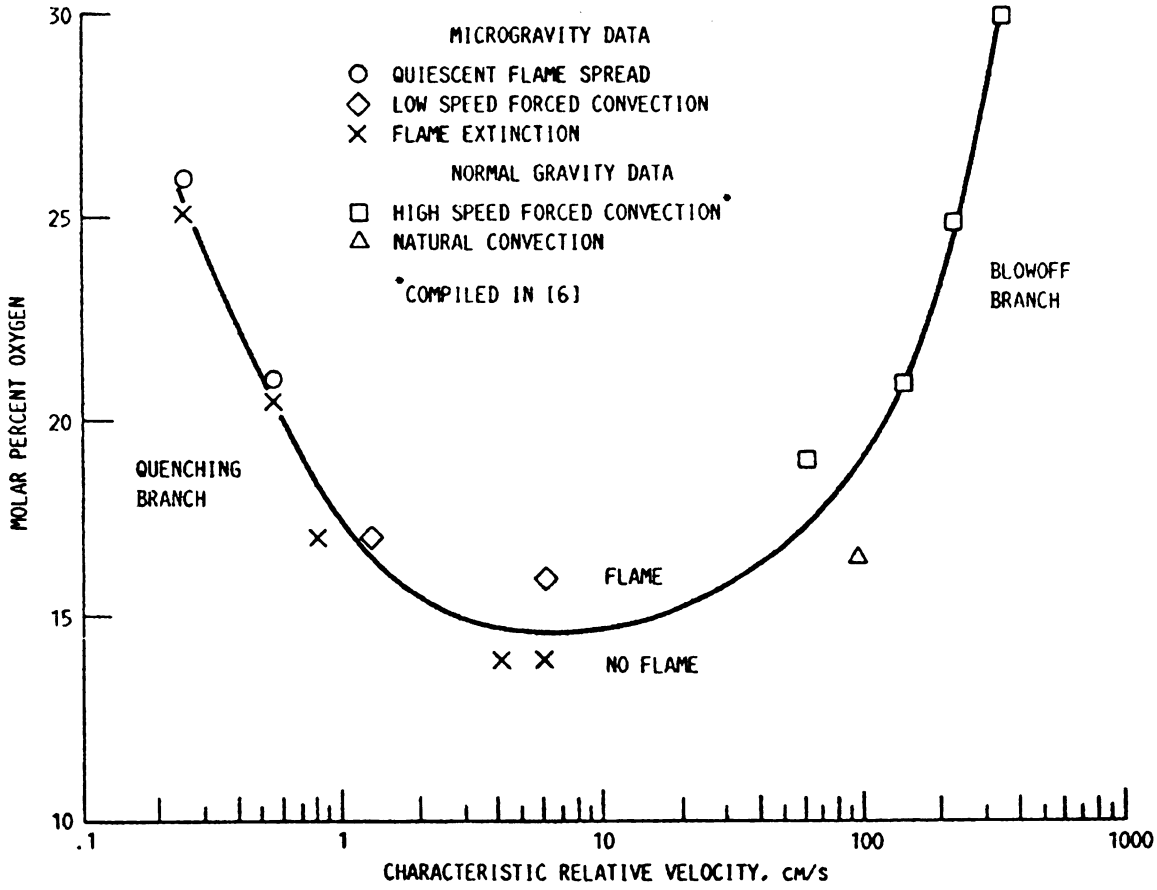

Figure 10. Flammability Map [4].

The third region is the blow-off branch. A simple way to describe blow-off is to consider a candle flame. When the oxidizer flow is too strong it can extinguish the flame. This flammability map predicted the conditions of experiments under which flamelets may occur. It is anticipated that flamelet-like behavior occurred near the quenching branch.

A work by Olson, Miller and Wichman [9] summarizes the expectations of steady state in flamelets propagation. Steady state is when the flamelets continue to propagate infinitely on a constant rate. Steady state is when the cumulative number of flamelets is constant and hence the average fraction of the sample burned is also constant. The observation time of the flamelet propagation must be longer than the average lifetime of the flamelets. Three generations sufficed although more would give better results.

Wichman studied the flame spread in a forced opposed flow environment [14]. This article includes reviews of microgravity flame spread, flame-to-smolder spread transition, and the quenched triple flame problem. In this study, theoretical models of flame spread over thin and thick fuels were described and principal references were provided.

Olson and T'ien studied the structure of low stretch diffusion flames and their extinction characteristics using PMMA samples [6]. The experiments were performed in normal gravity environment, but the understanding that was acquired may apply directly to the microgravity (or simulated microgravity) environment. Another flammability map was obtained and the quenching extinction limit occurred at low stretch with high-induced heat losses. A preliminary pre-extinction indicator is flame oscillation.

The flamelet fingering (or branching) mechanism is a phenomenon that has been observed in nature. A study by Ball [1] presents numerous branching mechanisms. In *The*

Self-made Tapestry, Ball introduces natural patterns such as tree branches, snowflakes, and branching patterns in the fluid-dynamical Hele-Shaw cell. The density of the branches can relate to the cluster radius.

$$N \propto r^{d_f} \tag{1}$$

where N is the number of particles in a cluster and d_f is the fractal dimension. Ball also introduces the instability theory of Saffman-Taylor who studied instability in viscous fluids using the Hele-Shaw cell. When the fluid-front develops bulges and the pressurized tip moves faster, this causes a finger to appear. This phenomenon is very similar to the occurrence of the flamelet fingering pattern. When the flame-front becomes instable, it starts to bulge at some points along the line, and then form flamelets.

CHAPTER 3
FLAMELET POPULATION ANALYSIS

3.1 Background

In a near limit extinction environment where there is not much oxygen, flames break apart into flamelets. Flamelets propagate in search of oxygen and leave unburned material behind that will show the formation of finger-like patterns. Some flamelets survive and produce more flamelets. Some flamelets die or extinguish because of oxygen starvation. This phenomenon makes flamelets look almost like other living things, and allows one to study flamelets using biological measures, for example, the *carrying capacity*. In biological terms, the carrying capacity is a feature that constrains populations based on environmental limitations, such as food supply or the presence of predators. In the flamelet world, the carrying capacity is limited by the oxygen supply.

When a flamelet reproduces, it is called bifurcation. On the other hand, when a flamelet extinguishes because of oxygen starvation it is called extinction. Since flamelets reproduce and die analogous to living organisms, many flamelet population analyses can be carried out. These analyses were done for both normal and inverted positions of the test section tunnel, with tunnel heights of 3, 4 and 5 mm, and various final low air velocities. These population analyses include lifetime measurement and "census data" for events such as bifurcations and extinctions.

Figures 11 and 12 are snapshots of bifurcation and extinction, respectively. The time difference between snapshots was approximately one-third of a second. As shown in the bifurcation sequence, initially a flamelet expanded, and then it broke up. The initial flamelet was considered as dead or extinguished but it produced two new flamelets. On the other hand, as seen in the extinction sequence, initially there were three flamelets. The

middle flamelet contracted, then it extinguished. Using biological terms, flamelets that bifurcate are called the *mothers* (productive flamelet), the new flamelets are called the *infants*, and flamelets that don't bifurcate but extinguish after a long period of time are called the *spinsters* (unproductive flamelet). A flamelet was considered to be an infant if the flamelet lived for less than 5 seconds. On the average, the first bifurcation for an experiment occurred 5 seconds after the formation of the flamelets. Additionally, *survivors* are flamelets that survive to the end of a given test.

Figure 11. Flamelet bifurcation, starting with one flamelet and ending with two.

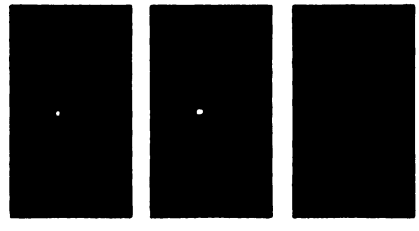

Figure 12. Flamelet extinction, starting with three flamelets and ending with two.

3.2 Approach

To analyze the flamelet population, recorded experimental data in movie video files was required. Additionally, computer software programs were used to collect data from the experimental movie. The first thing to do in collecting data was to watch the video record using Windows Media Player repeatedly and to become familiar with the flamelet distribution and the fingering patterns of the experiment. Then the video was watched repeatedly to track the propagation of the flamelets (one by one) from the beginning to the

end of the experiment, using Windows Media Player as well as TRACKER[1]. TRACKER was used to track the experiment frame by frame. In one second there are about thirty frames. Therefore, the precise time for every event that occurred in the progression of a flamelet can be tracked. Each event that occurred and its frame number were stored in a Microsoft® Excel spreadsheet.

After every event (along with its frame number) was stored in a spreadsheet, the frame numbers were sorted from the smallest to the biggest. Therefore, the events were in chronological order. The cumulative count of the flamelet population started approximately when the designated test air velocity was reached, and lasted until the flamelets reached the end of the sample or until the record was terminated.

Every time there was a flamelet bifurcation, the cumulative population was increased by one. Every time there was a flamelet extinction the cumulative population was diminished by one. With these data, a plot of the cumulative population of flamelet versus time was obtained along with the cumulative numbers of bifurcation and extinction. The rates of the bifurcation and extinction can be evaluated by dividing the respective totals by the elapsed time. Note that near the end of an experiment the bifurcation and extinction counts often increase substantially. This may happen because of the flow change at end of sample. However, the sudden increase was neglected when evaluating the bifurcation and extinction rates.

To measure the flamelet lifetime, the previously collected data for the population analysis was used. For each initial flamelet, all of the events that occurred were listed in

[1] TRACKER is a software image analysis package that was developed at NASA and is free for NASA contractors and grantees.

order. Just as before, the frame number was sorted in the order from the smallest to the biggest. Then the lifetime of a particular flamelet can be calculated. The lifetime of a flamelet was counted from when a flamelet was formed until it bifurcated or it extinguished. In other words, the flamelet lifetime was exactly the time difference between events for each flamelet. For example, consider a flamelet that initially formed at frame t_1 and bifurcated at frame t_2. Say, one of the two new flamelets extinguished at frame t_3. Therefore the lifetime of the initial flamelet is t_2-t_1, and the new flamelet has a lifetime of t_3-t_2. The flamelet lifetime was presented in bar graphs using a logarithmic scale. Each bar represents a flamelet and the height represents the lifetime.

To categorize the flamelet for census data, the flamelet lifetime data from the previous lifetime measurement were used. Based on the lifespan flamelets were categorized into mothers, infants, spinsters and survivors. For easy observation the census data were presented in the form of pie charts. In the charts, the survivors were not shown.

3.3 Flamelet Population

In the population graphs presented in this section, the x-axis (abscissa) is the approximate time from when the designated final low air velocity was reached. The left y-axis (ordinate) is the cumulative numbers of bifurcation and extinction. The right y-axis is the cumulative flamelet population. Also shown in the plots are the rates for the bifurcation and extinction as well as the average instantaneous population.

3.3.1 Experiments in the Normal Position

There are three population graphs that represent the results for tunnel heights of 3, 4 and 5 mm. These can be found in Figures 13, 14 and 15, respectively. Shown in these figures are the trend lines for bifurcation and extinction. The slopes are linear with a

parallel correlation to each other. This is an indication that the flamelet population achieved a steady state. As noted in the figures, the bifurcation and extinction frequencies were very close, and the same for all the three cases shown here. The carrying capacity approximately was the average population, as there was just enough oxygen supply for the flamelets to survive. Since the cumulative population fluctuates around the average, it can be said that the flamelet population was at the carrying capacity state. These population graphs also show that the cumulative number of population over time has an oscillatory behavior. Later in this thesis a separate chapter discusses a population model that describes the oscillation.

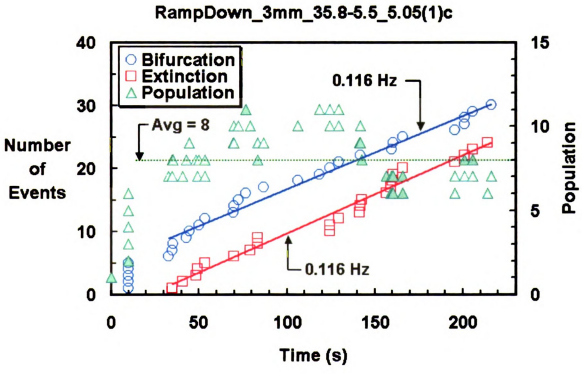

Figure 13. Example of flamelet population plot with 3 mm tunnel height in normal position of the test facility.

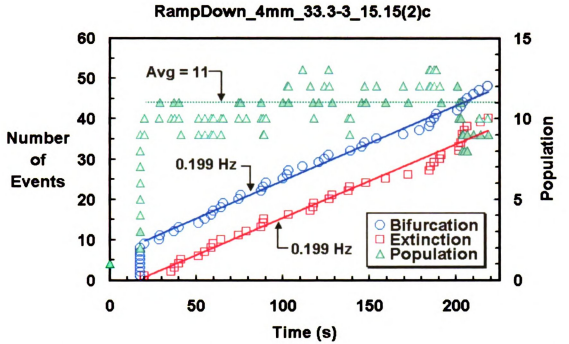

Figure 14. Example of flamelet population plot with 4 mm tunnel height in normal position of the test facility.

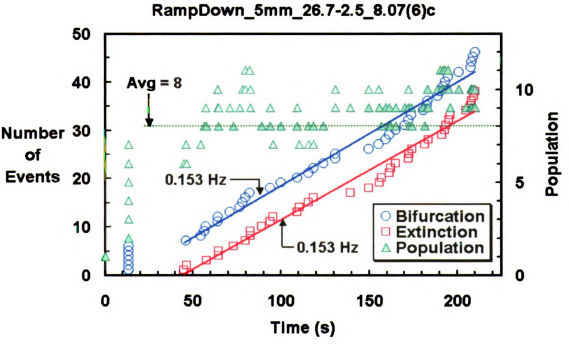

Figure 15. Example of flamelet population plot with 5 mm tunnel height in normal position of test facility.

A few tests that were analyzed showed a slightly different trend of bifurcation and extinction. For example, consider the flamelet population for 3 mm tunnel height with final air velocity of 5.5 cm/s, test RampDown_3mm_35.8-5.5_10.1(2)c, in Figure 16. The graph shows that the extinction slope is steeper than the bifurcation slope. This means that the extinction rate is higher. It happened because in the middle of the experiment, there was a significant increase of flamelet extinction. This can be visually explained using the corresponding fingering pattern of the test shown in Figure 17 (note the high extinction rate in the middle). As can be seen in the pattern several flamelets in the middle of the sample suddenly extinguished within a short period of time. Such occurrence motivates the need for a longer sample, since the flamelets appeared to require a longer time to reach a steady state.

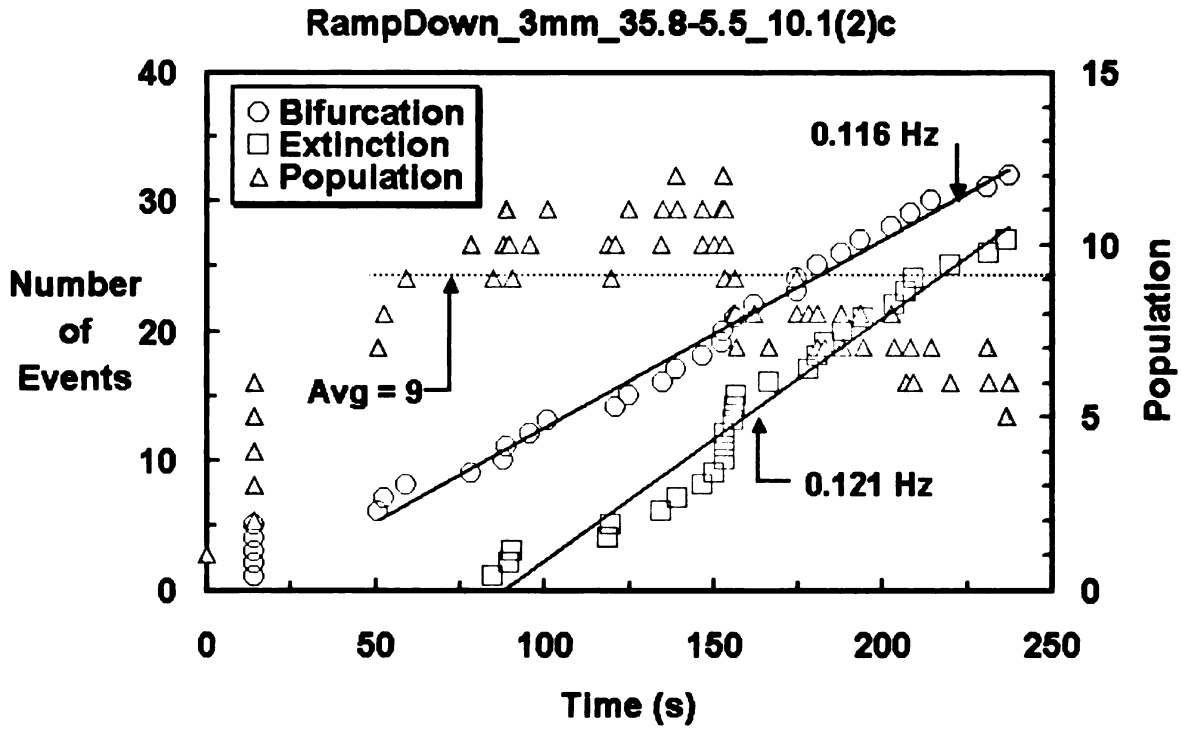

Figure 16. Example of flamelet population plot with high extinction rate in the middle of the experiment.

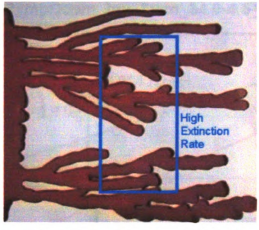

Figure 17. Fingering pattern of a test with high extinction rate in the middle of the experiment.

3.3.2 Experiments in the Inverted Position

Three flamelet population graphs that represent the results of the experiments in the inverted position for tunnel heights of 3, 4 and 5 mm can be found in Figures 18, 19, and 20, respectively.

Generally the flamelet population in the inverted position shows a similar behavior to the flamelet population in the normal position. The flamelet populations with tunnel heights of 4 and 5 mm have linear trend lines of bifurcation and extinction. These lines are parallel to each other, which means that the flamelet propagation achieved steady state. The cumulative number of the population shows an oscillatory behavior about that steady state. The flamelet population for the 3 mm tunnel height shows a slightly different result. Figure 18 shows that the trend line for extinction is steeper than for bifurcation. The frequency of bifurcation is lower than the frequency of extinction. This could mean that the experiment has not yet reached steady state or will never do so. In fact, many experiments in the inverted position of test facility with 3 mm tunnel height and very low final air velocities extinguished before the end of the sample.

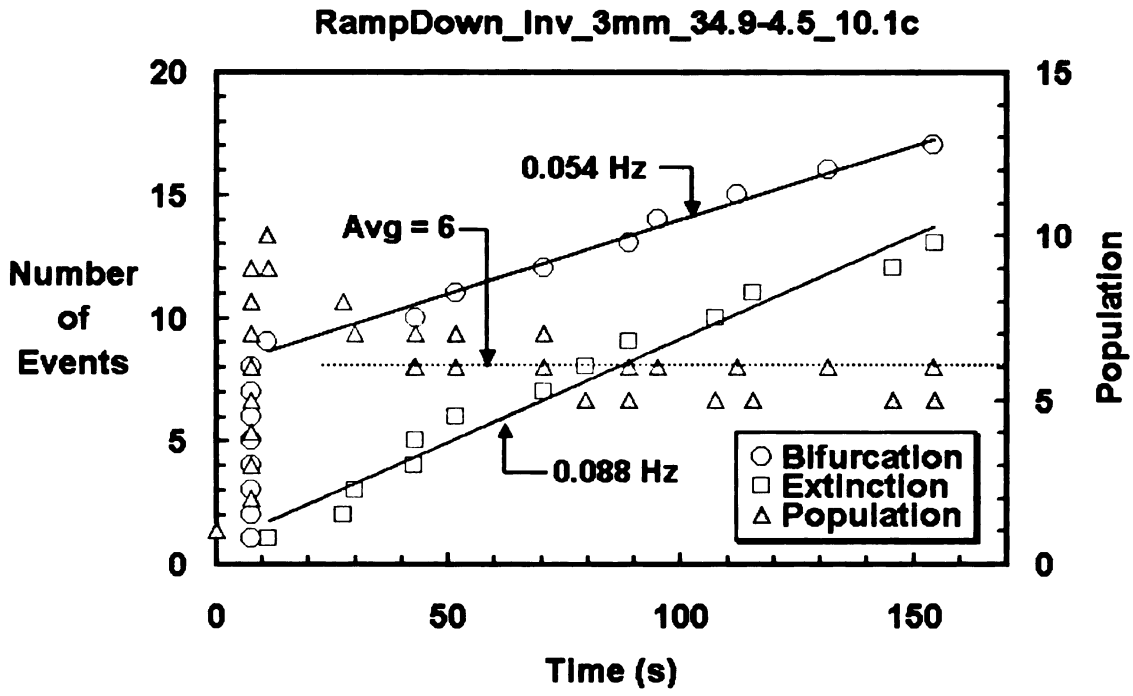

Figure 18. Example of flamelet population plot with 3 mm tunnel height in inverted position of the test facility.

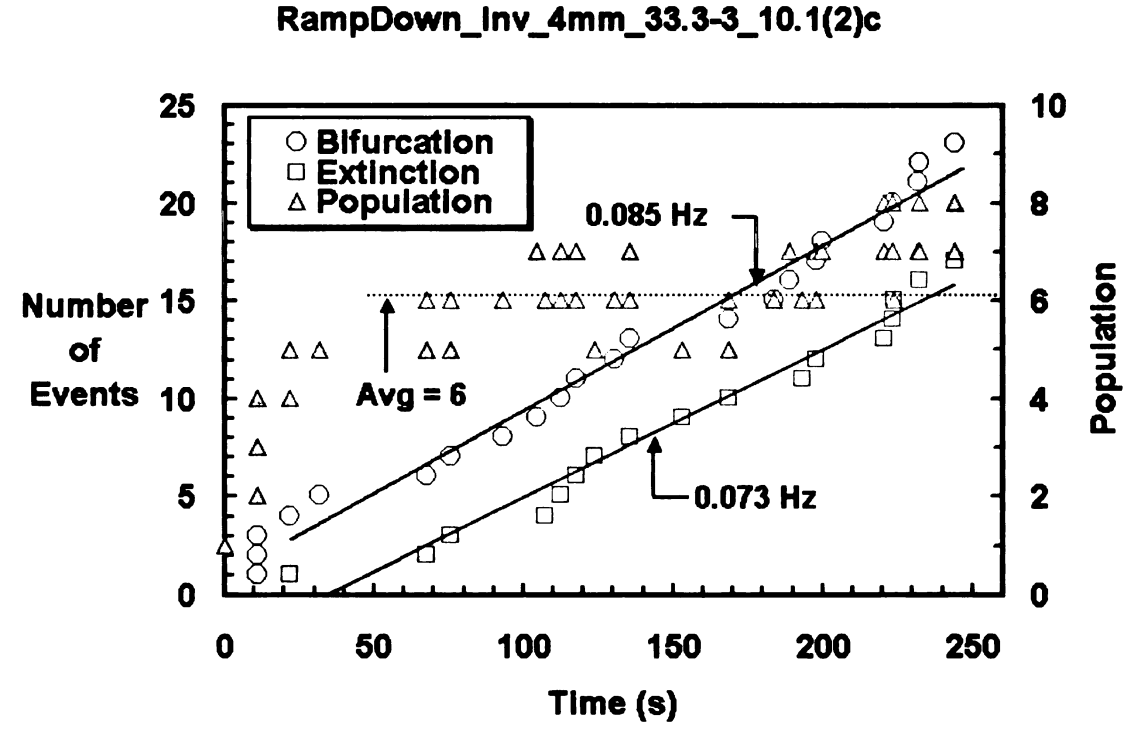

Figure 19. Example of flamelet population plot with 4 mm tunnel height in inverted position of the test facility.

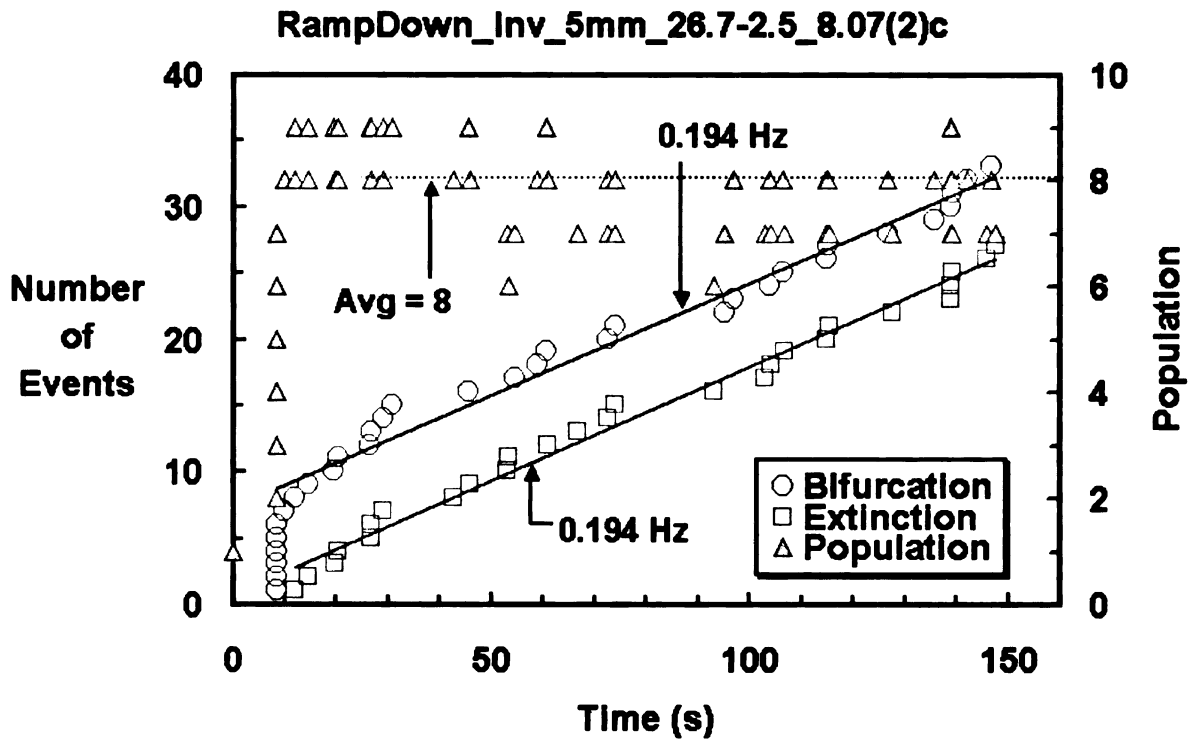

Figure 20. Example of flamelet population plot with 5 mm tunnel height in inverted position of the test facility.

3.3.3 Flamelet Population Summary

Table 2 is a summary of the average population, bifurcation and extinction rates. The average population was plotted for each tunnel height for both normal and inverted positions of the test facility. This plot can be found in Figure 21. In the figure, the normal position data are presented on the left side and the inverted position data are on the other side. Generally, the average numbers of flamelet population in both normal and inverted positions are proportional to the oxidizer flow level as well as the tunnel height. That is, the flamelet population increases as the final air velocity and tunnel height increase. Also, it can be seen that the average flamelet population for experiments in the normal position generally is higher than that in the inverted position.

Table 2. Average flamelet population, bifurcation rate, and extinction rate

Position	Tunnel Height (mm)	Air Velocity (cm/s)	Average Population	Average Bifurcation Rate (Hz)	Average Extinction Rate (Hz)	(Ext. rate-Bif. rate) Population
Normal	3	2.5	4	0.053	0.073	5.0E-3
		5.5	9	0.151	0.157	6.7E-4
	4	2.5	7	0.236	0.220	-2.2E-3
		3.0	9	0.224	0.196	-2.9E-3
		3.5	8	0.334	0.298	-4.5E-3
		4.0	11	0.219	0.197	-2.0E-3
	5	2.5	8	0.174	0.173	-2.7E-5
		5.0	12	0.163	0.140	-1.9E-3
Inverted	3	3.5	5	0.091	0.139	9.1E-3
		4.5	6	0.061	0.075	2.2E-3
	4	3.0	6	0.090	0.084	-1.2E-3
		3.5	9	0.147	0.142	5.6E-4
		4.0	9	0.133	0.115	-2.0E-3
		5.0	6	0.135	0.135	0
	5	2.5	7	0.155	0.161	8.8E-4
		3.5	8	0.170	0.150	-2.5E-3

The bifurcation rate versus the extinction rate was plotted in Figure 22. The dotted line is the x=y line. As shown in the plot, the agreement between the bifurcation and the extinction rates is nearly unity. This verifies that flamelet propagation nearly achieve a constant rate or are in steady state. The trend line leans toward the bifurcation side, which means that the bifurcation rate is on average slightly higher than the extinction rate. This is because the initial flamelet distribution was not uniform, although the spread becoming more uniform throughout the sample. When the bifurcation rate is higher flamelets presumably continue to propagate, i.e. the spread rate can continue as long as there are more bifurcations than extinction. In addition, it is apparent that generally the experiments in the normal position have slightly higher rates of bifurcation and extinction. The equations for the slopes are shown in the plot, where y_n is for normal position data points and y_i is for inverted position data points.

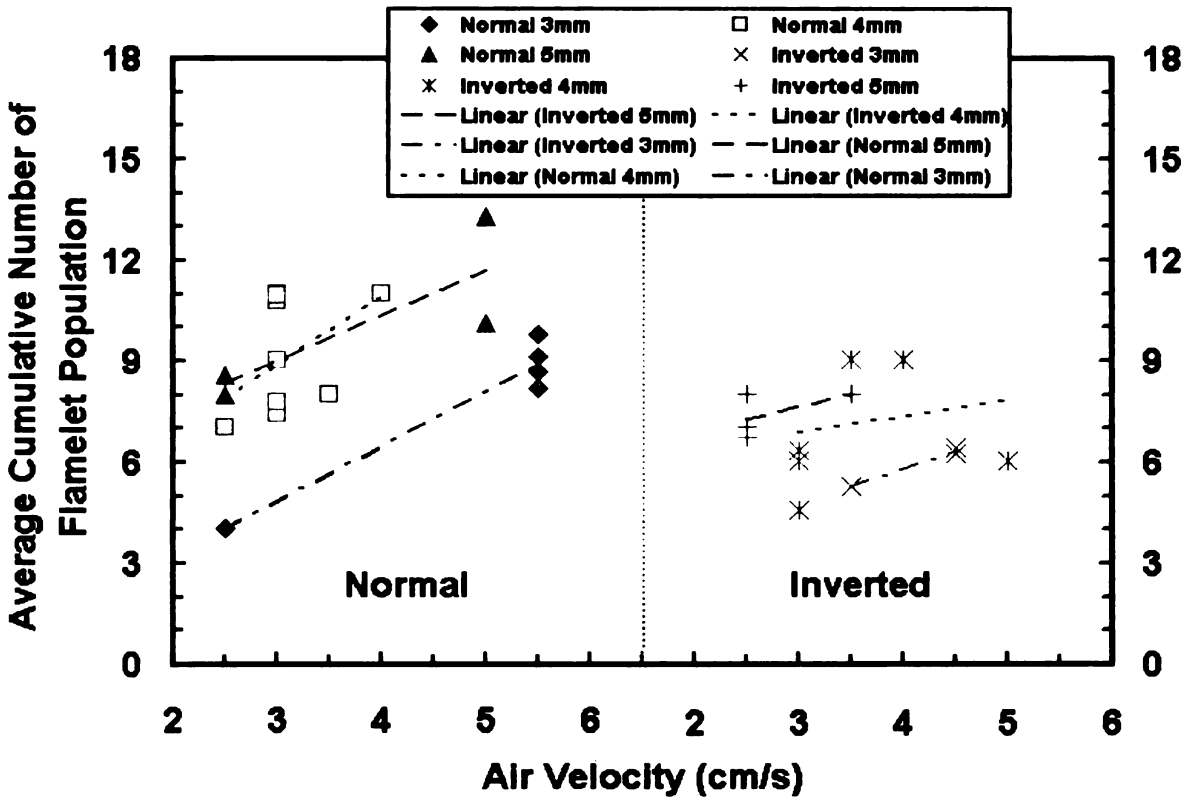

Figure 21. Average number of flamelet population versus final airflow test velocity.

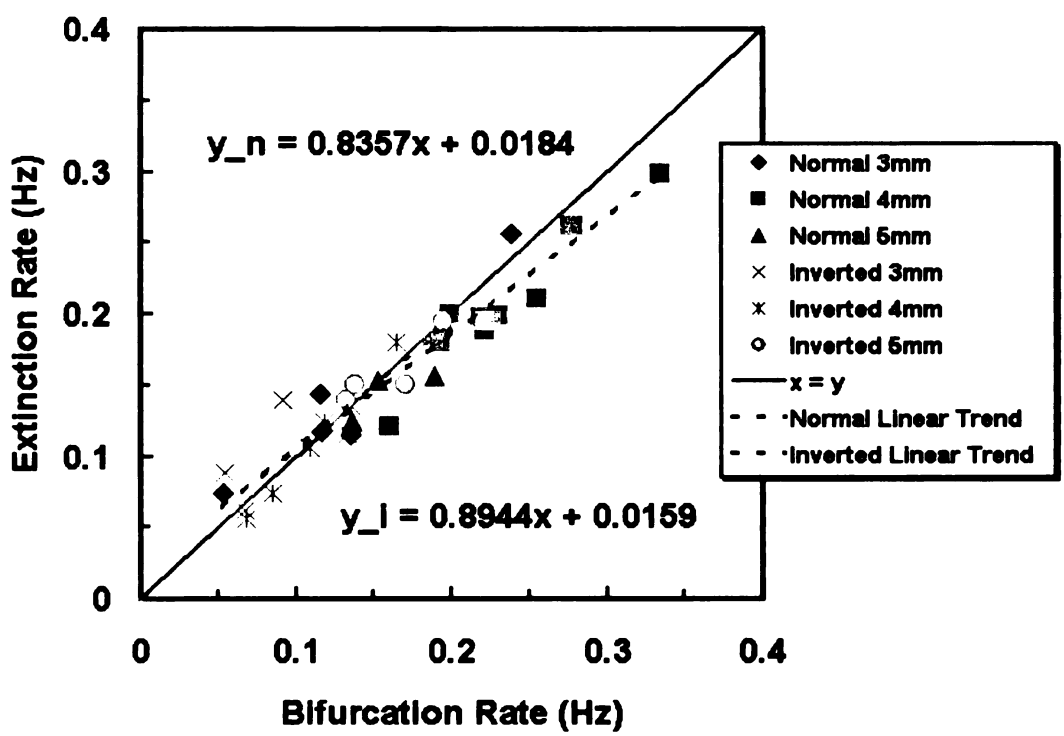

Figure 22. Bifurcation rate versus extinction rate.

Two plots, Figures 23 and 24, were established to further study on the total number of the flamelet population. Figure 23 shows the total number of flamelets versus the tunnel height for the same final air velocity. For the normal position of the test facility, the final air velocity was 2.5 cm/s and for the inverted position, the final air velocity was 3.5 cm/s. The plot shows that for fixed final air velocity of 2.5 cm/s, the number of flamelets increases as the tunnel height increases for experiments in the normal position. However, experiments in the inverted position show that the number of flamelets increases from tunnel heights 3 to 4 mm, then decreases from tunnel heights 4 to 5 mm for fixed final air velocity of 3.5 cm/s.

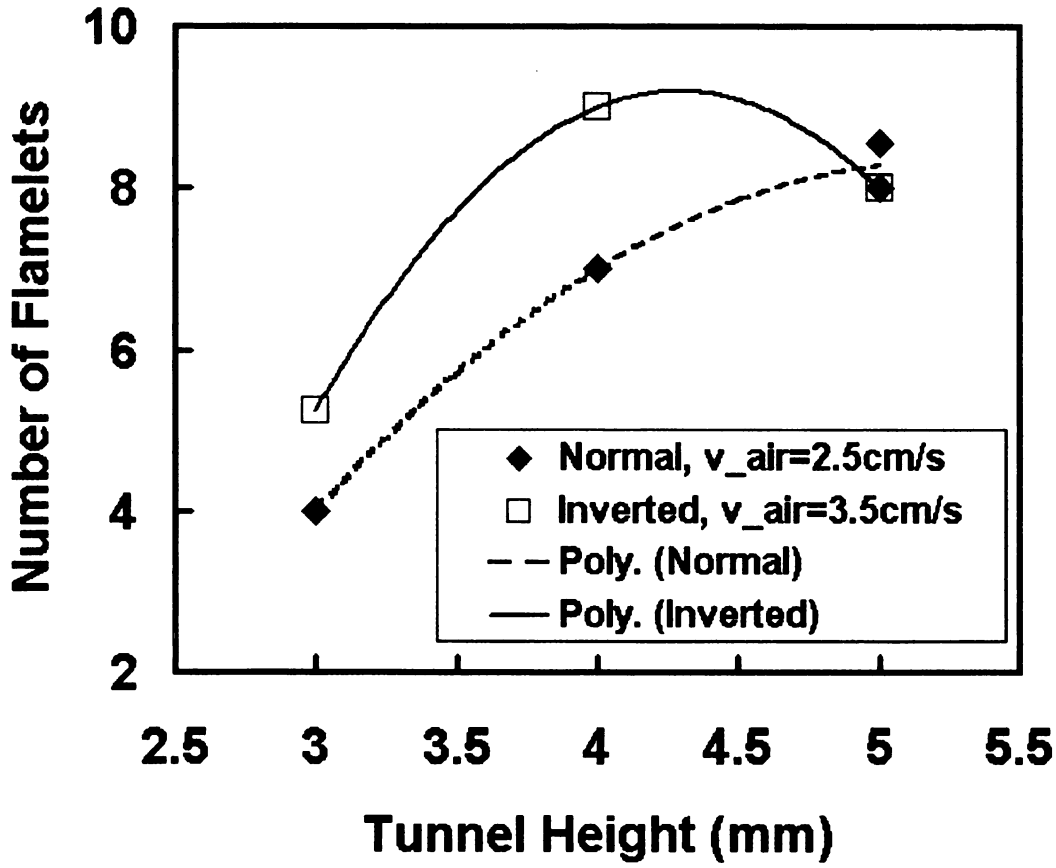

Figure 23. Number of flamelets for various tunnel heights with the same final air velocity (2.5 cm/s for normal position and 3.5 cm/s for inverted position).

Figure 24 shows the number of flamelets versus the product of the tunnel heights and the final air velocity plot. The second order polynomial trend lines were drawn for experiments in the normal and inverted positions of the test facility. For experiments in the normal position, the trend shows that the number of flamelets generally increases, as there is more oxidizer flowed into the system. Experiments in the inverted position show a parabolic trend.

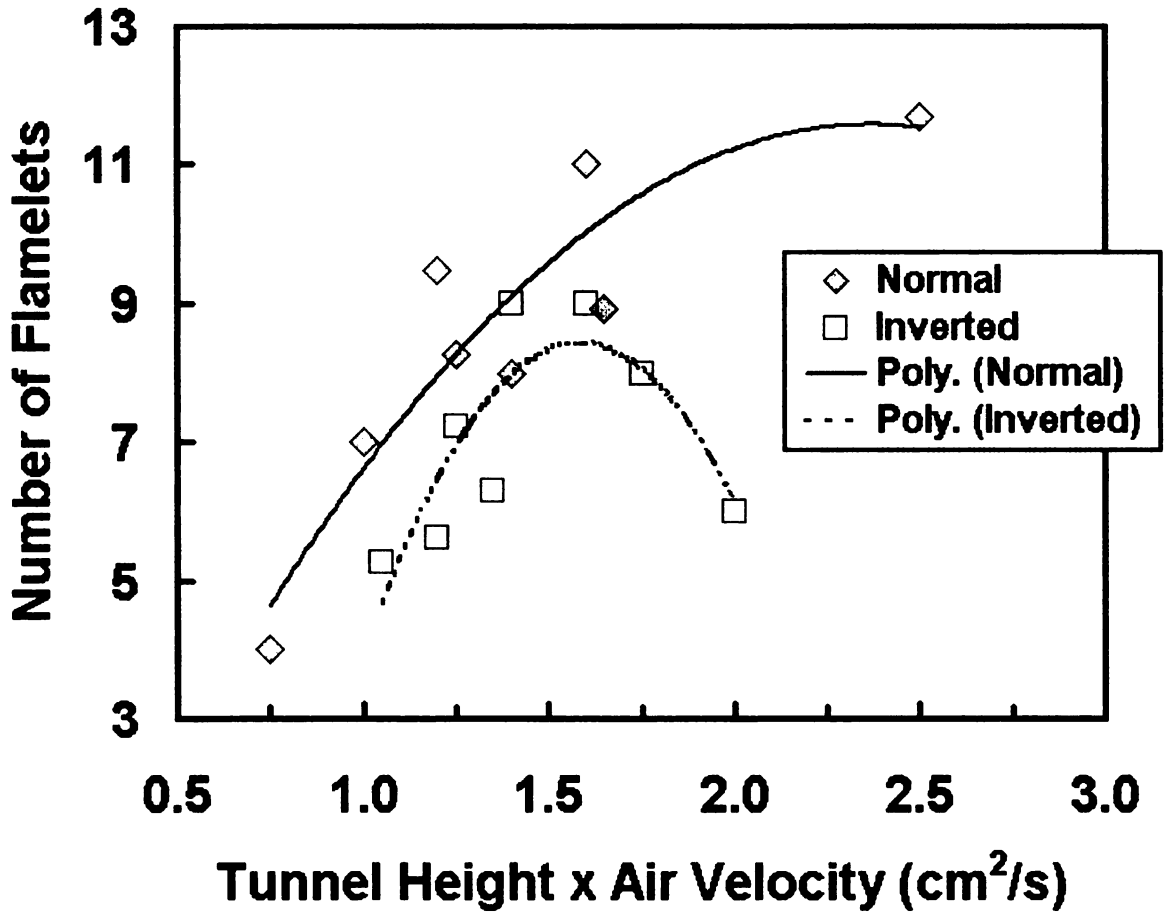

Figure 24. Plot of number of flamelets versus the product of tunnel height and air velocity.

3.4 Flamelet Lifetime

Flamelet lifetime is presented in the form of bar graphs. The x-axis (abscissa) is the flamelet category and the y-axis (ordinate) is the flamelet lifetime on a logarithmic scale with unit of second.

3.4.1 Experiments in the Normal Position

Figures 25, 26 and 27 represent the results of flamelet lifetime for experiments in the normal position with tunnel heights of 3, 4 and 5 mm, respectively. Flamelets generally lived less than 100 seconds. There are only a small number of flamelets that lived slightly more than 100 seconds. As can be seen in these graphs, generally the slopes are gradually increasing for each flamelet category. However, there are a few tests where the slope for category flamelet infants is flat then rapidly increases. The flat part implies that there are as many infants born as those that die right away.

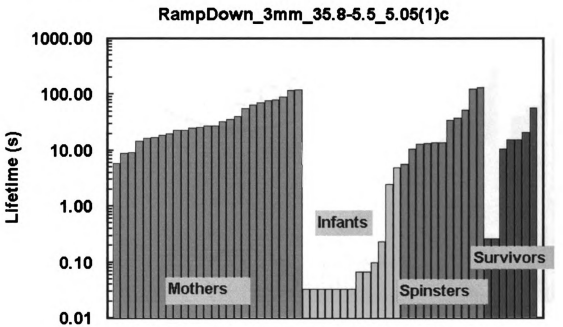

Figure 25. Example of flamelet lifetime plot with 3 mm tunnel height in normal position of the test facility.

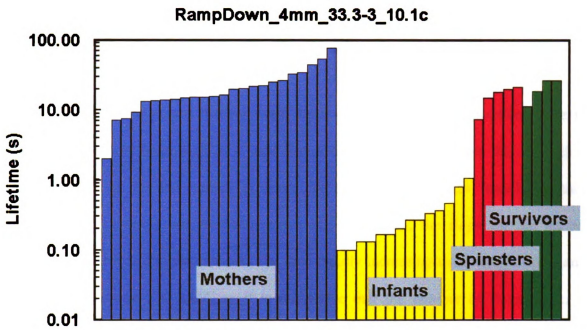

Figure 26. Example of flamelet lifetime plot with 4 mm tunnel height in normal position of the test facility.

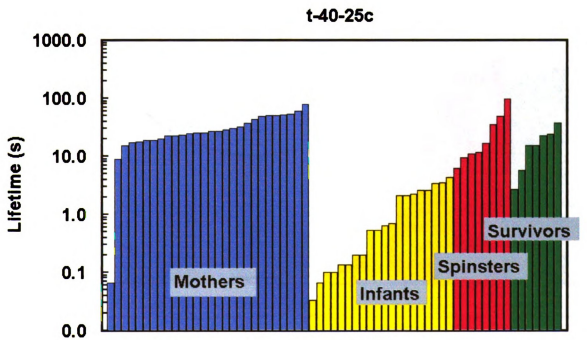

Figure 27. Example of flamelet lifetime plot with 5 mm tunnel height in normal position of the test facility.

3.4.2 Experiments in the Inverted Position

The three bar graphs that represent the results in the inverted position of the test facility with tunnel heights of 3, 4, and 5 mm can be seen in Figures 28, 29, and 30, respectively. As for the normal position, the slope for categories flamelet mothers, spinsters and survivors are gradually increasing. However, the slope for the flamelet infants in the inverted position shows flat then rapidly increasing trend more often than in the normal position. In addition, it is noticeable that the number of flamelets in the inverted position is less than the number of flamelest in the normal position.

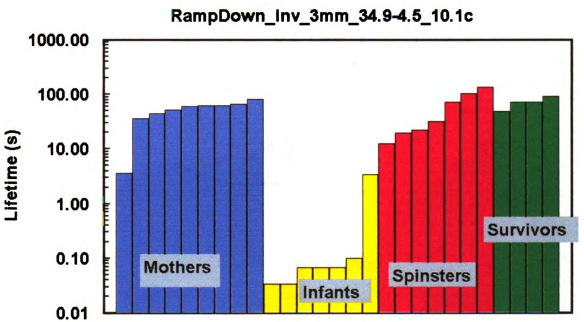

Figure 28. Example of flamelet lifetime plot with 3 mm tunnel height in inverted position of the test facility.

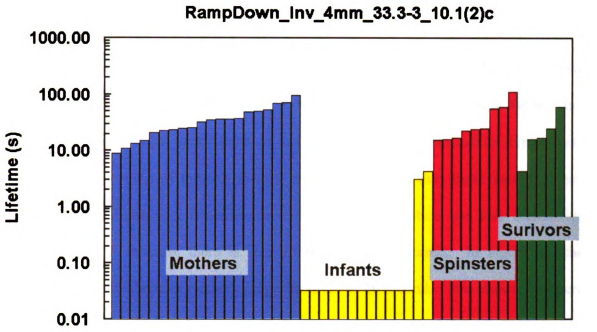

Figure 29. Example of flamelet lifetime plot with 4 mm tunnel height in inverted position of the test facility.

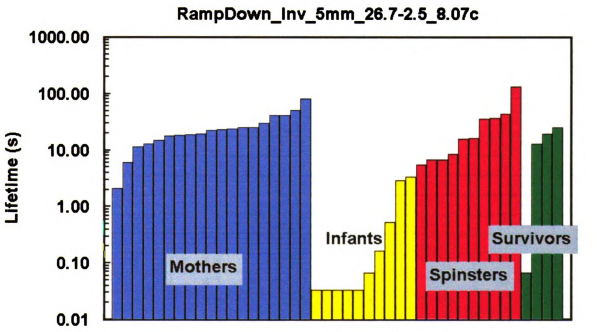

Figure 30. Example of flamelet lifetime plot with 5 mm tunnel height in inverted position of the test facility.

3.4.3 Flamelet Lifetime Summary

A summary of the average lifetime of flamelets can be found in Table 3. These numbers were plotted and shown in Figure 31 through Figure 34. As listed in Table 3 and shown in Figures 31 to 34, the lifetimes of flamelets mothers and spinsters for experiments in the inverted position of the test facility are slightly higher than those in the normal position. This shows that experiments in the inverted position has less cumulative population overall, because there is less bifurcation that occurred. In Figure 31, the average lifetime for flamelet mothers ranges from 10 to 60 seconds. It is shown in Figure 32 that the average lifetime for flamelet infants ranges from 0 to 1.5 seconds, and more than half of it is concentrated between 0 and 0.5.

Table 3. Average flamelet lifetime for mothers, infants, spinsters, and survivors

Position	Tunnel Height (mm)	Final Air Velocity (cm/s)	Flamelet Mother Lifetime (s)	Flamelet Infant Lifetime (s)	Flamelet Spinster Lifetime (s)	Flamelet Survivor Lifetime (s)
Normal	3	2.5	30.85	0.15	13.07	118.57
		5.5	34.04	0.86	46.25	40.30
	4	2.5	15.32	0.33	25.11	16.79
		3.0	24.49	0.58	23.65	20.58
		3.5	16.14	0.35	12.96	12.03
		4.0	25.60	1.22	15.78	30.91
	5	2.5	24.98	0.56	24.57	29.64
		5.0	32.14	1.13	32.97	19.90
Inverted	3	3.5	32.05	0.23	32.71	31.00
		4.5	45.50	0.29	76.37	68.99
	4	3.0	34.05	0.18	22.09	32.49
		3.5	34.22	0.38	33.42	53.89
		4.0	28.13	0.30	22.30	58.92
		5.0	20.17	1.31	14.33	25.67
	5	2.5	26.59	0.56	26.91	26.58
		3.5	25.55	0.31	17.44	20.57

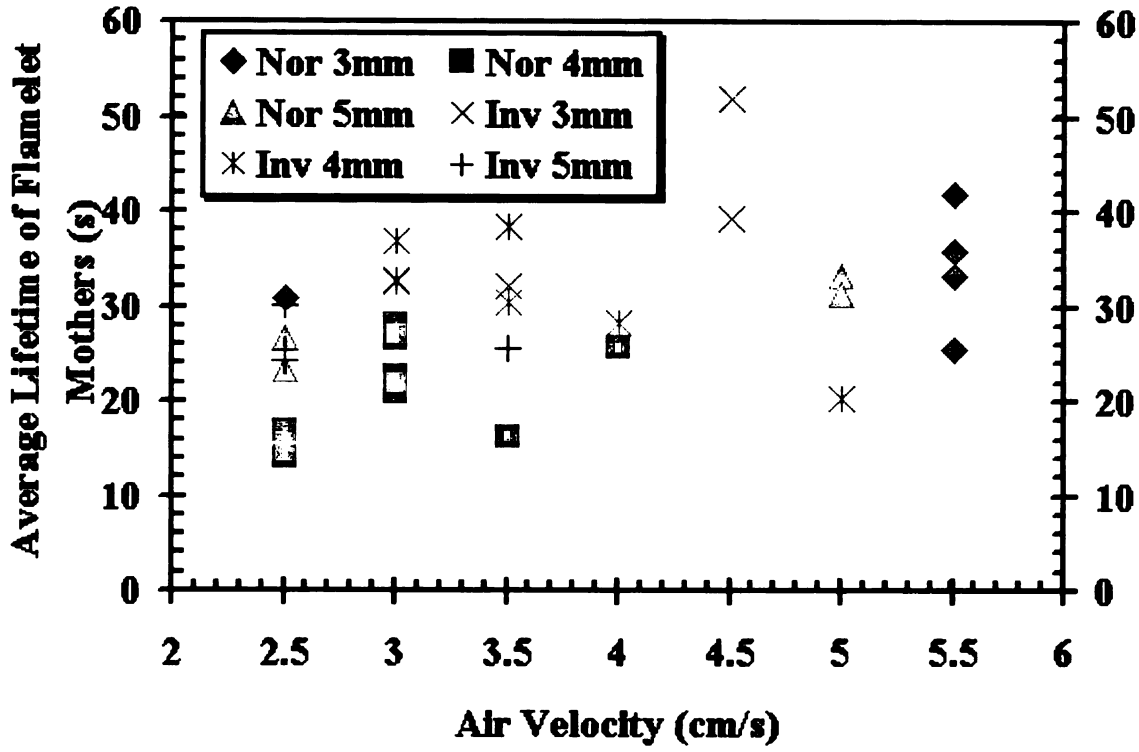

Figure 31. Average lifetime for flamelet mothers versus final air flow velocity.

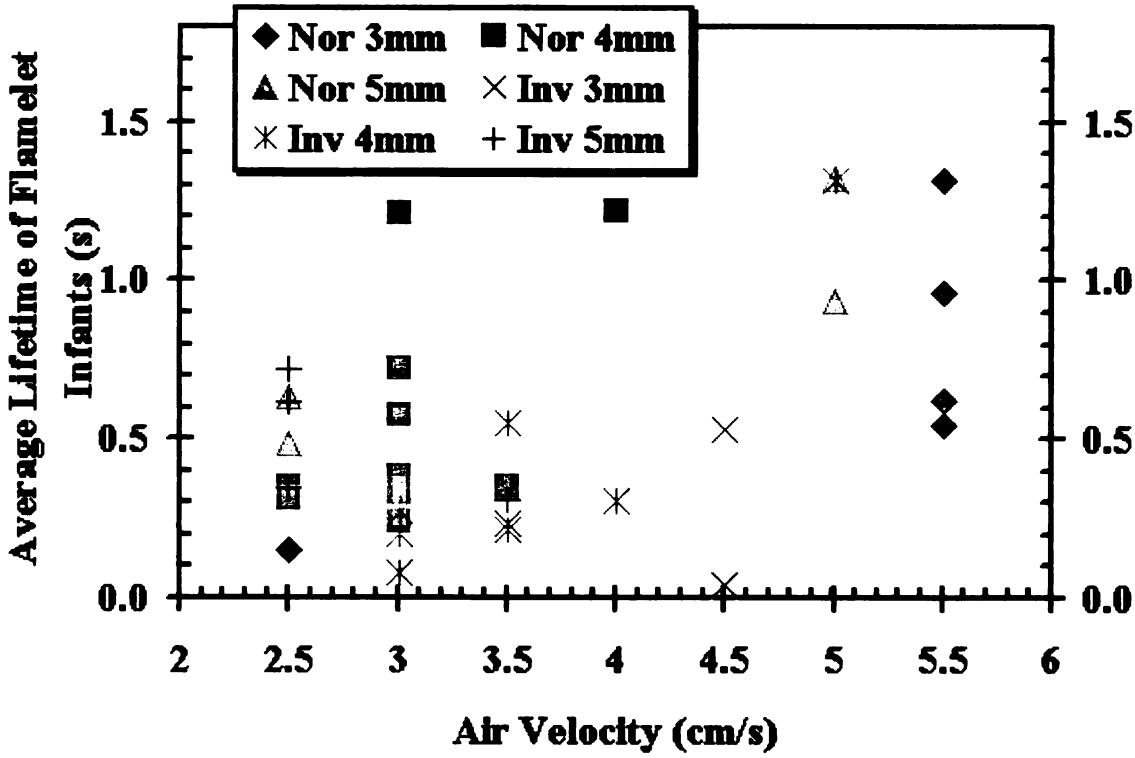

Figure 32. Average lifetime for flamelet infants versus final air flow velocity.

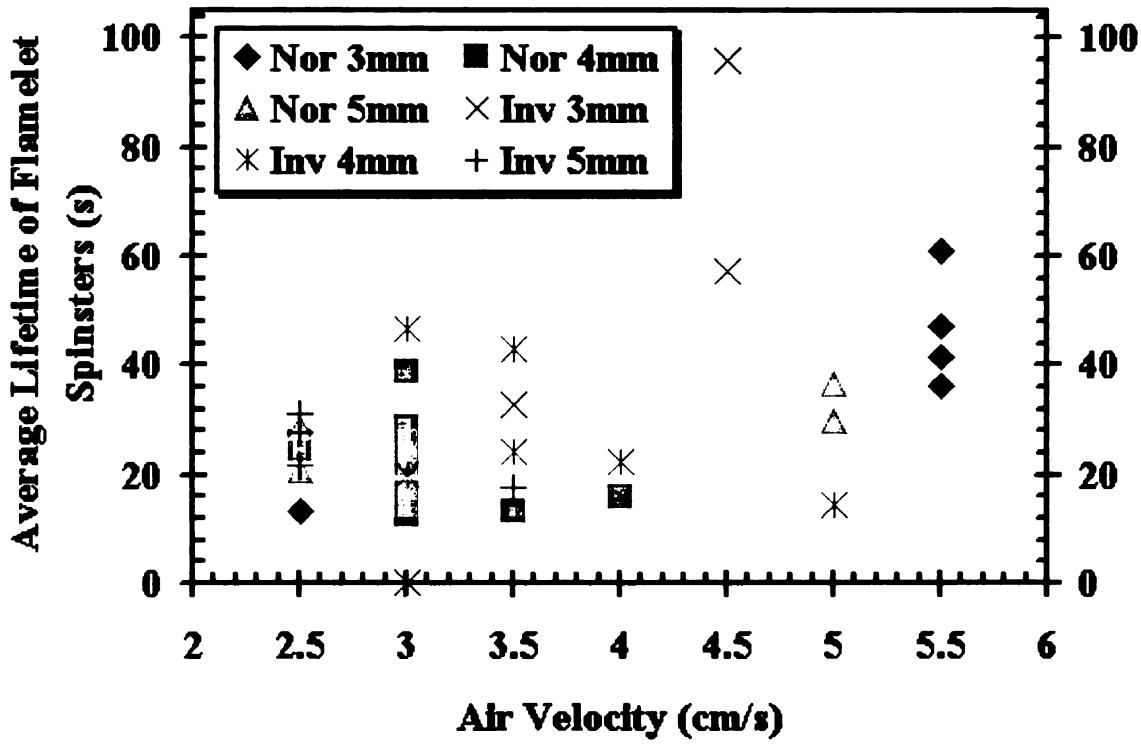

Figure 33. Average lifetime for flamelet spinsters versus final air flow velocity.

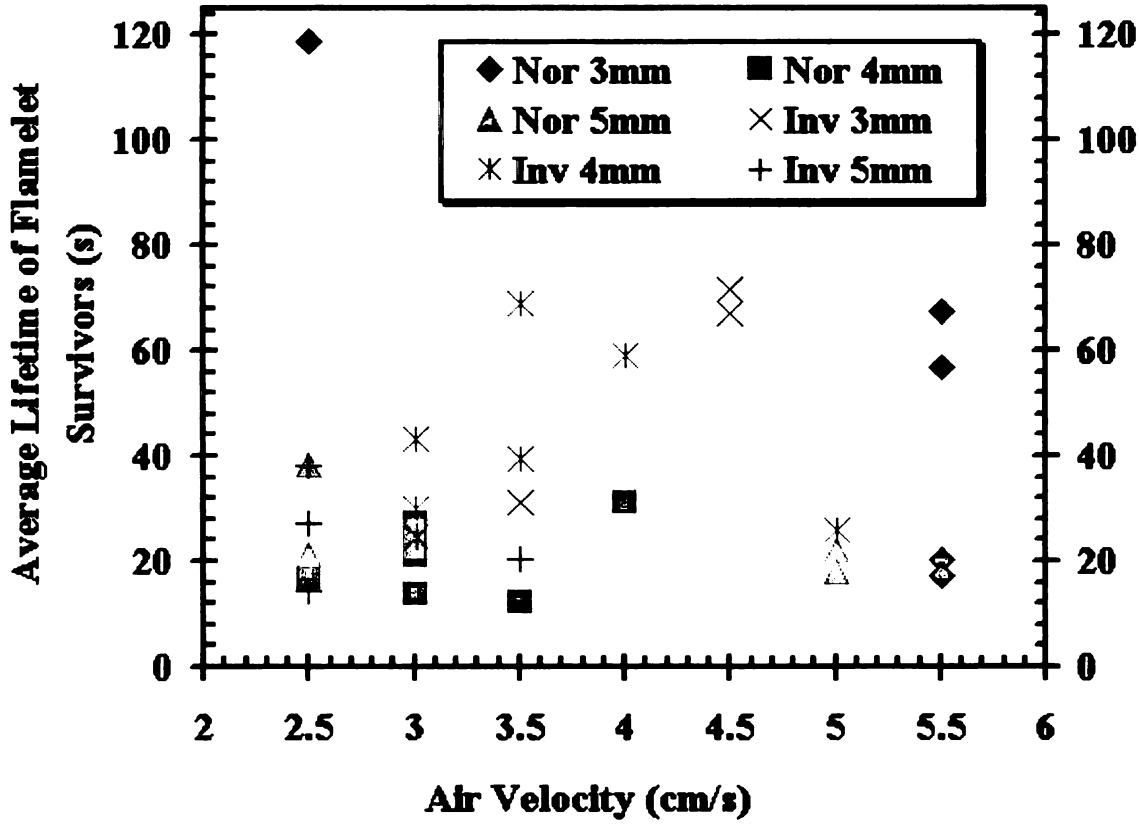

Figure 34. Average lifetime for flamelet survivors versus final air flow velocity.

In Figure 33, it appears that there is one outlier. This outlier is of the inverted test with test conditions of 3 mm tunnel height and final air velocity of 4.5 cm/s. This particular test has a higher average lifetime for flamelet spinsters. This can be explained by observing the fingering patterns of the tests. A fingering pattern of a test with the same conditions (inverted, tunnel height = 3 mm, air velocity = 4.5 cm/s) is shown in Figure 35. This picture shows that there are not many fingering branches. From the pattern, it can be said that many of the flamelets traveled for long period of time as spinsters.

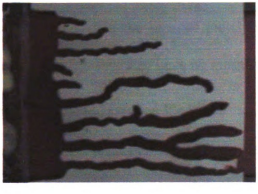

Figure 35. A fingering pattern of a test with higher lifetime of flamelet spinsters.

In Figure 34, an outlier appears at an air velocity equals to 2.5 cm/s. This outlier is from the experiment in the normal position with tunnel height equals 3 mm. From Figure 34, the average lifetime of the flamelet survivors is about 120 s. This can be explained by observing the fingering pattern of the test. Shown in Figure 36 is the fingering pattern of the test. It can be seen that there are two flamelets that survived to the end of the experiment. These two flamelets traveled long without bifurcating until one of them reached the end of the sample paper. Flamelet spinsters or long life survivors appeared in many of the 3 mm tunnel height experiments both in normal and inverted positions of the test facility.

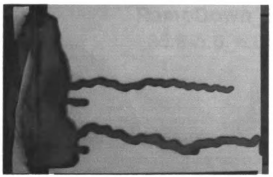

Figure 36. A fingering pattern of a test with higher lifetime of flamelet survivors.

3.5 Flamelet Census

The flamelet census is presented in the form of pie charts. In the pie charts the flamelet survivors were not included because they have no meaning in the total population.

3.5.1 Experiments in the Normal and Inverted Positions

The pie charts in Figure 37 on page the next page represent the results of tunnel heights 3, 4, and 5 mm for experiments in the normal position of the test facility. The charts show the percentages of the flamelet mothers, infants and spinsters. The pie charts show that the distribution of each category is virtually uniform. At least 50% of the total population are productive flamelets (mothers), and the other 50% of the total population are unproductive flamelets (infants and spinsters).

The pie charts that represent the results for tests in the inverted position for tunnel heights of 3, 4, and 5mm are shown in Figure 38. The three pie charts show a good agreement with the results in the normal position. At least 50% of the total population is productive flamelets (mothers) and the remaining 50% are unproductive flamelets (infants and spinsters). The distribution of categories flamelets infants and spinsters are not as uniform as the results in the normal position.

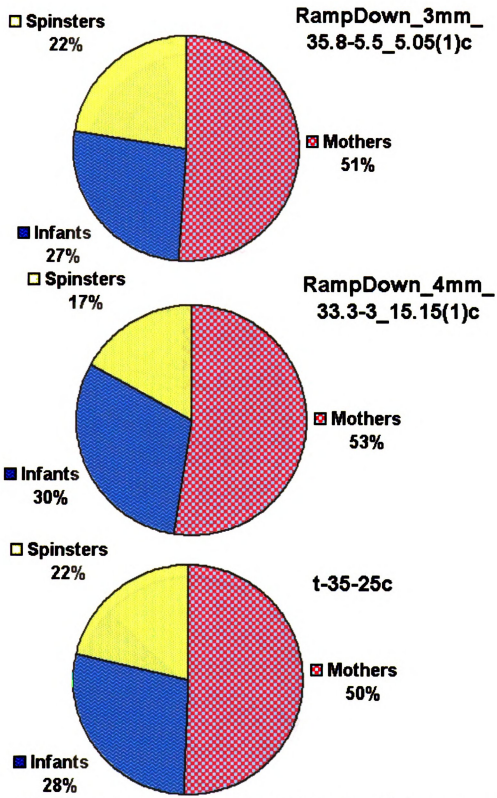

Figure 37. Example pie charts for results of experiments in the normal position of test facility with tunnel heights of 3, 4, and 5 mm.

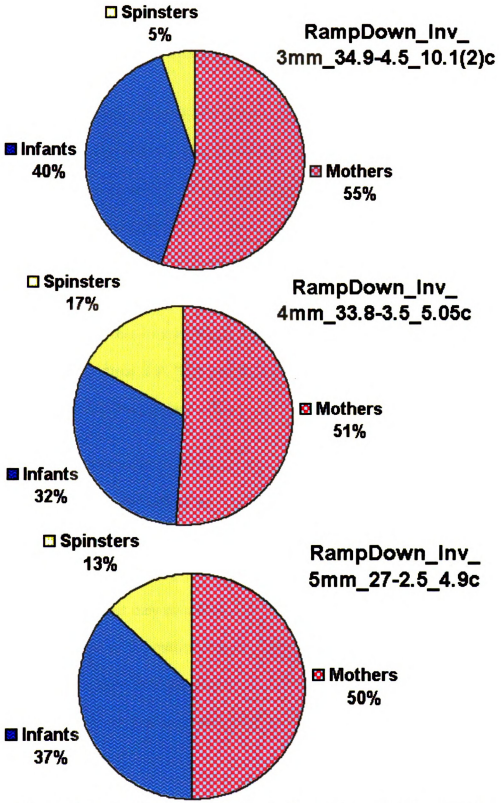

Figure 38. Example pie charts for results of experiments in the inverted position of test facility with tunnel heights of 3, 4, and 5 mm.

3.5.2 Flamelet Census Summary

A summary of the population percentages of flamelet mothers, infants and spinsters can be found in Table 4. The summary plot of percentage population of flamelet mothers can be found in Figure 39. Drawn in the graph are the ± 3% limits from the 50% line. The majority of the tests show that flamelet mothers are within the 50% ± 3% range. There are 21 tests between 47%-53%, 5 tests are above 53%, and 4 tests are below 47% (3 of them are far below the line). Ignoring the three outliers, this result generally shows a good agreement with the results studied at NASA. The prediction done by Olson, Miller and Wichman [9] states that 50% of survivorship is necessary for flamelets to continue to propagate indefinitely (steady state).

The three outliers shown in Figure 39 are of 3 mm tunnel height tests. One of the three tests was in the normal position with a final air velocity of 2.5 cm/s. The other two tests were in the inverted position with final air velocities of 3.5 cm/s and 4.5 cm/s. These three tests had a relatively low oxygen delivery rate level. In these conditions flamelets hardly survive, but they continued to move slowly for a very long time. In addition, these test correspond to the outliers shown previously in Figures 31 and 32. In Figure 39, the three outliers show low numbers of flamelet mothers, while in Figures 33 and 34 these three outliers show high numbers of spinsters and survivors.

Table 4. Summary of flamelet census for both normal and inverted tests

Position	Tunnel Height (mm)	Velocity (cm/s)	Mothers (%)	Infants (%)	Spinsters (%)
Normal	3	2.5	42.11	42.11	15.79
		5.5	48.44	30.92	20.64
	4	2.5	51.73	39.61	8.68
		3.0	52.67	33.05	14.28
		3.5	51.47	38.24	10.29
		4.0	52.63	31.58	15.79
	5	2.5	49.96	34.95	15.09
		5.0	50.32	31.78	17.91
Inverted	3	3.5	42.11	44.74	13.16
		4.5	47.07	35.22	17.72
	4	3.0	52.60	40.24	7.16
		3.5	49.38	31.34	19.28
		4.0	53.57	28.57	17.86
		5.0	50.00	27.08	22.92
	5	2.5	49.23	34.50	16.27
		3.5	51.92	28.85	19.23

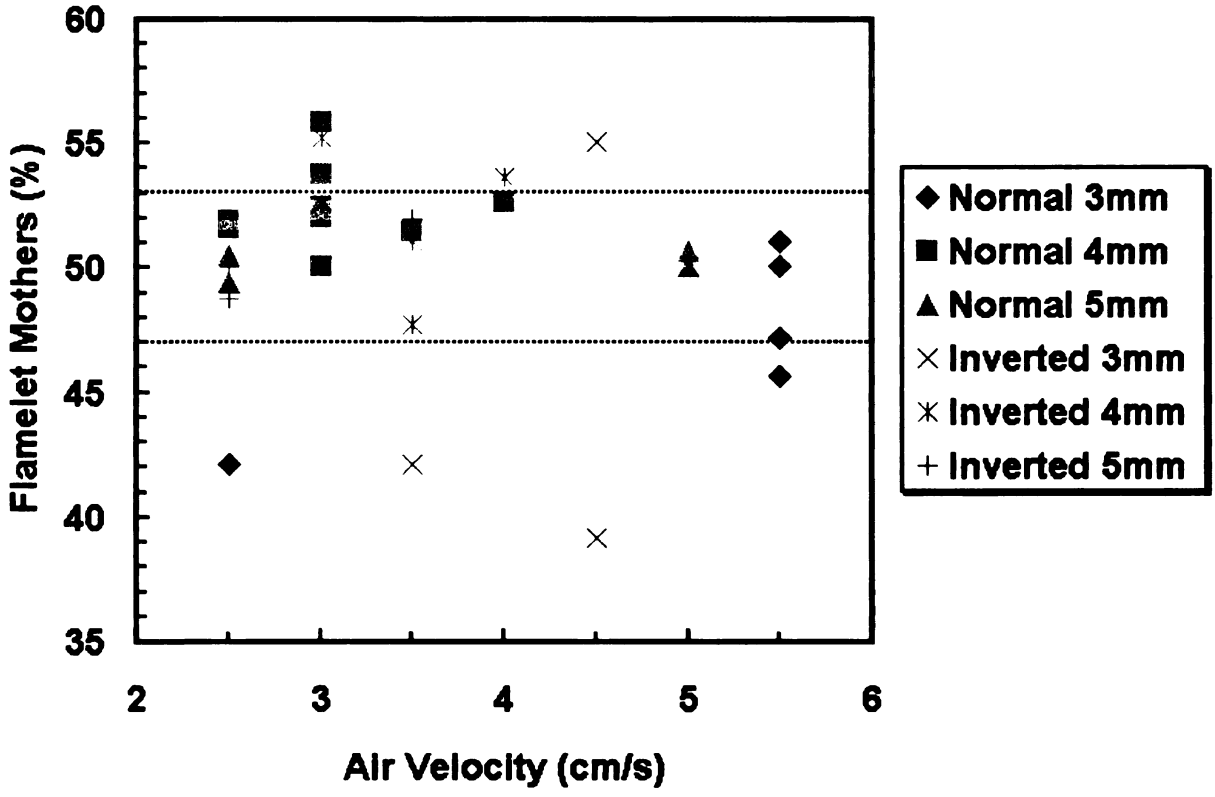

Figure 39. Percentage of flamelet mothers versus final air flow velocity.

The next two graphs in Figures 40 and 41 are the population percentages of flamelets infants and spinsters. As shown, the population percentage of flamelet infants mostly scattered between 20% and 45%. On the other hand, the flamelet spinsters scattered between 0% and 30%. The data points for the infants show a slight decrease as the air velocity increases. Conversely, the data points for the spinsters show a slight increase as the air velocity increases.

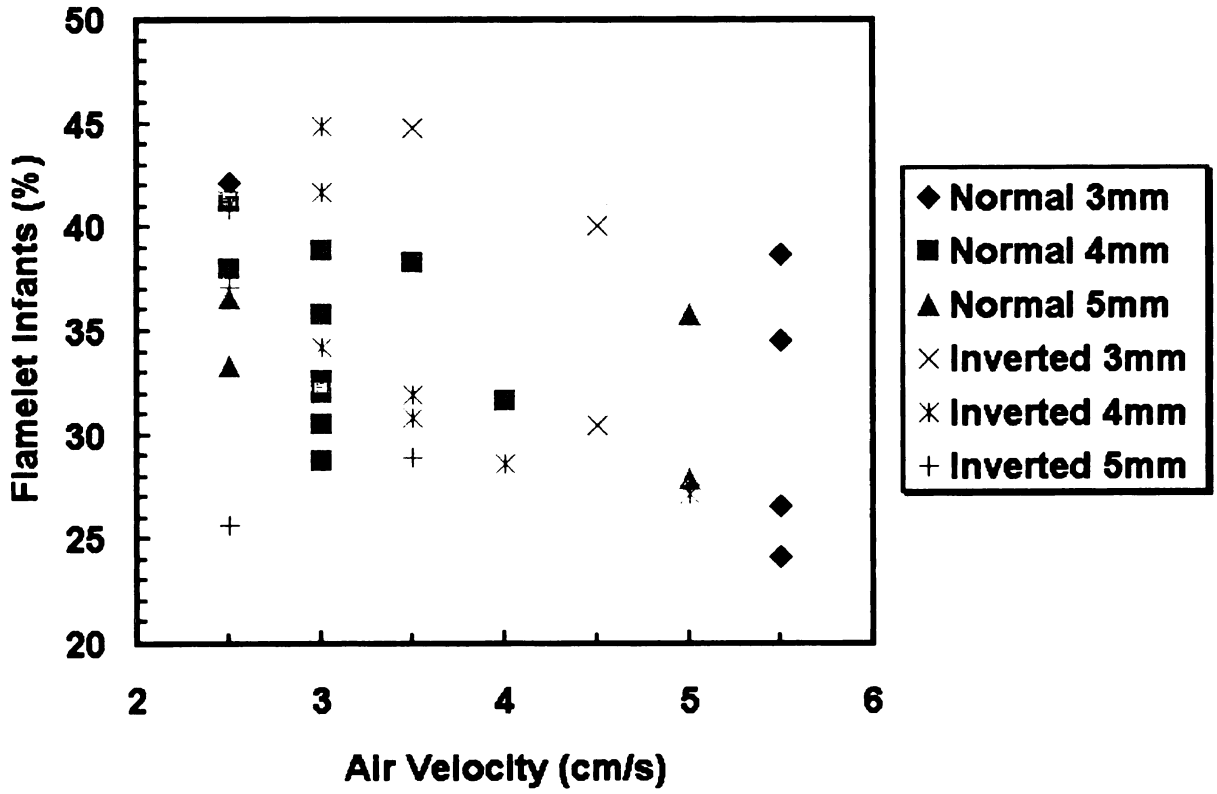

Figure 40. Percentage of flamelet infants versus final air flow velocity.

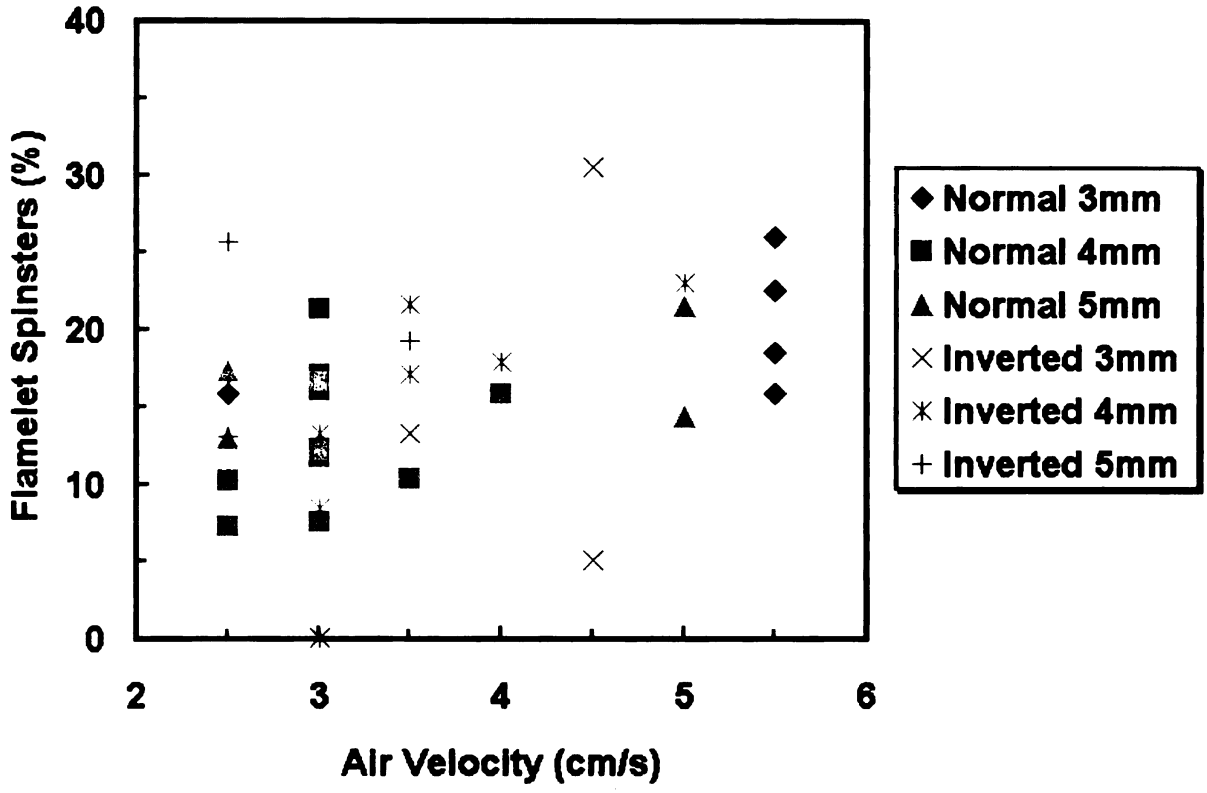

Figure 41. Percentage of flamelet spinsters versus final air flow velocity.

CHAPTER 4
FLAMELET BIFURCATION ANGLE ANALYSIS

4.1 Background

The fingering pattern that flamelets produce in search of oxygen has different characteristics. Depending on the test conditions, such as the tunnel height and the air velocity, the fingering patterns have different gap spaces and bifurcation angles. Two samples of the fingering patterns of two different tests are shown in Figures 42 and 43.

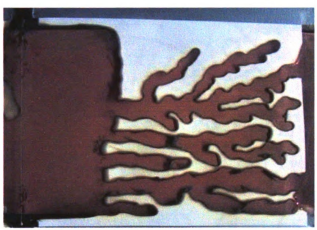

Figure 42. Fingering pattern with tunnel height of 5 mm and final air velocity of 2.5 cm/s in the normal position of the test facility.

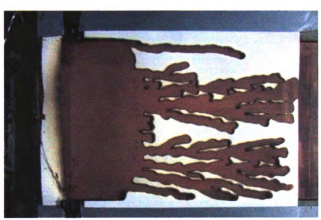

Figure 43. Fingering pattern with tunnel height of 3 mm and final air velocity of 5.5 cm/s in the normal position of the test facility.

The white portion is the unburned fuel sample and the black portion is char. Figure 42 shows the fingering result of a test with a 5 mm tunnel height and a final 2.5 cm/s air velocity. Figure 43 shows the fingering result of a test with a 3 mm tunnel height and a final air velocity of 5.5 cm/s. As can be seen in Figure 42, the fingering is more distinguished compared to the fingering in Figure 43. In Figure 43, the fingers are closer to one another.

The flamelet "infants" previously discussed are those with lifetimes less than 5 seconds after bifurcation. Many of them had lifetimes that are less then 1 second. This rapid extinction causes the flamelet burn pattern to be wavy. For example, consider flamelets A and B in Figure 44. The pathway of flamelet A does not have branches, however is wavy. Flamelet A unsuccessfully bifurcated many times. On the other side, the pathway of flamelet B has 5 obvious branches. The bifurcation angle measurement accounted the wavy edges caused by the fast extinction as well as the more obvious separation.

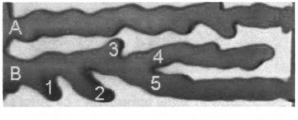

Figure 44. Picture of fingers with different bifurcation angles.

4.2 Approach

At the end of each experiment, a picture of the fingering pattern was taken. The picture was taken with the room lighting and the copper background to receive excellent contrast. Bifurcation angle measurements were done easily with the help of Adobe Photoshop 7.0. First, ovals were drawn following every curve of the fingering pattern.

Using the protractor tool the angle was determined for each oval. The data were stored in the Excel spreadsheet. The burnt material near the end of the sample was ignored since the fingering pattern was not a result of the flamelets, but because surviving flamelets reached the end of the sample and burned backwards to consume more of the sample. Figure 45 shows how the bifurcation angle measurement was done. As was expected, at several points there were multiple bifurcations. When that occurred, the average of the bifurcation angles at that point was taken instead. Figure 45 shows an example of the bifurcation angle measurement.

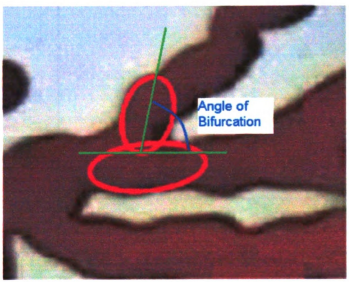

Figure 45. Measuring angle of bifurcation.

4.3 Results and Discussion

The measurement ignored which direction the flamelets grew because it was more important to record the angle and not its direction (i.e., positive or negative with respect to the inflow direction).

4.3.1 Experiments in the Normal Position

The average angles of bifurcation in the normal position for tunnel heights of 3, 4 and 5 mm are shown in Figure 46. The air velocities for the each tunnel height are 3.5 cm/s, 3 cm/s and 2.5 cm/s, respectively. As can be observed from the plot, the average bifurcation angle is proportional to the tunnel height. When the tunnel height increases the bifurcation angle increases as well. The bifurcation angle ranges from 15° to 22°.

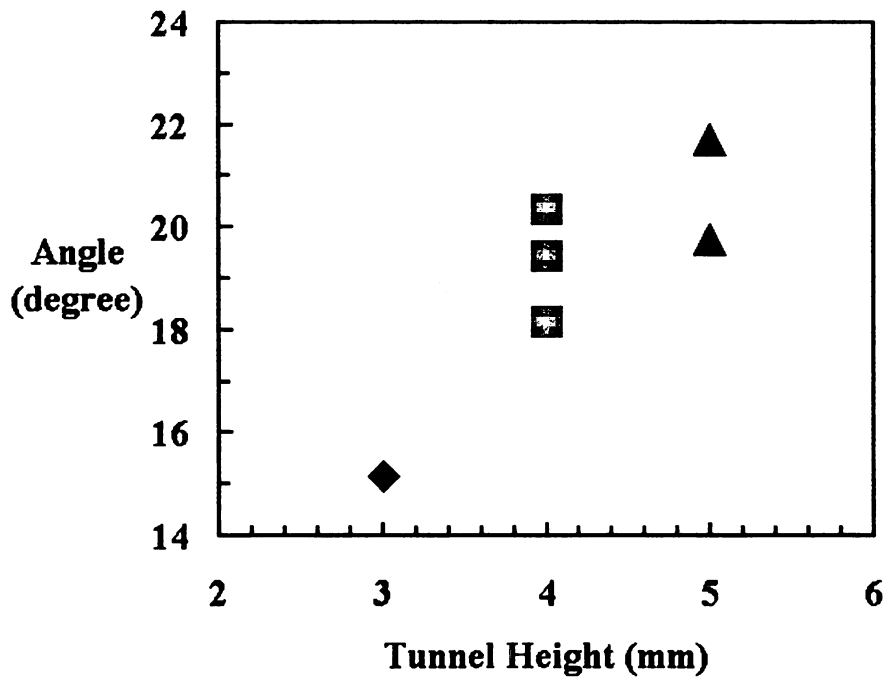

Figure 46. Bifurcation angle versus tunnel height for normal position of test facility.

4.3.2 Experiments in the Inverted Position

The average angles of bifurcation can be found in Figure 47 for experiments in the inverted position of the test facility, with tunnel heights of 3, 4, and 5 mm. The air velocities for each tunnel height are 3.5 cm/s, 3 cm/s and 2.5 cm/s, respectively. The trend is similar to the results in the normal position, the angle of bifurcation increases as the tunnel height increases. The values fall between 14° and 19°.

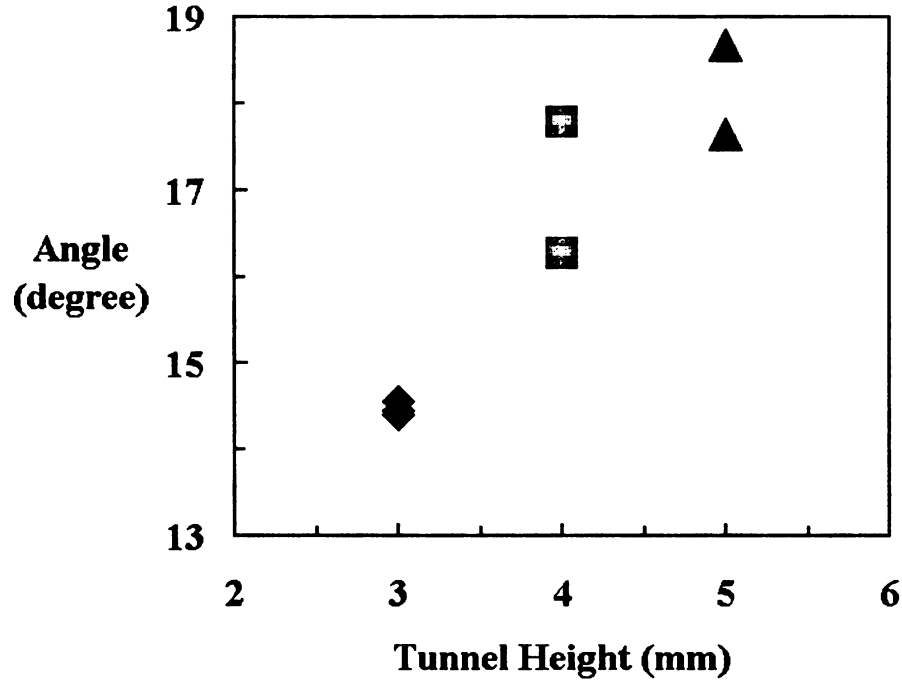

Figure 47. Bifurcation angle versus tunnel height for inverted position of test facility.

4.3.3 Summary of Bifurcation Angles

Table 5 lists the average bifurcation angle for tunnel heights 3, 4, and 5 mm with air velocities of 3.5, 3, and 2.5 cm/s, respectively, for both normal and inverted positions of the test facility. These numbers were plotted in Figure 48 for easy observation. The general trend is very clear that when the tunnel height increases the bifurcation angle increases as well. The bifurcation angle for experiments in the normal position, though, is higher than the bifurcation angle for experiments in the inverted position. The second-order polynomial trend lines were drawn, and they show significant increase from 3 mm to 4 mm for both positions of the test facility, although the normal position appears to be more major. From 4 mm to 5 mm the increase is more moderate for both positions of the test facility. This may happen because the 3 mm tunnel height experiments produced more flamelets initially; therefore there was little room for the flamelets to bifurcate laterally.

Overall the average lateral bifurcation angle ranges between 14° and 21°. This range is close to the lateral growth angle in [9], which value ranges from 15° to 23°.

Table 5. Summary of the average bifurcation angles for experiments in the normal and inverted positions at various tunnel heights and final air velocities

Position	Tunnel Height (mm)	Velocity (cm/s)	Bifurcation Angle (°)
Normal	3	3.5	15.17°
	4	3.0	19.30°
	5	2.5	20.70°
Inverted	3	3.5	14.51°
	4	3.0	17.02°
	5	2.5	18.16°

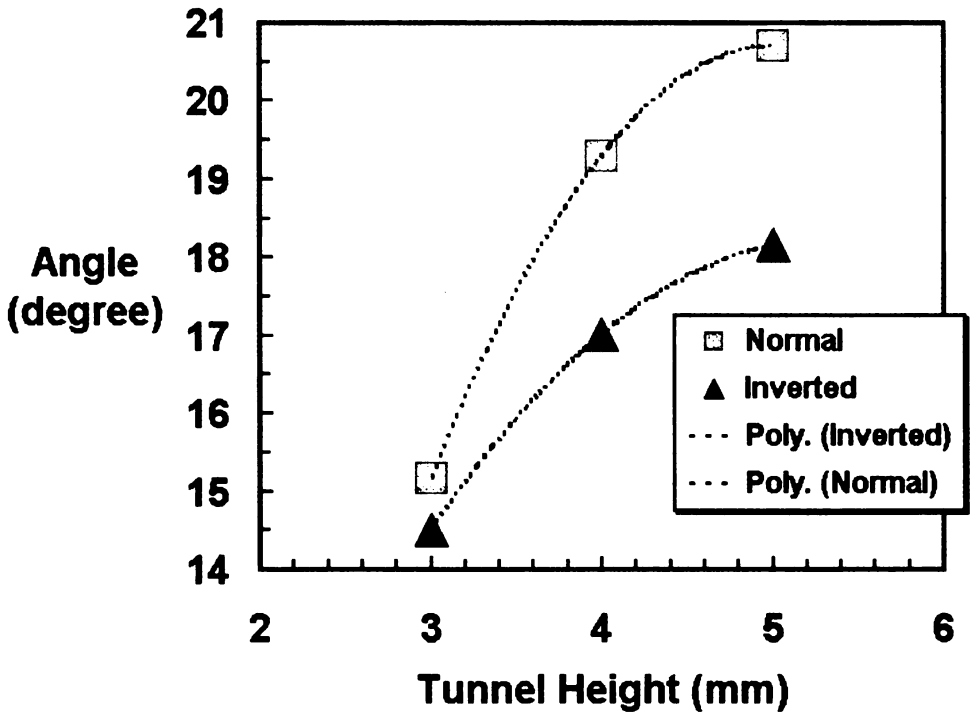

Figure 48. Average bifurcation angle versus tunnel height.

CHAPTER 5
FUEL SAMPLE BURNED AREA ANALYSIS

5.1 Overview

In further study of the flamelet, the fuel sample burned area analysis plays a major role. With this analysis, evaluation such as flamelet energy production can be done; and more prominently the oxygen consumption rate during combustion can be predicted. The prediction of the oxygen consumption rate along with the measurement of the flamelet spread rate are very useful to evaluate other studies such as the fuel-to-air ratio, flamelet power, and a few parameters for the population study using logistic model that will be discussed later in this thesis (Chapter 8). All of these topics will be discussed separately in sections 5.2 through 5.7, both for the normal and inverted positions of the test facility. Additionally, all necessary measurements were done utilizing the experimental video file as well as sophisticated computational software.

5.2 Fuel Sample Area Burned Fraction

5.2.1 Approach

The area burned measurement was done utilizing a software image analysis package TRACKER. The first task was to set the image scale from the image to user units in order to obtain results in the desired physical units. In TRACKER a suitable "threshold tracking" area of interest (AOI) was used to distinguish the burned area from the un-burned area by amplifying the color difference. Various image processing tools provided in the software can be deposited into the "image processing sequence." Then TRACKER recorded continuously, by small increments, the distance across the length of the sample. Figure 49 shows how the area burned measurement was done along with a list of the necessary image

processing tools that must be stored in the sequence. "Extract Plane-luminance" set the image in the AOI to a grayscale; "Threshold-Simple" set the bright color scale as white and the dark color scale as black; "Measurement-Area" measured the white and the black areas continuously; and "Threshold-Simple" was set by default. After measuring continuously with TRACKER, the fuel burned fraction was calculated using a reference point at the location of the ignition or at a point where the fuel was consumed uniformly.

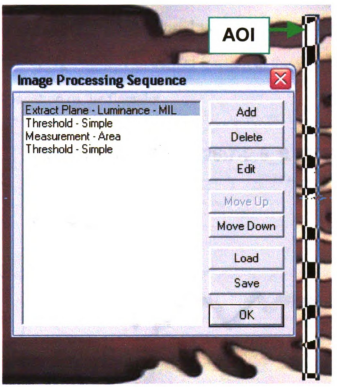

Figure 49. Measuring fuel sample burned area.

5.2.2 Experiments in the Normal Position

The burned area fraction ranges from 0 to 1. Where 0 is when the sample was not consumed at all, and 1 is when the sample was entirely consumed. In the plot, x-axis is the distance measured approximately from where the ignition was said to occur (this is an arbitrary location). The typical area burned fraction curve for experiments in the normal

position of the test facility can be found in Figure 50. This figure also represents the fuel burned fraction for tunnel heights 3, 4, and 5 mm with various final air velocities. The general shape of the burned fraction curve can be divided into three regions. The first region is the flat part, then the drop part, and the oscillatory part. These three regions correspond to the flame-front region, flame-front to flamelet transformation region, and the flamelet region, respectively. As appears in Figure 50, the flame-front region is flat because the flame-front uniformly consumed the fuel sample. Depending on the ignition, in some tests the flame-front was not linear and uniform, therefore the curve would not appear as flat as shown in Figure 50. The burned fraction in the flamelet region fluctuates depending on the propagation of the flamelet.

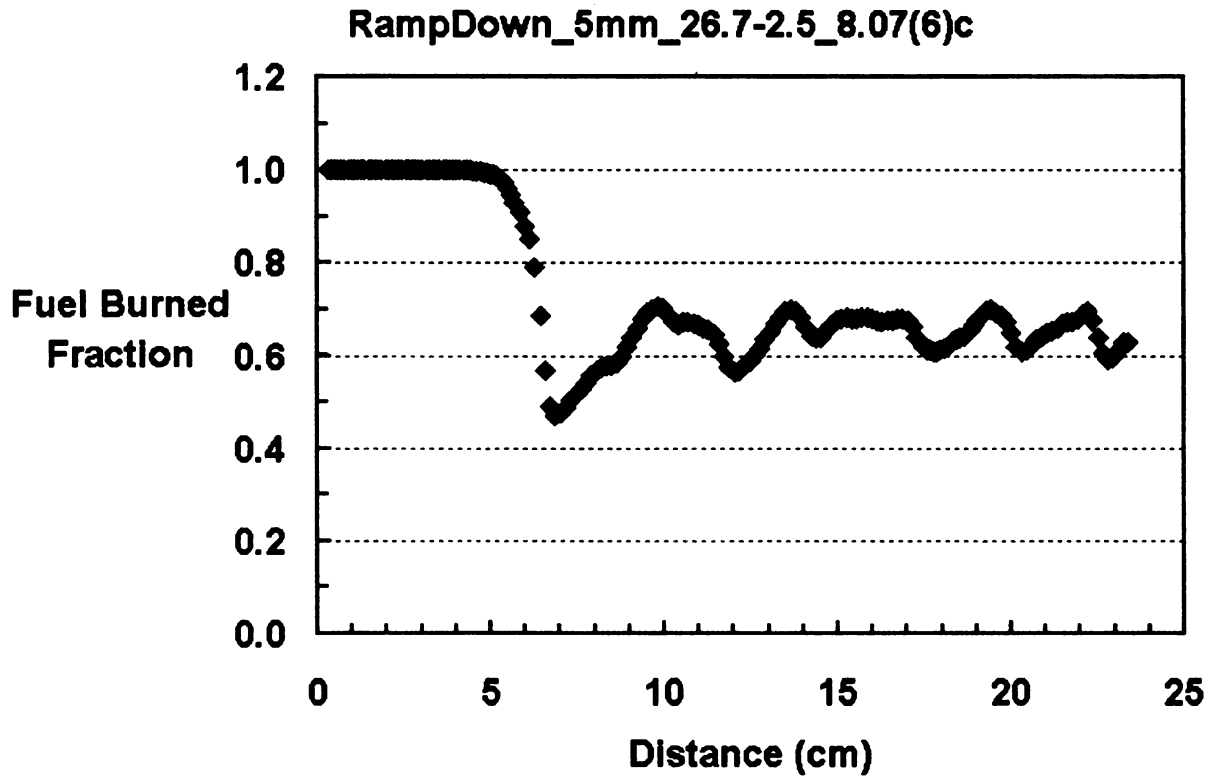

Figure 50. Area fuel burned fraction plot that represents results in the normal position of the test facility with tunnel heights 3, 4, and 5 mm and various final air velocities.

The fuel burned fraction shown in Figure 50 is from one of the tests with test conditions of 5 mm tunnel height and 2.5 cm/s final air velocity. The fingering pattern of this test (RampDown_5mm_ 26.7-2.5_8.07(6)c) can be found in Figure 51. Dotted lines were drawn to divide the three regions discussed earlier. The flamelet propagation was almost uniform across the sample. The result is shown in Figure 50, where the burned fraction variation is close to steady.

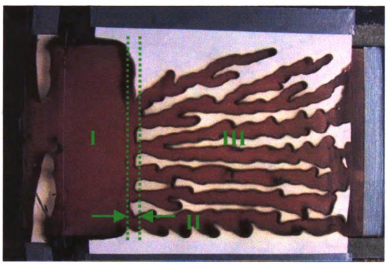

Figure 51. Three regions of test RampDown_5mm_26.7-2.5_8.07(6)c.

For each tunnel height, the air velocity was varied to see the effect on the burned fraction in the flamelet region. The result can be seen in Figure 52. As can be seen in Figure 52, the fuel burned fraction is proportional to the final air velocity and the tunnel height. This result is consistent with the flamelet population analysis. That is when the final air velocity and tunnel height increase, the flamelet population increases as well (more fuel consumption). In Figure 52, the average fuel burned fraction for most of the tests fall between 0.4 and 0.7, which means that most of the time flamelets consumed about 40% to 70% of the fuel sample. Roughly, the average burned fraction for all of the tests is about

58%. This number is comparable to the study performed at NASA [9], in which the fraction of fuel consumed for opposed flamelets is about 62%.

Linear trend lines for each tunnel height were drawn in the plot. The equations for these trend lines are $y_3=0.1248x+0.3095$, $y_4=0.1630x+0.0599$, and $y_5=0.1517x-0.2747$, for tunnel heights 3, 4 and 5 mm, respectively. As can be seen from the plot and the values of the slopes, the trend lines are almost parallel to each other.

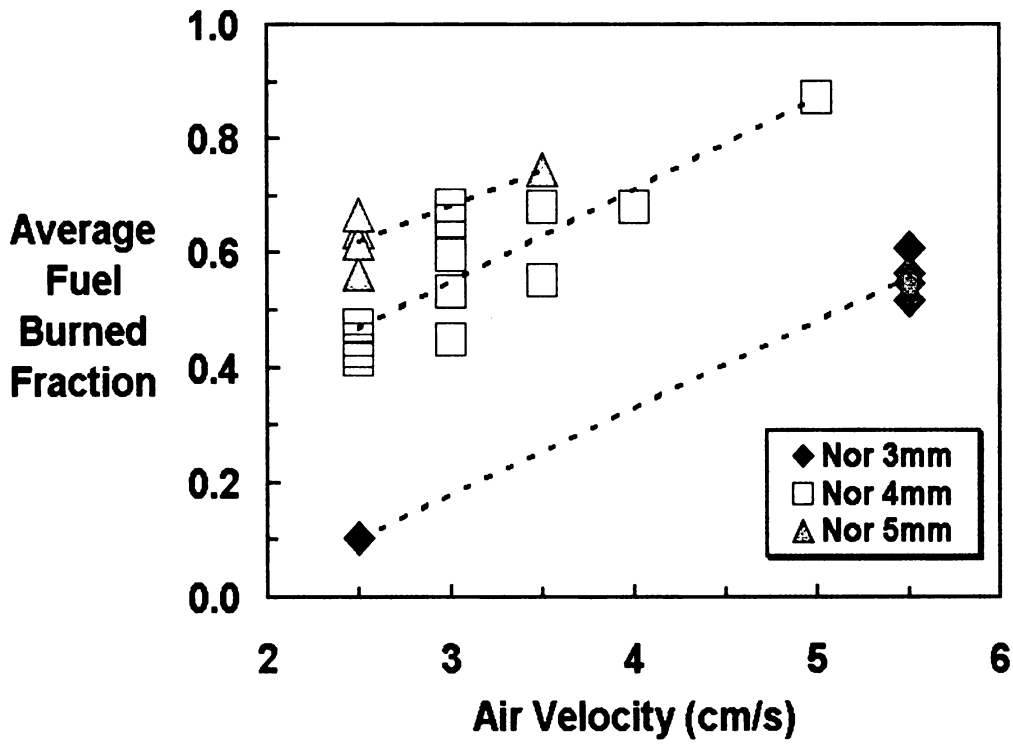

Figure 52. Burned fraction for experiments in the normal position.

5.2.3 Experiments in the Inverted Position

A fuel area burned fraction graph can be found in Figure 53. This graph represents the results in the inverted position of the test facility for various tunnel heights and final air velocities. The fuel burned fraction curves for experiments in the inverted position qualitatively agree with the results for the normal position of the test facility. The three

regions can be seen in Figure 53 like the three regions shown for the normal position. The fuel burned fraction shown in Figure 53 had test conditions of 3 mm tunnel height and final air velocity of 4.5 cm/s. It can be seen from the plot that there was not much fuel consumption.

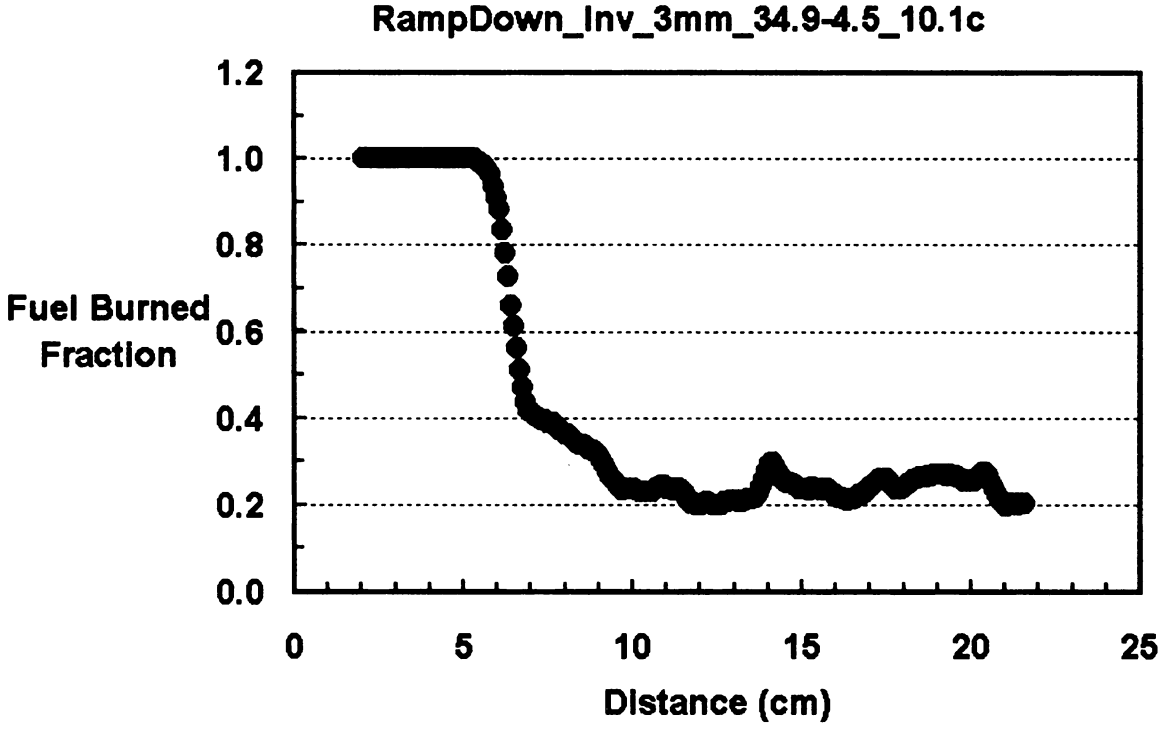

Figure 53. Fuel area burned fraction that represents the results in the inverted position of the test facility with tunnel heights 3, 4, and 5 mm and various final air velocities.

As before, the burned fraction for each tunnel height was compared for different final air velocities. Figure 54 shows the average of fuel burned fraction for experiments in the inverted position. As before, the results in the inverted position are similar to the normal position. Generally the burned fraction is proportional to the tunnel height and final air velocity. As the tunnel height and final air velocity increase, the burned fraction increases as well. Again, this agrees with the population analysis. When there were more

flamelets there was more fuel consumption. The average fuel burned fraction shown in Figure 54 mostly falls between 0.2 and 0.5. This means that in the inverted position, flamelets consumed about 20% to 50% of the fuel sample. Approximately, the average fuel burned fraction for all of the tests is 37%. This is about 21% lower than the average fuel burned fraction for experiments in the normal position. This may occur because of the difference in shape of the test section, such that the top portion was the heat sink where the bottom plate was the quartz glass.

The linear trend lines for each tunnel height were drawn and the equations are y_3=0.3218x-0.4047, y_4=0.2382x-0.3695, and y_5=0.1623x-0.4290 for tunnel heights 3, 4, and 5 mm, respectively. As can be seen from the plot that the lines are almost parallel to each other, however the values of the slopes affirm that they are not as good as the other results from the experiments in the normal position.

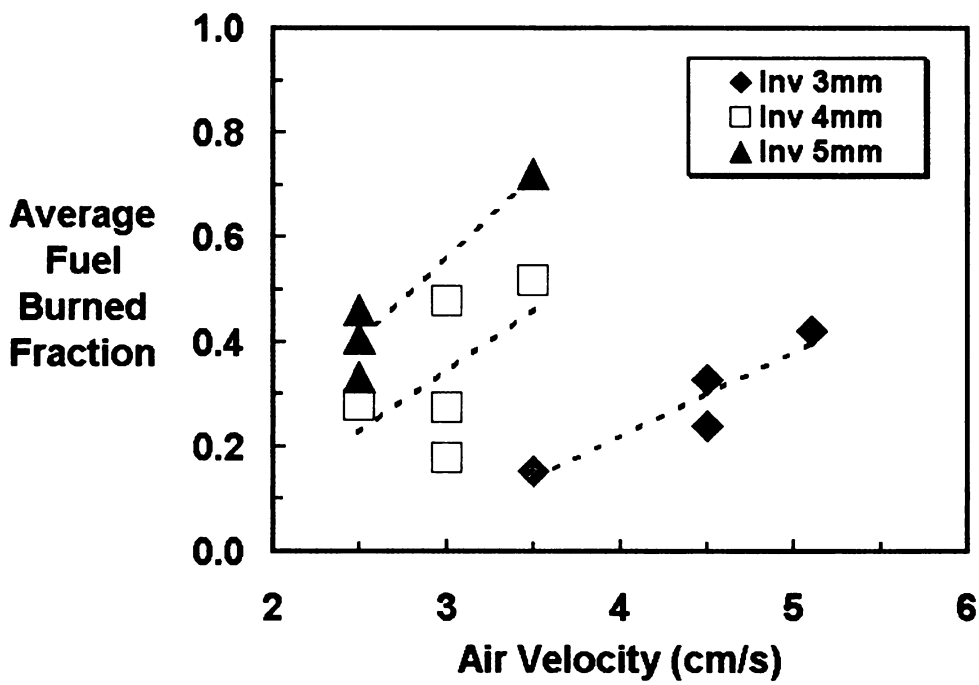

Figure 54. Average fuel burned fraction for experiments in the inverted position with tunnel heights 3, 4, and 5 mm and various final air velocities.

5.2.4 Flamelet Region in the Burned Fraction Curve

The burned fraction curve in the flamelet region shows a random fluctuating behavior that can be casually related to observe the flamelet behavior. The fluctuation, as described before, depends on the flamelet propagation. The peaks and the valleys of the burned fraction curve correspond to the bifurcations and extinctions that occurred during flamelet propagation. For example, Figure 55 that shows a fingering pattern of a test with a semi transparent burned fraction curve of the same test (RampDown_5mm_26.7-2.5 _8.07(6)c) superposed on top. The test was done with a 5 mm tunnel height and a 2.5 cm/s final air velocity.

Recall that in the burned fraction curve, 1 means that the fuel was entirely consumed, while 0 means that the fuel was not consumed at all. Therefore the peaks represent bifurcations while the valleys represent extinctions. In Figure 55 there were three solid lines drawn between distances 5 and 10 cm. The lines were identified as *a*, *b* and *c*. After the flame-front broke into five initial flamelets the burned fraction curve dropped quickly because flamelet spread left unburned material in between. Then between lines *a* and *b* the five initial flamelets spread and attempted to bifurcate. Thus, the burned fraction curve increased in response to the increased fuel consumption. The slight bump at line *b* was caused by two little flamelet extinctions indicated by the two crosses. Hence, the curve leveled slightly. Then, between lines *b* and *c* the curve increased as more fuel consumption occurred by flamelet bifurcation. Two bifurcations occurred between lines *b* and *c*, as indicated by the two red circles. Then at line *c*, the curve reached its highest point and dropped again. This was clearly because there were two flamelet extinctions, denoted

by the two crosses at line *c*. The drop however, was minor because there was a bifurcation (red circle past the line c) that counter balanced the extinctions.

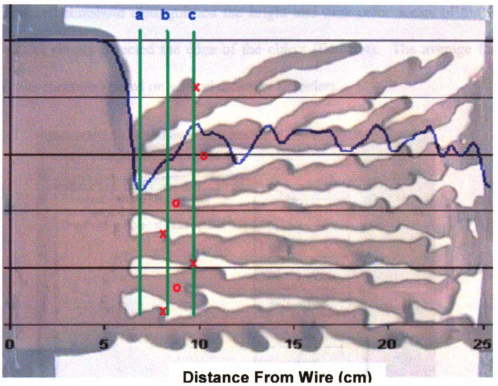

Figure 55. Burned fraction with its fingering pattern superposed on top.

5.3 Flamelet Spread Rate

5.3.1 Approach

The flamelet spread rate was measured using the image analysis software package called SPOTLIGHT[2] because of its capability to track the center of an object. SPOTLIGHT was similar to TRACKER. However, SPOTLIGHT had certain image processing tools that TRACKER did not provide such as "center tracking" AOI. It required a few "image processing sequences" to track the flamelet spread rate continuously. As

[2] SPOTLIGHT is a software image analysis package that was developed at NASA and is free for NASA contractors and grantees.

shown in Figure 56, the sequence consisted of "ExtractPlane-intensity", "Threshold-simple-inverse", "Filter-edge detect", and "Threshold-simple-standard" which appeared by default. The first threshold distinguished the bright and dark color scales of the image. The edge detect simply detected the edge of the object (flamelet). The average flamelet spread rate was measured based on several different flamelets.

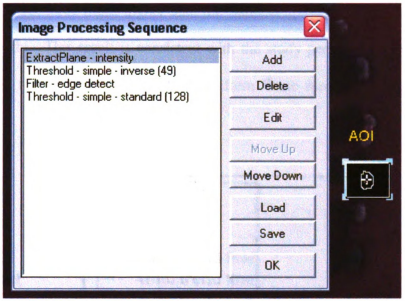

Figure 56. Measuring flamelet spread rate.

5.3.2 Experiments in the Normal Position

Applying the approach described above, the flamelet spread rate was plotted for the three different tunnel heights and for various final air velocities. The distribution can be observed in Figure 57. From the plot, it is shown that flamelet spread rate increases as the air velocity increases. Moreover, the flamelet spread rate increases as the tunnel height increases. At 2.5 cm/s and 3 cm/s final air velocities, the flamelet spread rate for different tunnel heights are within the same scale, as they appear to be very close to each other. The

flamelet spread rate plot in Figure 57 shows similarity with the flamelet spread rate plot [9] obtained at NASA (the plot can be found in appendix A, Figure A1).

As can be seen in Figure 57, the flamelet spread rate increases as the final air velocity increases. A few spread rate measurement for uniform or corrugated flame (higher final air velocity) was performed. The results show that the uniform or corrugated flame spread rate is about three times higher than the flamelet spread rate particularly for the 5 mm tunnel height. This result is consistent with the study performed at NASA. Where flamelet spread rate is said to be ⅓ of the uniform flame spread rate [9] (Appendix A, Figure A1).

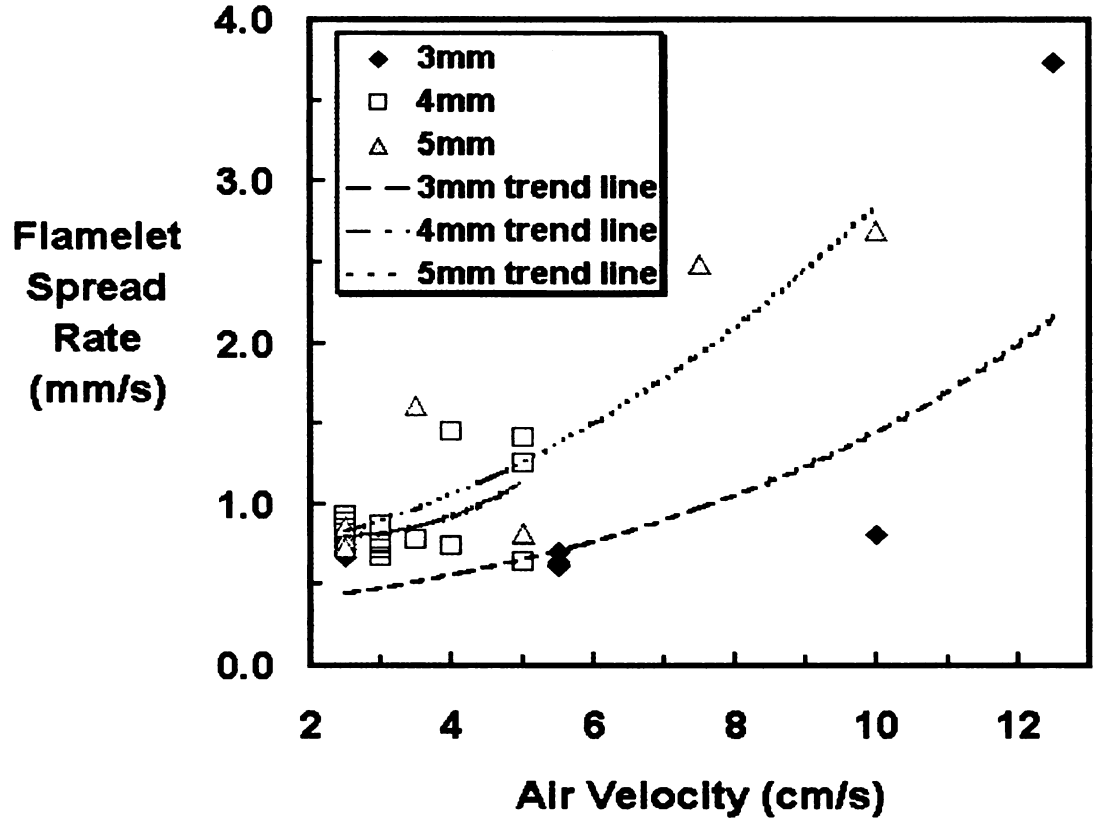

Figure 57. Flamelet spread rate for experiments in normal position of test facility with various tunnel height and final air velocities.

5.3.3 Experiments in the Inverted Position

Figure 58 shows the average flamelet spread rate for experiments in the inverted position. Generally the flamelet spread rate is proportional to the tunnel height and the final air velocity. Due to the low number of tests performed and the difficulty to track the flamelet in the inverted position (because they pulsed most of the time), there was only one test for the 4 mm tunnel height with a higher final air velocity. Comparing to the results in the normal position, the results in the inverted position show a slightly different pattern. For example, the 5 mm tunnel height shows a more significant increase from 3.5 cm/s to 4.5 cm/s final air velocities. While the 3 mm tunnel height shows a more moderate increase from 5 cm/s to 8.5 cm/s final air velocities. Again this occurred because of the difference in the test section tunnel geometry.

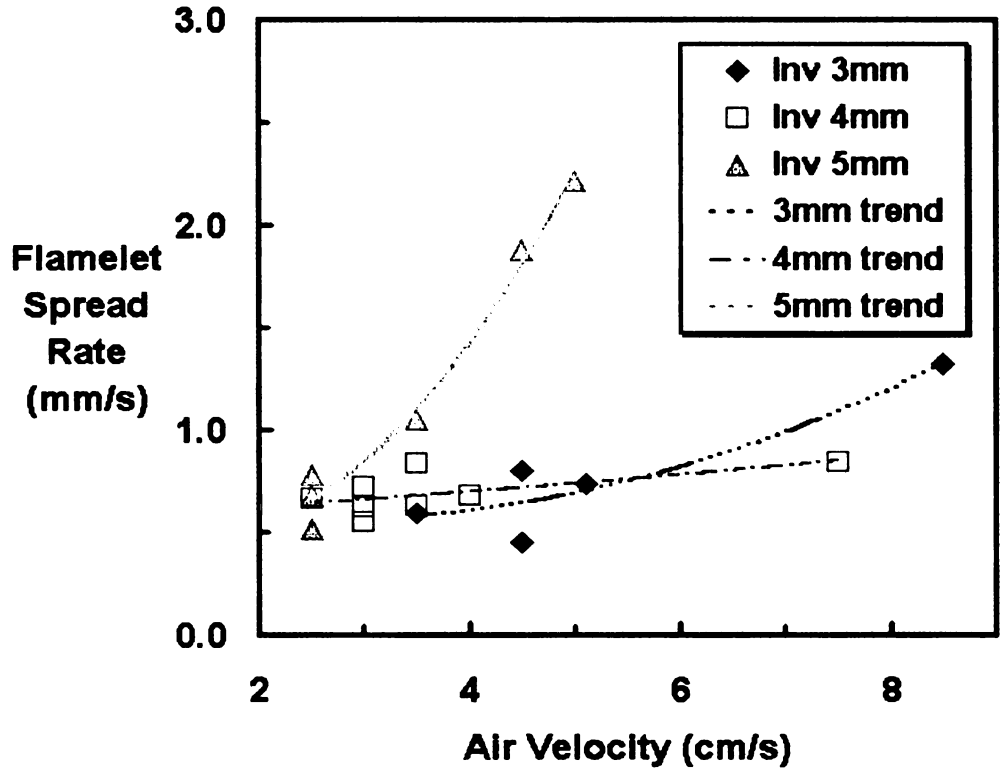

Figure 58. Flamelet spread rate for experiments in the inverted position of the test facility for various tunnel heights and final air velocities.

5.4 Per-Flamelet Heat Release Across Sample

The calculation of the per-flamelet heat release per unit length across the sample was initially based on many assumptions. The first assumption made was that the combustion reaction was stoichiometric. By definition, stoichiometric is when the amount of oxidizer is exactly the amount needed to burn completely a quantity of fuel. For cellulose (filter paper) and air (with a composition of 21% oxygen and 79% nitrogen, by volume), the reaction can be written as:

$$C_6H_{10}O_5 + 6(O_2 + 3.76\ N_2) \rightarrow 6CO_2 + 5H_2O + 22.56N_2. \qquad \text{(R1)}$$

For the above reaction, the mass ratio of air to fuel is shown in Equation (2). Here, MW_{air} (28.85 kg/kmol) and $MW_{C6H10O5}$ (162 kg/kmol) were the air and cellulose molecular weights, respectively. The 4.76 was the number of moles of air (3.76 moles of N_2 plus 1 mole of O_2), and 6 was the oxidizer coefficient.

$$\frac{m_{air}}{m_F} = \left[\frac{MW_{air} \cdot 4.76 \cdot 6}{MW_F}\right] = 5.08 \qquad (2)$$

5.4.1 Approach

The evaluation of the per-flamelet heat release per unit length across the sample was done using the burned fuel fraction and the flamelet spread rate data. The average per-flamelet heat release per unit length across the sample was according to Equation (3). Here, Y_{O2} was the oxygen mass fraction (0.233), and ρ_s was the cellulose area density (74 g/m^2). N and L were the number of flamelets and burned section, respectively.

$$Q(x) = 13.1MJ/kg_{O_2} \cdot 5.08 \cdot Y_{O_2} \cdot \rho_s \cdot (L_1/N_1) \cdot \int_0^x \Re(x)dx, \qquad (3)$$

where

$$\Re(x) = \frac{N_1}{L_1} \cdot \frac{L_x}{N_x}. \tag{4}$$

Then the instantaneous average heat release rate per-flamelet was according to Equation (5), where N_{avg} was the average number of flamelet, and v_f was the flamelet spread rate. The instantaneous heat release rate is expected to be proportional to the heat release per unit length because, except for the value of Q(x), everything else in the formula is constant.

$$\dot{q}_{avg} = \frac{Q(x) \cdot N_{avg} \cdot v_f}{\Delta x} \tag{5}$$

5.4.2 Experiments in the Normal Position

An example of the per-flamelet heat release per unit length across the sample plot can be found in Figure 59. This plot represents the results of the experiments in the normal

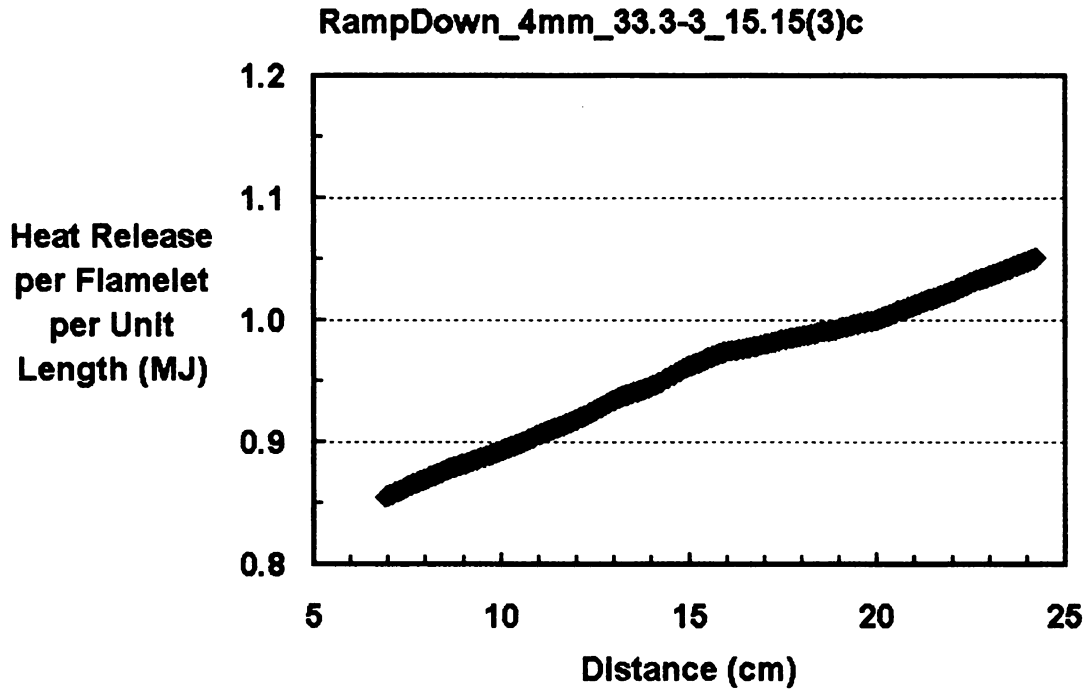

Figure 59. Per-flamelet heat release per unit length across the sample that represents the results in the normal position of the test facility for various tunnel heights final air velocities.

position for tunnel heights 3, 4, and 5 mm and various final air velocities. The heat release linearly increases. The results confirm the speculated plot in [15]. In [15], the straight line slope indicates that the overall per-flamelet heat release had reached steady state.

5.4.3 Experiments in the Inverted Position

The results of per-flamelet heat release per unit length across the sample for experiments in the inverted position are similar to the results shown for the normal position. Figure 60 represents the results of the experiments in the inverted position for tunnel heights 3, 4, and 5 mm and various final air velocities. As can be seen, the per-flamelet heat release linearly increases toward the end. Again, as it was speculated, this behavior suggests that a steady condition had been reached.

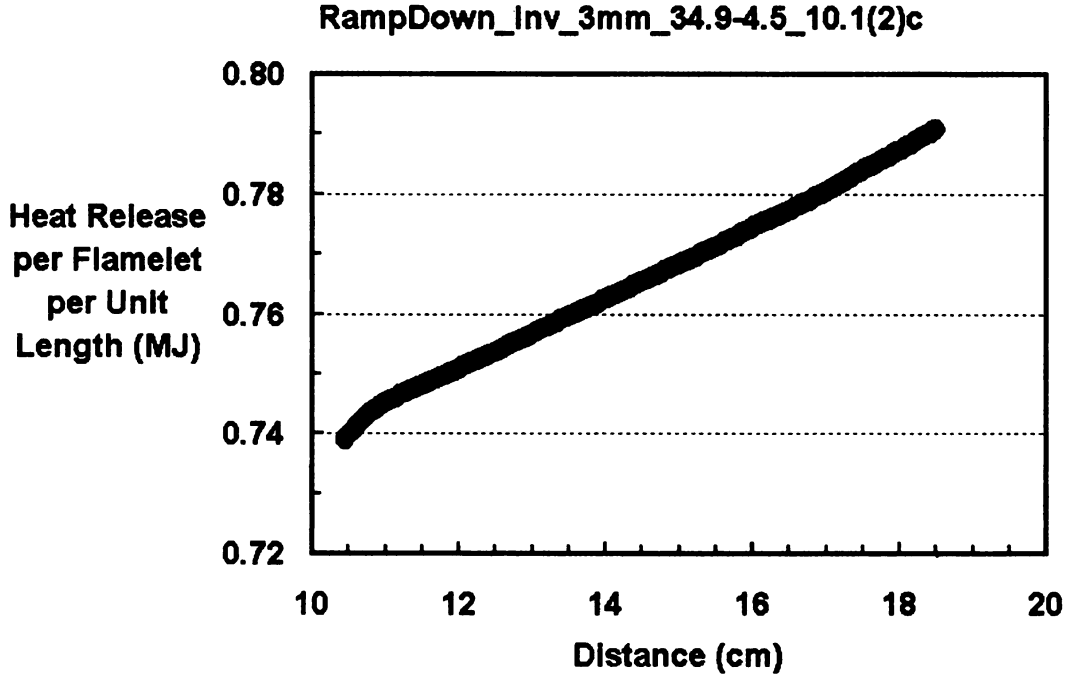

Figure 60. Per-flamelet heat release per unit length across the sample that represents the results in the inverted position of the test facility for various tunnel heights final air velocities.

5.5 Oxygen Consumption Rate

At the NASA Glenn Research Center the oxygen consumption rate was measured utilizing a special device. Unfortunately, the MSU Combustion Laboratory lacks appropriate equipment to measure the oxygen consumption rate. Since it was impossible to measure the oxygen consumption rate, some equations to predict the rate based on the known conditions were established. The oxygen consumption rate was predicted (not measured) using the area burned rate data as well as the flamelet spread rate data.

5.5.1 Approach

There were five equations established to predict the oxygen consumption rate. These five equations, though, assumed that the reaction was stoichiometric. The stoichiometric Reaction (R1) was described previously in Section 5.4.

The first equation to predict the oxygen consumption rate is expressed in Equation (6) below. Where dA/dt was the area burned rate, ρ_F was the cellulose area density and 6(32/162) was the stoichiometric oxygen-fuel molecular weight ratio.

$$\dot{O}_2 = \frac{dA}{dt} \cdot \rho_F \cdot 6 \cdot \frac{32}{162} \tag{6}$$

The second equation that predicts the oxygen consumption rate can be seen in Equation (7) below. This equation assumed that the oxygen heat of combustion was 13.1 MJ/kg_{O2}.

$$\dot{O}_2 = \frac{\frac{dA}{dt} \cdot \rho_F \cdot q_F}{q_{O_2}} \tag{7}$$

The third equation that predicts the oxygen consumption rate can be found in Equation (8). This equation assumed that the fuel heat of combustion was 17.5 MJ/kg $_{C6H10O5}$ (the value was obtained from the first law of thermodynamics, and will be discussed later in this section). The fuel surface temperature during the combustion was estimated as 700 K.

$$\dot{O}_2 = \frac{\frac{dA}{dt} \cdot \rho_F \cdot C_{PF} \cdot (T_S - T_O)}{q_F} \cdot 6 \cdot \frac{32}{162} \tag{8}$$

The fourth equation that predicts the oxygen consumption rate is stated in Equation (9). This equation was established assuming that the oxygen heat of combustion was 13.1 MJ/kg$_{O2}$, and the fuel surface temperature was 700 K.

$$\dot{O}_2 = \frac{\frac{dA}{dt} \cdot \rho_F \cdot C_{PF} \cdot (T_S - T_O)}{q_{O_2}} \tag{9}$$

Lastly, the fifth equation that was established to predict the oxygen consumption rate is expressed in Equation (10) below. This equation assumed that the cellulose (fuel) heat of combustion was 17.5 MJ/kg $_{C6H10O5}$. As can be seen in this equation, there are two common factors, q_F, which would cancel each other out. This causes Equation (10) to become exactly the same to Equation (6). Since this equation give the exact same results, this equation will not be discussed in the result and discussion section.

$$\dot{O}_2 = \frac{\frac{dA}{dt} \cdot \rho_F \cdot q_F}{q_F} \cdot 6 \cdot \frac{32}{162} \tag{10}$$

Notice in all five equations, Equations (6) to (10), that the variables that appear are all constants except "dA/dt". Consequently, the oxygen consumption rate is proportional to the area burned rate.

The value of 17.5 MJ/$kg_{C6H10O5}$ was obtained from the first law of thermodynamics. Since the energy of the reactants was equal to the fuel enthalpy of formation, the energy of the products was calculated according to Equation (11) with the assumption that the reaction was stoichiometric:

$$H_{products} = 5 \cdot \left(h^{o}_{f\,H_2O} + \Delta h_{H_2O}\right) + 6 \cdot \left(h^{o}_{f\,CO_2} + \Delta h_{CO_2}\right) + 22.56 \cdot \left(h^{o}_{f\,N_2} + \Delta h_{N_2}\right) \quad (11)$$

All the values of the h_f and Δh were selected at the ambient temperature (298 K). At 298 k, the values of the Δh terms were zero. By definition, the value of h_{fN2} was also zero. Once $H_{products}$ was found, the fuel heat of combustion can be calculated.

Once the oxygen consumption rate was predicted, the unconsumed oxygen rate can be predicted. The unconsumed oxygen rate was the difference between the constant inflow oxygen rate and the oxygen consumption rate. With this relationship, the unconsumed oxygen rate would be inversely proportional to the area burned rate. To evaluate the inflow oxygen rate, first the air mass inflow rate was determined using continuity. The property of air was taken at 298 K, the inlet area depended on the tunnel height, and the velocity was the final air velocity. Then, the inflow oxygen rate was the product of the air mass flow rate and the oxygen mass fraction. Table 6 lists all the constants involved to predict the oxygen consumption rate. In addition, unit verification to check the validity of the oxygen consumption rate equations can be found in Appendix A.

Table 6. Input variables to predict the oxygen consumption rate

Constants	Values	Units
ρ_F	0.074	kg/m^2
ρ_{air}	1.172	kg/m^3
MW_F	162	g/gmol
MW_{O2}	32	g/gmol
C_{PF}	11,704	J/kg*K
T_s	700	K
T_∞	298	K
q_F	17.5	MJ/kg_F
q_{O2}	13.1	MJ/kg_{O2}
Y_{O2}	0.233	
w	17.8	cm

5.5.2 Experiments in the Normal Position

The results of the predicted oxygen consumption rate from the four equations can be seen in Figure 61. This plot represents the results of the predicted oxygen consumption rate for experiments in the normal position of the test facility with various tunnel heights

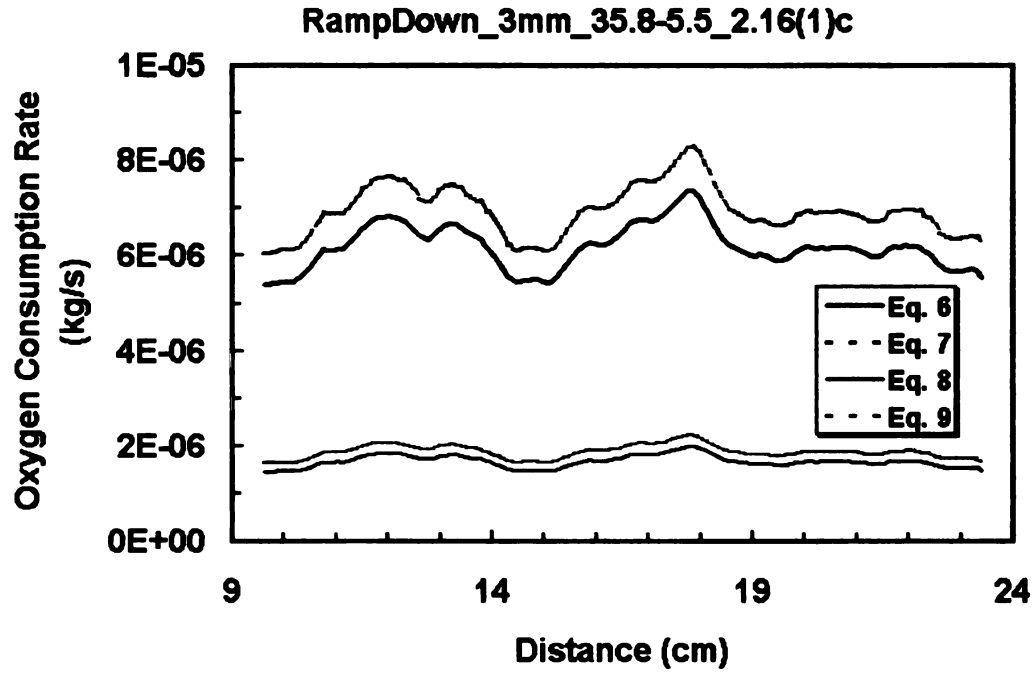

Figure 61. Predicted oxygen consumption rate plot that represents the results in the normal position of the test facility with various tunnel heights and final air velocities.

and final air velocities. The x-axis is the approximate distance from where ignition was said to occur. The oxygen consumption rate in the flame-front region was insignificant. Therefore the plot only included the oxygen consumption rate in the flamelet region. As can be seen in plot, the results using Equations (6) and (7) are close together, and the results using Equations (8) and (9) are close together but much lower compare to the results of Equations (6) and (7).

5.5.3 Experiments in the Inverted Position

The predicted oxygen consumption rate plot that represents the results in the inverted position of the test facility for three tunnel heights and various final air velocities can be found in Figure 62. Again, the results obtained using Equations (6) and (7) are close

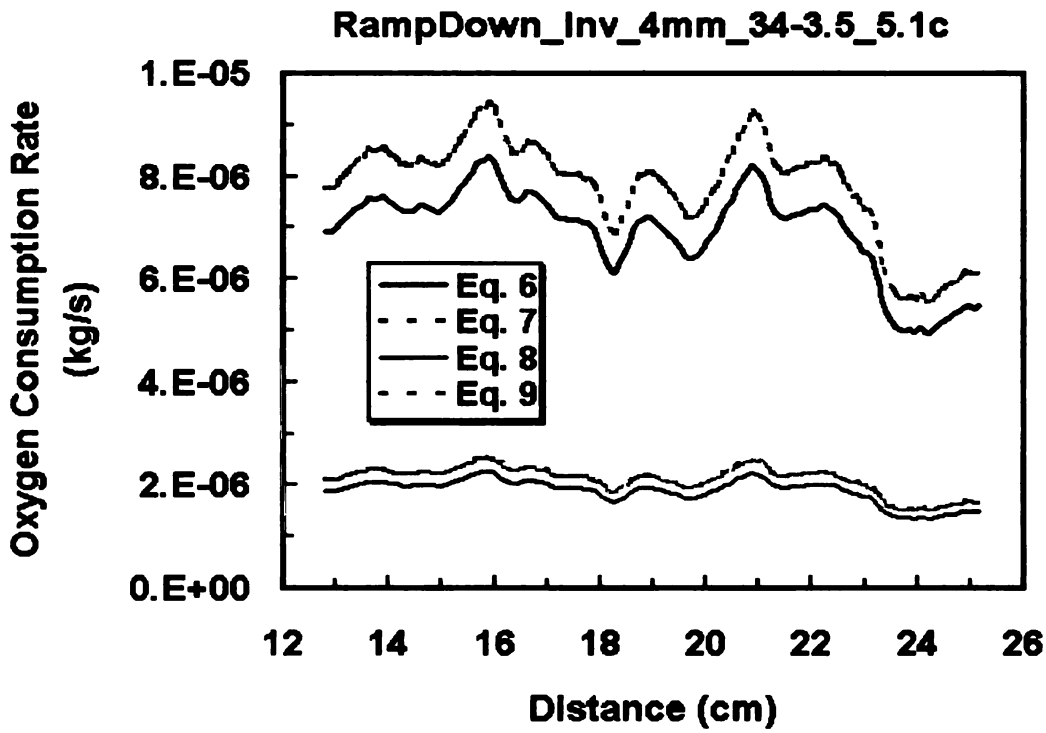

Figure 62. Predicted oxygen consumption rate plot that represents the results in the inverted position of the test facility with various tunnel heights and final air velocities.

together, and the results obtained from Equations (8) and (9) are close together, however, much lower than the results from Equations (6) and (7). Up to this point, it is still undetermined which one (or two) of these equations predicted more reasonable results.

5.5.4 Discussion

To compare the results of the four equations that predict the oxygen consumption rate, the average percentage of the unconsumed oxygen rate were outlined in Table 7. From the table, it can be seen that the predicted unconsumed oxygen rate from Equations (6) and (7) generally are lower than the results from Equations (8) and (9). For example the average in the normal position, the overall average for tunnel heights 3, 4, and 5 mm from Equations (6) then (8) are: 70%, 39%, 28% and 91%, 81%, 78%, respectively. The results from Equation (6) suggest that there was more oxygen consumed by flamelets during the combustion. Where the results from Equation (8) suggest that there was only 10% to 20% of the oxygen that flowed into the system was consumed. Therefore, it can be determined that the results using Equations (6) and (7) are more reasonable compared to the results from Equations (8) and (9).

Observing Table 7, it can be seen that the percentage of the unconsumed oxygen rate decreases as the tunnel height increases. This means that the there was more oxygen consumed by flamelets for larger tunnel heights. Between the normal and the inverted positions of the test facility, it can be seen that there was less oxygen consumed by flamelets in the inverted position. This result is consistent with the population analysis in Chapter 3. When there was less flamelets, clearly there was less amount of oxygen consumed.

Table 7. Summary of predicted unconsumed oxygen rate

Position	Tunnel Height (mm)	Air Velocity (cm/s)	Unconsumed Oxygen from Equation (6) (%)	Unconsumed Oxygen from Equation (7) (%)	Unconsumed Oxygen from Equation (8) (%)	Unconsumed Oxygen from Equation (9) (%)
Normal	3	2.5	85	83	95	96
		5.5	65	61	89	91
		10.0	74	71	92	93
		average	70	66	91	92
	4	2.5	40	32	82	84
		3.0	39	32	82	84
		3.5	35	29	78	80
		4.0	49	43	85	86
		5.0	38	31	80	82
		average	39	32	81	83
	5	2.5	28	19	78	81
Inverted	3	3.5	88	86	96	97
		4.5	82	80	95	95
		5.1	74	71	92	93
		average	81	79	94	95
	4	2.5	90	89	97	97
		3.0	82	80	94	95
		3.5	49	43	85	86
		average	77	74	93	94
	5	2.5	68	64	90	91

In predicting the oxygen consumption rate, there were some tests that showed unusual results. For example test number RampDown_5mm_26.7-2.5_12.1(7)c, whose unconsumed oxygen rate plot is shown in Figure 63. The unconsumed oxygen rate from Equation (7) reached to some negative values. Physically, this is impossible. There are a few reasons why this sometimes occurred in some tests. The first reason is the assumptions that were made when establishing the equations maybe slightly incorrect. Another reason that may cause this is that there were leaks in the system that allowed oxygen from the surroundings to act as additional sources of oxygen.

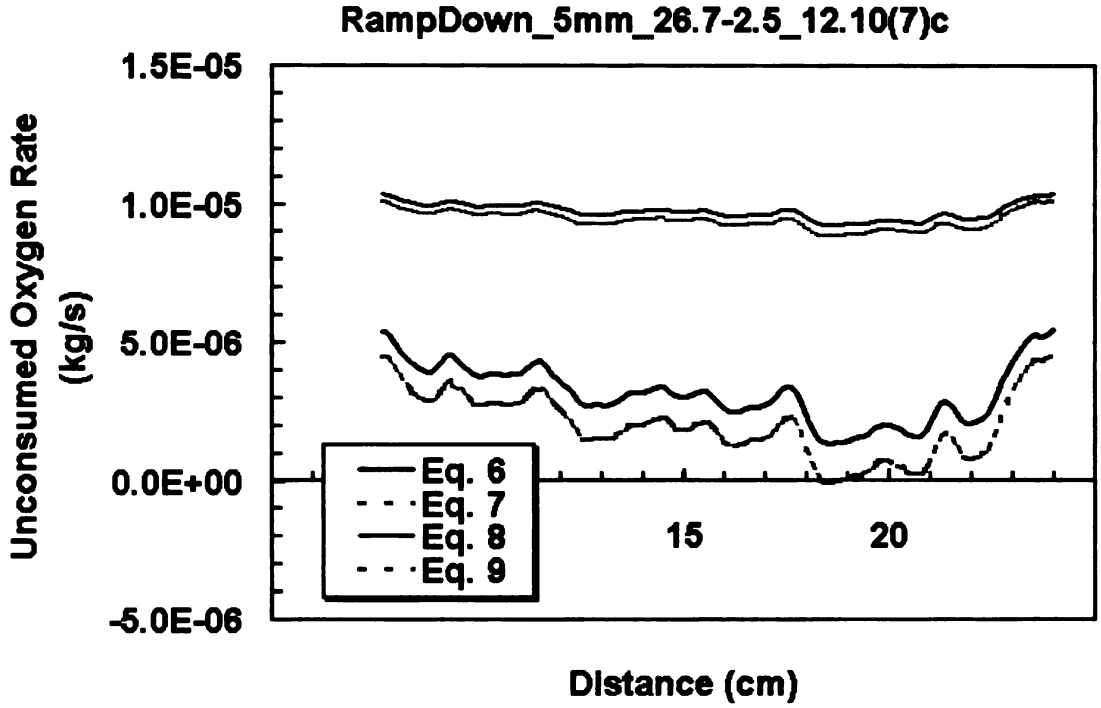

Figure 63. Predicted unconsumed oxygen rate with unusual occurrence.

5.6 Stoichiometric Ratio

Once the oxygen consumption rates were predicted, the global stoichiometric ratio can be estimated. Since there are four different equations that can be used to predict the oxygen consumption rate there are four different results of the global stoichiometric ratio that were obtained. However, for comparison purposes, only the results from Equation (6) will be presented in the results and discussion section.

5.6.1 Approach

Two important factors in evaluating the stoichiometric ratio [9] were the fuel burning rate and the oxygen consumption rate (which was predicted in section 5.5). The fuel burning rate equation can be found in Equation (12). The units for the fuel burning rate was $gmol_F/s$. Here v_f was the flame spread rate, f_{burned} was the fuel burned fraction, ρ_T was the fuel surface density, w was the sample width, and MW_F was the fuel molecular

weight. The oxygen consumption rate then can be expressed as in Equation (13) with unit of $gmol_{O2}/s$. The predicted oxygen consumption rate from the previous section was used in the $\Delta\chi_{O2}$ term. The global stoichiometric ratio then can be calculated according to Equation (14).

$$\dot{m}_F = \frac{v_f \cdot f_{burned} \cdot \rho_T \cdot w}{MW_F} \tag{12}$$

$$\dot{m}_{O_2} = \frac{\Delta\chi_{O_2} \cdot p \cdot U_\infty \cdot h \cdot w}{R \cdot T} \tag{13}$$

$$\Phi = 6 \cdot \frac{\dot{m}_F}{\dot{m}_{O_2}} \tag{14}$$

5.6.2 Results and Discussion

The average global stoichiometric ratios for both experiments in normal and inverted positions with various tunnel heights and final air velocities were tabulated in Table 8. When evaluating the global stoichiometric ratio, the results from using the oxygen consumption rate from Equation (9) are about three times higher than the values from the Equation (6). This confirms that Equations (6) and (7) produce more reasonable results than the results of Equations (8) and (9). Therefore the results using Equations (8) and (9) were ignored and not presented in this discussion.

The definition of stoichiometric combustion is when the amount of oxidizer is just the exact amount demanded to burn some amount of fuel completely. That is when the ratio of fuel-to-air is equal to unity. When the fuel-air ratio is >1, this means that the mixture is fuel-rich. And when the ratio is <1, it means that the mixture is fuel-lean. From

this definition, it can be said that the reaction of the burning sample paper is fuel-rich, since the values are all greater than 1. This agrees with the study performed at NASA [9]. The global stoichiometric ratio is 1.25, which is a fuel-rich.

Table 8. Summary of the average global stoichiometric ratio

Position	Tunnel Height (mm)	Air Velocity (cm/s)	Stoichiometric Ratio from oxygen consumption rate calculation using Eq. (6)
Normal	3	2.5	1.35
		5.5	1.31
		10.0	1.33
	4	2.5	1.27
		3.0	1.20
		3.5	1.13
		4.0	1.25
		5.0	1.21
	5	2.5	1.08
		3.5	1.08
Inverted	3	3.5	1.55
		4.5	1.51
		5.1	1.65
	4	3.0	2.05
		3.5	1.23
	5	2.5	1.37

5.7 Flamelet Power

5.7.1 Approach

There were four equations to predict the oxygen consumption rate. Therefore there are four results of the flamelet power. However, only the oxygen consumption rate from Equation (6) will be used in this section, since this equation produced more reasonable results. The flamelet power was evaluated by multiplying the oxygen consumption rate per flamelet by the oxygen heat of combustion. The unit of flamelet power is J/s or Watts.

5.7.2 Results and Discussion

The results of the flamelet power can be found in Table 9. The flamelet power calculations were done using the oxygen consumption rate results of Equation (6). The flamelet power increases as the air velocity increases. Moreover, flamelet has more power when the tunnel height is larger. Between the inverted and the normal positions of the test facility, flamelets in the normal position generally were brighter than flamelets in the inverted position. In fact, when running experiments in the inverted position it was noticeable that the inverted position always produced dim flamelets. Dimmer flamelets also occurred at low final air velocities.

Table 9. Summary of flamelet power

Position	Tunnel Height (mm)	Air Velocity (cm/s)	Flamelet power from oxygen calculation using Equation (6) (W)
Normal	3	2.5	8
		5.5	11
		10.0	31
	4	2.5	16
		3.0	14
		3.5	23
		4.0	18
		5.0	35
	5	2.5	18
Inverted	3	3.5	4
		4.5	6
		5.1	14
	4	2.5	8
		3.0	7
		3.5	13
	5	2.5	9
		3.5	28

CHAPTER 6
FLAMELET ANALYSIS

6.1 Background

There are three possibilities of combustion reaction for the burning cellulosic fuel sample. First the combustion could be a stoichiometric reaction. Then it is possible that the combustion reaction is fuel rich or fuel lean. The reactions describing the latter two reactions are shown in Reactions (R2) and (R3), respectively:

$$C_6H_{10}O_5 + (6+\beta)\,(O_2 + 3.76\,N_2) \rightarrow 6CO_2 + 5H_2O + \beta O_2 + (22.56+3.76\beta)N_2, \qquad (R2)$$

$$C_6H_{10}O_5 + (6-\beta)(O_2 + 3.76\,N_2) \rightarrow (6-2\beta)CO_2 + 5H_2O + 2\beta CO + (22.56+3.76\beta)N_2. \qquad (R3)$$

The first reaction contains excess oxygen. This is seen in the product side where the excess oxygen is indicated by β moles of O_2. The second reaction describes combustion with an oxygen deficit. It is shown by the excess carbon in the product side, that is the 2β moles of CO.

The challenge with these two reactions was to determine the value of β. However it was possible to determine the β value by looking at the physical behavior of the flamelets. An equation had been derived [15] relating the physical behavior of the flamelets to the determination of the value of β. The first step to determine the value of β is shown in Equation (15) below. N was the expected number of flamelets, r was the radius of the flamelets (here, it was assumed that the flamelet has a spherical shape), ρ_A and v_A were the air density and velocity, respectively. $H^* \cdot W^*$ was the area of oxygen consumed, D_F was the fuel diffusivity and Y_F was the fuel mass fraction.

$$N \cdot r = \frac{1}{2\pi \cdot 5.08 \cdot \left(1 + \frac{\beta}{6}\right)} \cdot \left[\frac{\rho_A \cdot v_A \cdot H^* \cdot W^*}{\rho_A \cdot D_F \cdot Y_F}\right] = \varepsilon \tag{15}$$

Rearranging Equation (15), Equation (16) was obtained. Equation (16) investigates the number of flamelets at a particular point by measuring the physical properties of the flamelets such as the radius, the gap between the flamelets, and the quench distance from the sample edge. Here, W^* is the sample fixed width, g is the gap between flamelets, and q is the quench distance.

$$N = \frac{W^* + g - 2q}{g + 2r} \tag{16}$$

6.2 Approach

All of the quantities shown in Equation (16) such as W*, g, q and r were measured using SPOTLIGHT. The measurement was done at various points across the sample, excluding the portion consumed entirely by the flame-front. In SPOTLIGHT, there was a line following AOI that was very useful. This tracking tool gave point coordinates for each pixel counted once a morphological outline was specified in the AOI. Just like TRACKER, SPOTLIGHT had various image processing tools that can be deposited in the line following the process sequence. The necessary sequences were "filter-smooth" to even out the pixels, "threshold-simple" was to distinguish the dark and bright color and "morphological-outline" was to draw lines between the bright and dark colors. Figure 64 shows the measurable quantities in Equation (16) while Figure 65 lists the processes done in SPOTLIGHT.

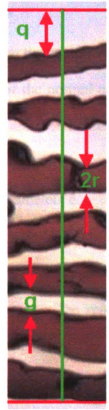

Figure 64. Fingering pattern segment showing the quantities q, g, and r (N = 7 and W* = 17.8 cm).

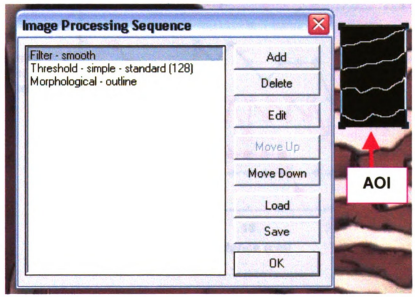

Figure 65. Line following process.

6.3 Average Number of Flamelets

The x-axis is the distance across the sample from approximately the location where the ignition took place. The results of the normal and inverted experiments were plotted together. In addition, the average number of flamelets were rounded up or down to the nearest integer value, since the number of flamelets must be an integer quantity.

The results of the number of flamelets equation, Equation (16), for the 3, 4 and 5 mm tunnel heights can be found in Figures 66, 67 and 68, respectively. In Figure 66, it can be seen, that generally the number of flamelets increases as the air velocity increases both for the normal and inverted experiments. The results for the 4 mm tunnel height are generally more bunched together. It still can be seen, however, that the average number of flamelets in the normal position is higher than the average number of the experiments in the inverted position.

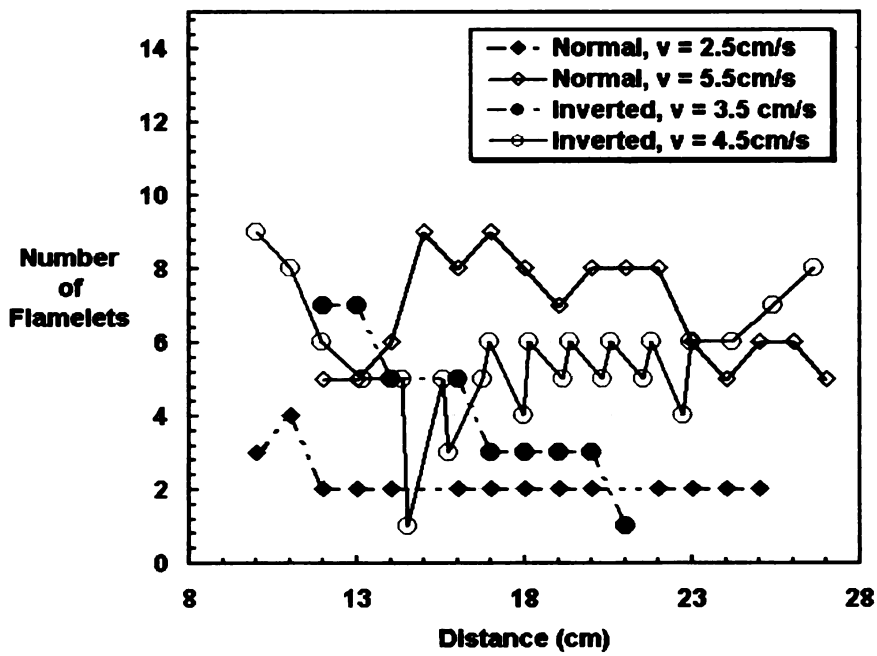

Figure 66. Average number of flamelets for 3 mm tunnel height.

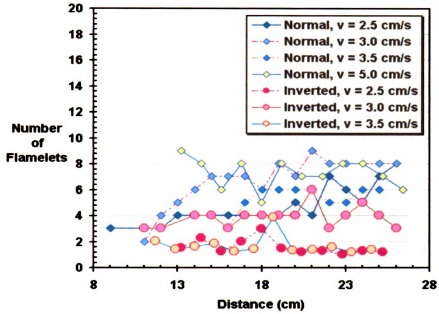

Figure 67. Average number of flamelets for 4 mm tunnel height.

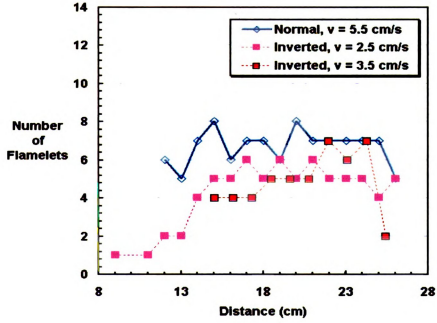

Figure 68. Average number of flamelets for 5 mm tunnel height.

The average number of flamelets for the 5 mm tunnel height can be found in Figure 68. Just like the previous two, Figure 68 shows that the number of flamelets in the normal

position is higher than the number of flamelets in the inverted position. These figures serve merely to formally quantity visual observations, from which are immediately recognizes this fact.

6.4 Flamelet Diameters, Gap Between Flamelets, and Quench Distance

Table 10 summarizes the measured quantities to evaluate the number of flamelets such as the quench distance, gaps between flamelets, and flamelet diameters. The numbers shown are the average values. These measurable properties, such as flamelet diameter, are useful to study the population analysis using the logistic model that will be discussed in the next chapter.

Table 10. Summary of flamelet diameters, gap spacing, and quench distance

Position	Tunnel Height (mm)	Air Velocity (cm/s)	Average flamelet diameter, (r) (cm)	Average flamelet gap spacing, (g) (cm)	Average quench distance, (q) (cm)	Number of flamelet calculated
Normal	3	2.5	1.22	4.81	4.96	2
		5.5	1.50	1.09	1.10	7
	4	2.5	1.63	1.93	2.55	5
		3.0	1.52	0.80	1.74	7
		3.5	1.93	1.21	1.57	5
		5.0	1.44	0.70	1.74	7
	5	2.5	1.75	0.71	1.32	7
Inverted	3	3.5	0.90	1.35	4.80	4
		4.5	1.13	1.29	3.30	5
		5.1	2.03	1.50	3.55	3
	4	2.5	1.57	0.81	7.43	1
		3.0	1.21	3.41	2.64	4
		3.5	1.67	1.07	0.99	6
	5	2.5	2.56	1.70	1.66	5
		3.5	2.74	1.55	0.35	5

CHAPTER 7
POPULATION MODEL

7.1 Background

The flamelet population demographics methods discussed in Chapter 3 shows that the cumulative population has an oscillatory behavior. This behavior happened in most of the tests. Both the NASA and MSU combustion groups had started to develop a theory to describe this behavior. A first-order non-linear differential equation that fits the experimental results had been developed. This model equation was based on biological animal population measures and had been used with some success [9] to describe various population behaviors. The general equation of the flamelets population model is

$$\frac{du}{dt} = a(t)\cdot u(t) - b(t)\cdot u(t)\cdot u(t-\tau). \tag{17}$$

The factors a(t) and b(t) may vary as functions of time. The last factor on the RHS has a time lag τ, indicating that the destruction of a population trails its creation. The simplest case occurs when the time lag, τ, is zero, hence factors a and b are constants, and $a/b = \kappa$. As $t \to \infty$, rearranging Equation (17) will produce Equation (18). Note that κ is known as the *carrying capacity*.

$$\frac{du}{dt} = a\cdot u(t)\cdot\left[1 - \frac{u(t)}{\kappa}\right] \tag{18}$$

A more complicated result occurs when τ is not equal to zero. In this case, the equation is non-linear and time-lagged. Letting $\rho = u/\kappa$, Equation (18) becomes:

$$\frac{d\rho}{dt} = \rho(t)\cdot[1-\rho(t-\tau)], \qquad \rho(0)=\rho_o. \tag{19}$$

This equation is solved numerically using numerical solution algorithms. These algorithms include the Euler method, the Modified Euler method (also known as the second order Runge-Kutta method), and the fourth order Runge-Kutta method. A computer software program was developed to yield an accurate graphical result. MATLAB student version 6.0 was used to operate the numerical solution of the equation using all the mentioned numerical solution methods. The MATLAB code was programmed systematically so one can enter inputs, and plot the output.

The Euler method is the easiest method, however, it is not very accurate compared to the modified Euler method. The Euler method is much less accurate than the fourth order Runge-Kutta method. Nevertheless for comparison purposes as well as to find more accurate numerical solutions, all the three methods were used. The Euler equation can be found in Equation (20). Here h is the time increment step size. The modified Euler and fourth order Runge-Kutta methods are presented in Equations (21) and (22), respectively.

$$y_{n+1} = y_n + hf(x_n, y_n), \qquad n = 0,1,2,\ldots \tag{20}$$

$$\begin{aligned} k_1 &= hf(x_n, y_n), \\ k_2 &= hf(x_{n+1}, y_n + k_1), \\ y_{n+1} &= y_n + \tfrac{1}{2}(k_1 + k_2), \end{aligned} \qquad n = 0,1,2,\ldots \tag{21}$$

$$
\begin{aligned}
k_1 &= hf(x_n, y_n), \\
k_2 &= hf(x_{n+\frac{1}{2}h}, y_n + \tfrac{1}{2}k_1), \\
k_3 &= hf(x_{n+\frac{1}{2}h}, y_n + \tfrac{1}{2}k_2), \qquad \text{n} = 0,1,2,\ldots \qquad (22) \\
k_4 &= hf(x_{n+1}, y_n + k_3), \\
y_{n+1} &= y_n + \tfrac{1}{6}(k_1 + 2\cdot k_2 + 2\cdot k_3 + k_4),
\end{aligned}
$$

7.2 MATLAB Code

The MATLAB code can be found in Appendix B. The code is presented as it is in the MATLAB command window. Based on how MATLAB works, the naming of the variables such as the time lag, increment time step and so on are different than in the equations described above. To avoid confusion, there are comments on each line. The comments are located after the percent (%) signs. The MATLAB code was divided into five major parts, for Euler method, Modified Euler method, fourth order Runge-Kutta method, error calculations between the three methods and the plotting commands.

7.3 Factors of Accuracy

There are numerous trials in developing the numerical solution programs. One of the major factors for obtaining more accurate solutions is the use of higher order differencing methods. Among the three methods used in this research, the simplest method is the Euler method. A higher order method is the Modified Euler method, which is accurate of $O(h^2)$. The highest order is the fourth order Runge-Kutta method, which is accurate to $O(h^4)$. Another factor in obtaining a more accurate solution is if the increment time step is small. The smaller the increment time step, the more accurate is the solution. The increment time step is denoted by h in Equations (20), (21) and (22), and *delta* in the MATLAB code of Appendix B.

In order to compare the three numerical solution methods, the MATLAB code of Appendix B included error norm calculations between the three methods. The goal is to produce an error magnitude that is as small as possible. The error norm is defined as

$$\|Error\| = \sum_{i=0}^{N} \sqrt{[y(t_i)_{method1} - y(t_i)_{method2}]^2} \,. \tag{23}$$

The following Figure 69 shows the three different results of the three numerical methods for different values of the numerical step size, *delta*. For comparison purposes the values of the time lag and final time were set to be 1.3 and 30 seconds, respectively. The first plot in Figure 69 shows the non-dimensional population with delta = 0.1. As can be seen in the graph, the modified Euler and the fourth order Runge-Kutta curves lay almost on top of each other, whereas the curve using the Euler method is separated from the others. The second plot in Figure 69 shows the non-dimensional population with delta = 0.01. As can be seen in the middle plot, all of the three curves converge and it is harder to see the difference. The curve using the Euler method appears also to agree with the others although it can still be seen that the Euler method still slightly deviates. In the third plot in Figure 69 shows the non-dimensional population with delta = 0.001. As shown, all of the three curves lay on top of each other, and it is hard to see any difference. Table 11 shows the summary of the norm error between the three methods for the three different delta values. Since it is obvious that the higher order of the numerical solution gives more accurate results, for the remaining study in this chapter, the scheme is of higher order is always used as the "standard".

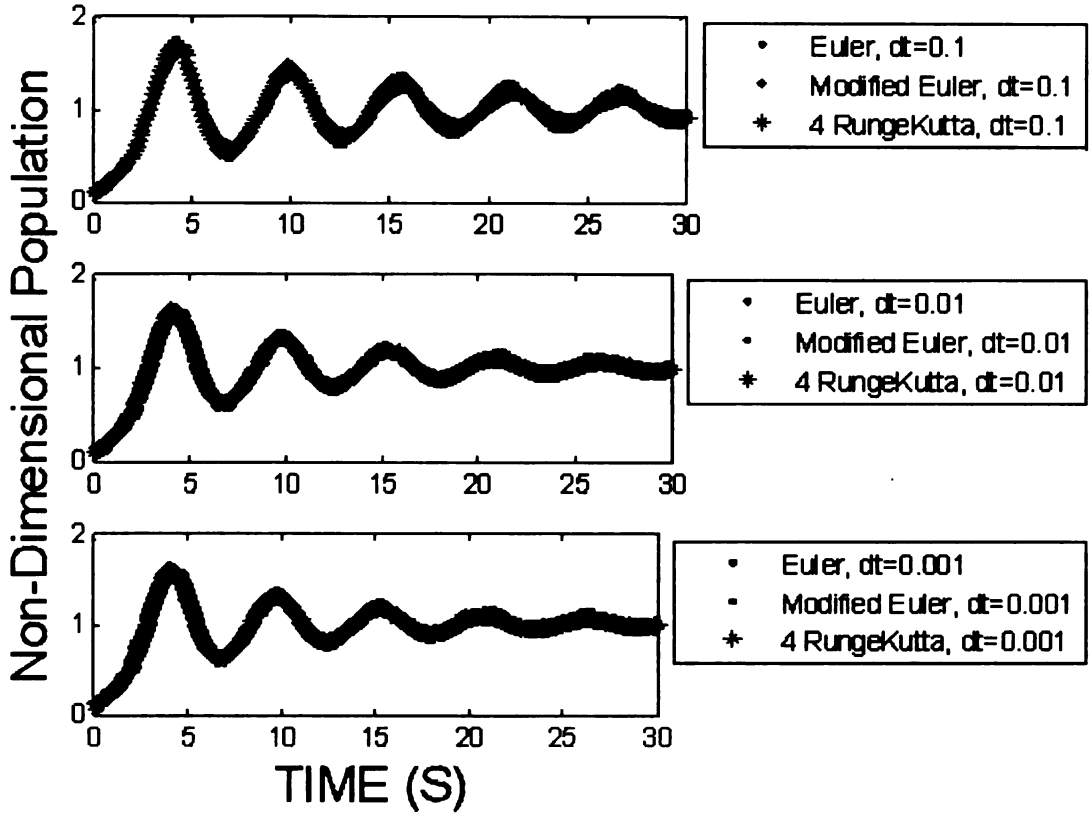

Figure 69. Non-dimensional population with delta = 0.1, 0.01 and 0.001 using Euler, Modified Euler and 4th Order Runge-Kutta methods.

Table 11. Error norm table

Delta	Euler v. Modified Euler	Euler v. 4th Runge-Kutta	Modified Euler v. 4th Runge-Kutta
0.1	1.300	1.349	0.049
0.01	0.331	0.332	0.001
0.001	0.103	0.103	3.42e-005

As can be seen in the table, the error norm approaches zero as delta decreases. However, the error norms between the Euler method and the other two methods are still larger than the error norm between the Modified Euler and the fourth order Runge-Kutta methods. Note also that when delta = 0.1, it required a short time (about 2 seconds) for the

program to generate the answers for the three methods. However, as the value of delta was reduced to 0.01, the program took more time to generate the answers. For the graph presented above, it required a longer time (about 5 seconds) to obtain the answers. Lastly, when the value of delta was reduced more to 0.001, it required a longer time (about 4 minutes) than the two smaller delta values to generate the answers and obtain the graphs that is shown above.

7.4 Time Lag

One of the major challenges encountered when developing the program was to include the 'time lag' term, τ, in the equation, Equation (19). The equation is already non-linear without the lag, and because of this 'lag' term the equation was much more difficult to solve numerically. Here, the MATLAB code was built with two loops in the program. The first loop was the linear loop; the second was the non-linear loop. Refer to Equation (19) and with a fixed 'lag' value, τ. First MATLAB would run within the linear loop. It is linear since the argument $(t-\tau)$ of the term $\rho(t-\tau)$is negative and this term is therefore neglected. In fact, the $\rho(t)\cdot\rho(t-\tau)$ is set to zero when $t < \tau$. When $t = \tau$ this term takes the value $\rho(\tau)\cdot\rho(0)$ and when $t = \tau+\Delta t$ it is $\rho(t+\Delta t)\cdot\rho(\Delta t)$, etc. When $t \geq \tau$ the MATLAB code would jump to the second loop, the non-linear loop where the term $\rho(t-\tau)$ would be included in the computation. Consider the simple sample calculations shown in Table 12. Using the Euler method with the increment time step, delta = 0.5, initial condition $\rho(0)$ = 1/10, and time lag τ = 1. The calculations are from the difference formulas given by Equations (24) and (25) for the linear and non-linear portions, respectively. Note that

Equations (24) and (25) are the rearranged first order (Euler) finite-difference version of Equation (19):

$$\rho(t+\text{delta}) = \rho(t) + \text{delta} \cdot \rho(t) \cdot [1], \tag{24}$$

$$\rho(t+\text{delta}) = \rho(t) + \text{delta} \cdot \rho(t) \cdot [1- \rho(t-\tau)]. \tag{25}$$

Table 12. Sample calculations of the population equation

t	$\rho(t-\tau)$	Equation	$\rho(t+\text{delta})$
0	$\rho(0-1) = \rho(-1)$ $(\rho(-1) \rightarrow 0)$	(24)	$\rho(0.5) = \rho(0) + \text{delta} \cdot \rho(0) \cdot [1]$ $= 0.1 + 0.5 \cdot 0.1 \cdot [1]$ $= 0.15$
0.5	$\rho(0.5-1) = \rho(-0.5)$ $(\rho(-0.5) \rightarrow 0)$	(24)	$\rho(1) = \rho(0.5) + \text{delta} \cdot \rho(0.5) \cdot [1]$ $= 0.15 + 0.5 \cdot 0.15 \cdot [1]$ $= 0.225$
1	$\rho(1-1) = \rho(0)$ $(\rho(0) = 0.1)$	(25)	$\rho(1.5) = \rho(1) + \text{delta} \cdot \rho(1) \cdot [1- \rho(1-1)]$ $= 0.225 + 0.5 \cdot 0.225 \cdot [1-0.1]$ $= 0.326$
1.5	$\rho(1.5-1) = \rho(0.5)$ $(\rho(0.5) = 0.15)$	(25)	$\rho(2) = \rho(1.5) + \text{delta} \cdot \rho(1.5) \cdot [1- \rho(1.5-1)]$ $= 0.326 + 0.5 \cdot 0.326 \cdot [1-0.15]$ $= 0.465$
2	$\rho(2-1) = \rho(1)$ $(\rho(1) = 0.225)$	(25)	$\rho(2.5) = \rho(2) + \text{delta} \cdot \rho(2) \cdot [1- \rho(2-1)]$ $= 0.465 + 0.5 \cdot 0.465 \cdot [1-0.225]$ $= 0.645$

MATLAB works according to the same basic technique shown in Table 12 though with much finer time steps, delta.

To see the effect of the time lag, the value of delta was set to 0.001. The value of τ was given the values 0.9, 1, 1.2, and 2. The results can be seen in Figures 70 (for $\tau = 0.9$ and 1) and 71 (for $\tau = 1.2$ and 2). As can be seen in all of the plots, the time lag influences the oscillation pattern. The larger the time lag, the more extreme the oscillation becomes.

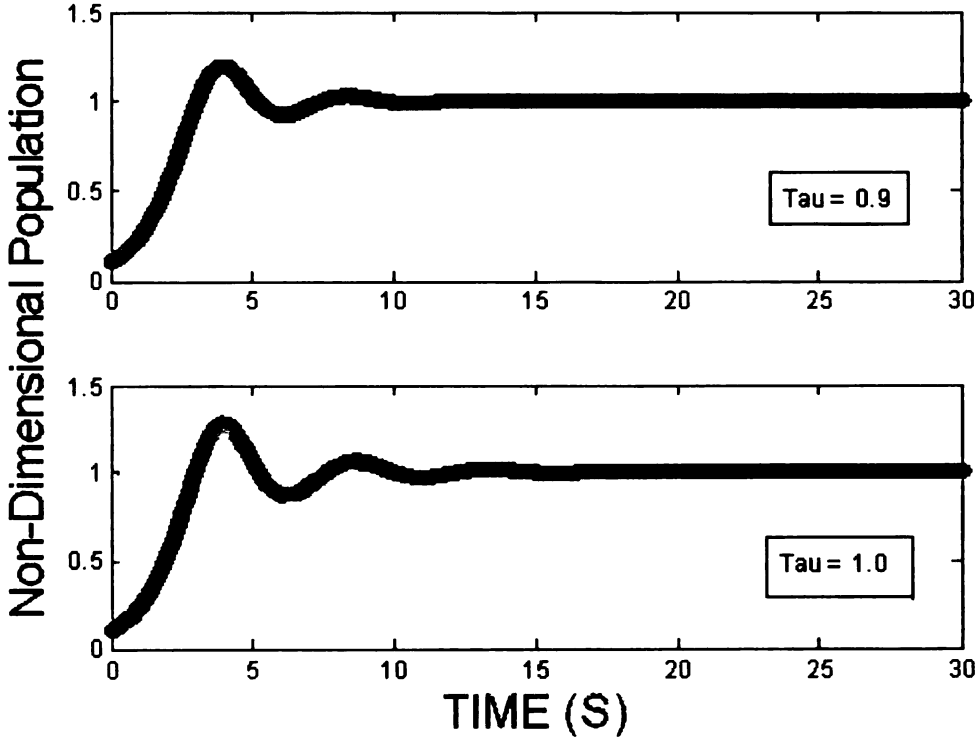

Figure 70. Population with time lag = 0.9 and 1.0.

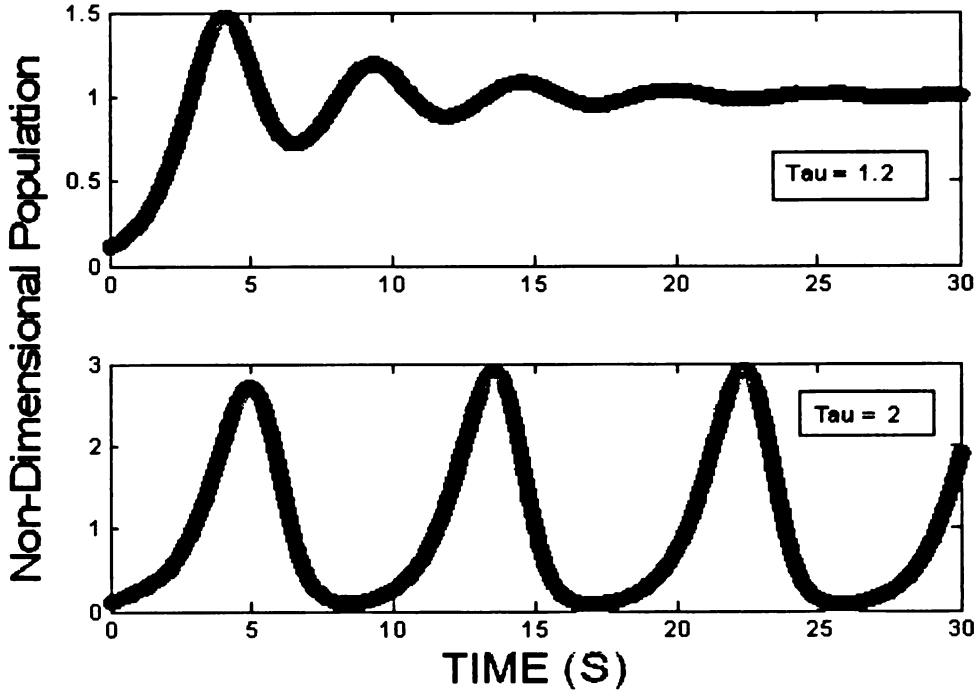

Figure 71. Population with time lag = 1.2 and 2.

7.5 Vibration Analyses

This first order differential equation has a non-linear term that produces an oscillating curve that resembles the basic oscillation that occurs in free excitation vibration with an under damped response. Therefore it is possible to analyze the problem from the vibration point of view. Some computations that can be made using ideas from vibrations include evaluating the period, frequency and the settling time of the oscillation. Another analysis that can be done using the observable peaks is to compute the damping ratio of the oscillation.

Refer to the MATLAB code laid out previously. In the non-linear loop there are loops that evaluate the peaks and the valleys of the oscillation with their corresponding occurrence times. In the peak loop, there are loops that evaluate the period, the frequency, as well as the log decrement. The period can be evaluated by taking the difference between the times of two successive peaks. For example, peak A occurs at time t_1, and peak B occurs at time t_2. The period is then t_2-t_1. Once the period is evaluated, the frequency can be found according to the following correlation.

$$f = \frac{1}{period} \tag{26}$$

Clearly, this frequency may vary with the duration of oscillation. As $t \to \infty$ it can be determined that $f \to \infty$, for example it is shown in the top plot in Figure 71.

The settling time is useful to predict when the oscillation will reach a steady state. The settling time occurs at the 2% mark from the center of the oscillation. The last peak that touches this 2% limit is defined as to be the settling time. For example, consider

Figure 72. Shown are the population curves for the three methods, where delta = 0.001, a time lag τ = 1.2 and an expended time range of to 50 seconds. Shown in the figure is the 2% limit line, which is defined as the line 1.02 from the center of the oscillation at 1.00. The settling time peak occurs at the peak value indicated in the figure. The settling time for this case occurs at t = 25.805 seconds for the modified Euler, and fourth order Runge-Kutta methods, and t = 25.806 seconds for the Euler method. As can be seen in the figure, after t = 25.805 the curve starts to reach the steady state and it no longer crosses the 2% limit line.

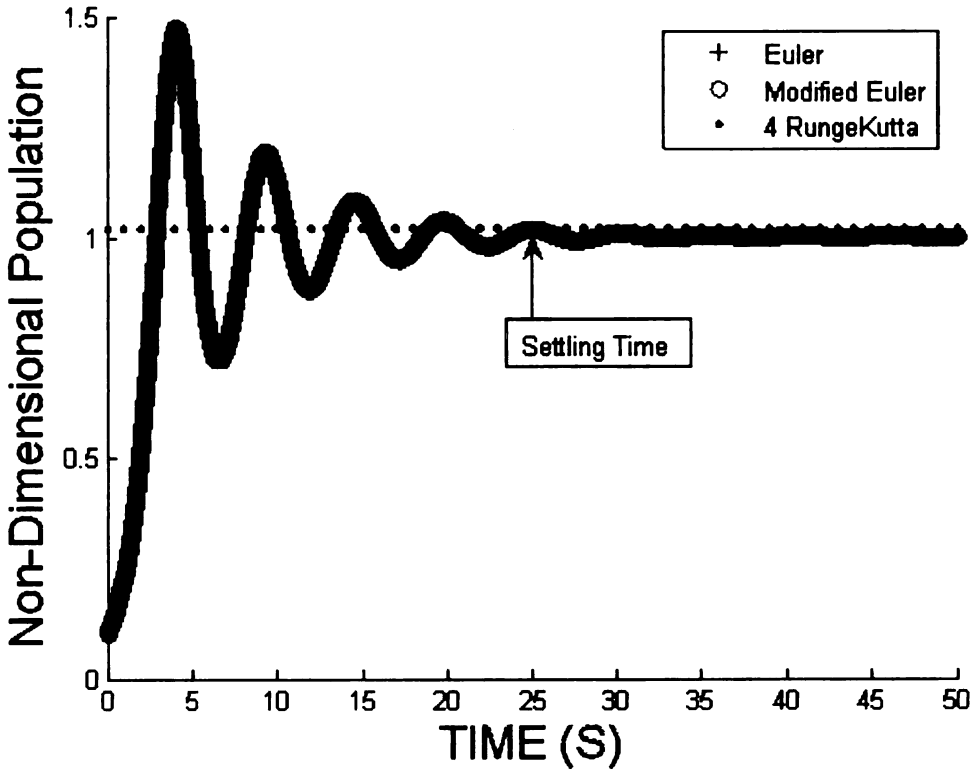

Figure 72. Settling time peak.

The damping ratio can be evaluated using the following relations; where δ is the log decrement of two consecutive peaks, x is the peak value, and ζ is the damping ratio. Since there are several peaks, an average value of δ is used when evaluating the damping ratio, ζ.

$$\delta = \ln\left(\frac{x_s}{x_{s+1}}\right) \tag{27}$$

$$\zeta = \delta_{avg} / (2\pi) \tag{28}$$

As an example of the evaluation of the damping ratio, consider the non-dimensional population shown in Figure 72. Using the results of the fourth order Runge-Kutta method, the damping ratio evaluation can be found as in Table 13. Then using Equations (27) and (28), the average of $\delta = 0.074$; therefore, $\zeta = 0.012$.

Table 13. Log decrement

	S=0	S=1	S=2	S=3	S=4
X_{1+s}	1.47	1.19	1.08	1.04	1.02
$\ln(x_1/x_{1+s})$	0	0.21	0.10	0.04	0.02

7.6 Temporal Perturbation of the Population Equation

Recall Equation (18), and where the carrying capacity factor κ simply had a(t) and b(t) equal to constants. It may be important to involve other factors that affect the population of the flamelets, such that a(t) and b(t) are not constants. Now consider a(t) and b(t) are equal to some function, say, $a(t) = b(t) = 1+\varepsilon\cdot\sin(\omega\cdot t)$, in addition to the variable τ. Then Equation (18) becomes:

$$\frac{du}{dt} = a(t)\cdot u(t)\left[1 - \frac{b(t)}{a(t)}\cdot u(t-\tau)\right]. \tag{29}$$

Since a(t) = b(t), Equation (29) becomes:

$$\frac{du}{dt} = (1 + \varepsilon \cdot \sin(\omega t)) \cdot u(t) \cdot [1 - u(t - \tau)]. \tag{30}$$

Notice that as $\varepsilon \to 0$ the equation essentially will become Equation (19). Additionally, the value of ω is about the value of the period of the curve using Equation (19).

To observe the affect of the additional sinusoidal function in the equation, the following Figures 73 and 74 were obtained using delta = 0.001, and time lag $\tau = 1.2$. $\omega = 5.24$ (or about $3\pi/2$) and ε was assigned to 1.5, 1, 0.5 and 0.01. Note that in these figures only the fourth order Runge-Kutta methods was used. As can be seen from this set of figures, the influence of the factor ε on the population is that the curve is undergoing transition from rough to smooth, as the value of ε approaches zero.

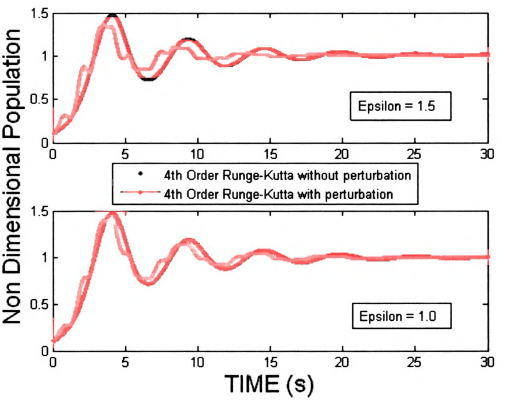

Figure 73. Population with $\varepsilon = 1.5$ and 1.0.

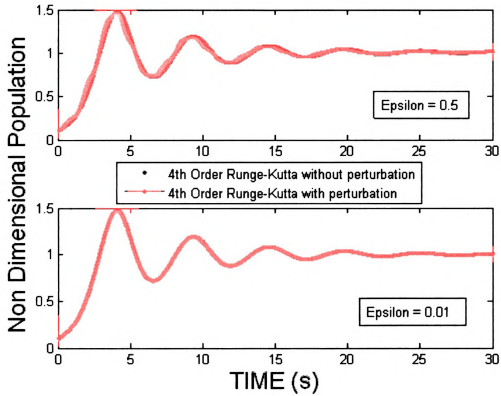

Figure 74. Population with $\varepsilon = 0.5$ and 0.01.

In addition, to observe the affect of ω on the modified population model, Figures 75 and 76 were obtained. Only the fourth order Runge-Kutta method was used for this comparison. One of the curves had the value of $\varepsilon = 0$ (unperturbed curve). The time lag and delta were set to 1.2 and 0.001. The value of ω was varied while ε was set to 0.5 in the Euler method using the equation containing the sinusoidal function. Apparent in these figures is that the curve becomes more stable as the value of ω approaches 2π. This is expected because sinusoidal functions repeat themselves every 2π radians.

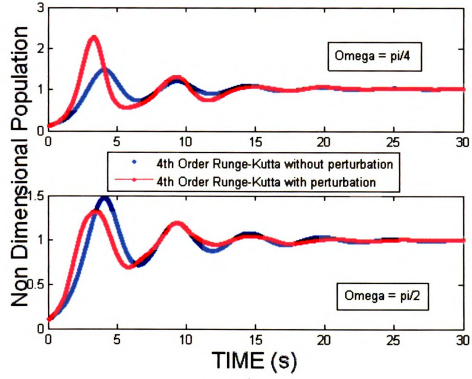

Figure 75. Population with $\omega = \pi/4$ and $\pi/2$.

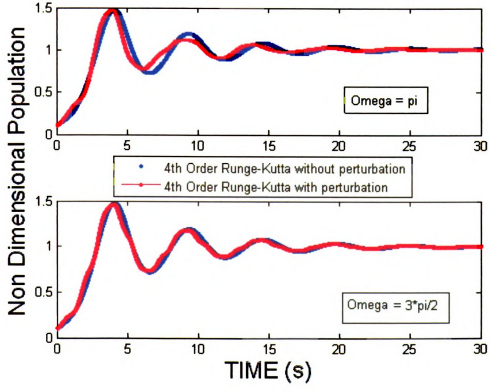

Figure 76. Population with $\omega = \pi$ and $3\pi/2$.

7.7 Comparison with Experimental Data

The population model so far had been developed as shown in Equation (30). The next step in the further study of this population model was to compare the numerical results with the experimental data. The experimental data shown in Figure 77 test RampDown_3mm_35.8-5.5_2.16(1)c has obvious an oscillation pattern in the cumulative flamelet population. The numerical solutions will be constructed upon the experimental data, such that the numerical solutions with upper and lower limits appear to fit the experimental data.

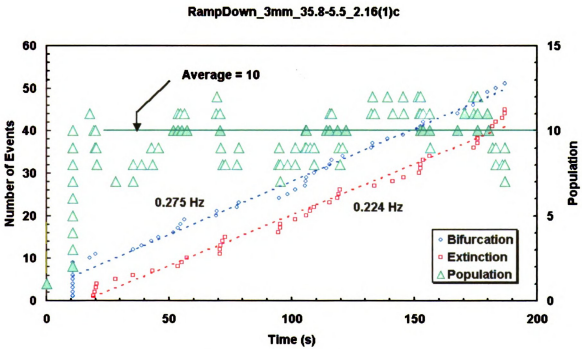

Figure 77. Population experimental data.

The experimental population data was generated in the .exl format, these data were transferred to the .m format and then plotted together with the numerical solution. One example of the combined plots can be found in Figure 78. As can be seen the numerical

solution data curve follows the curve of the experimental data. For the preliminary attempt to fit the numerical solution with the experimental data curve, Figure 78 shows a good result. The values of the parameters that improve the numerical solution to fit with the experimental data such as τ, ω, and ε, are 0.5, 1.5 and 1.7, respectively.

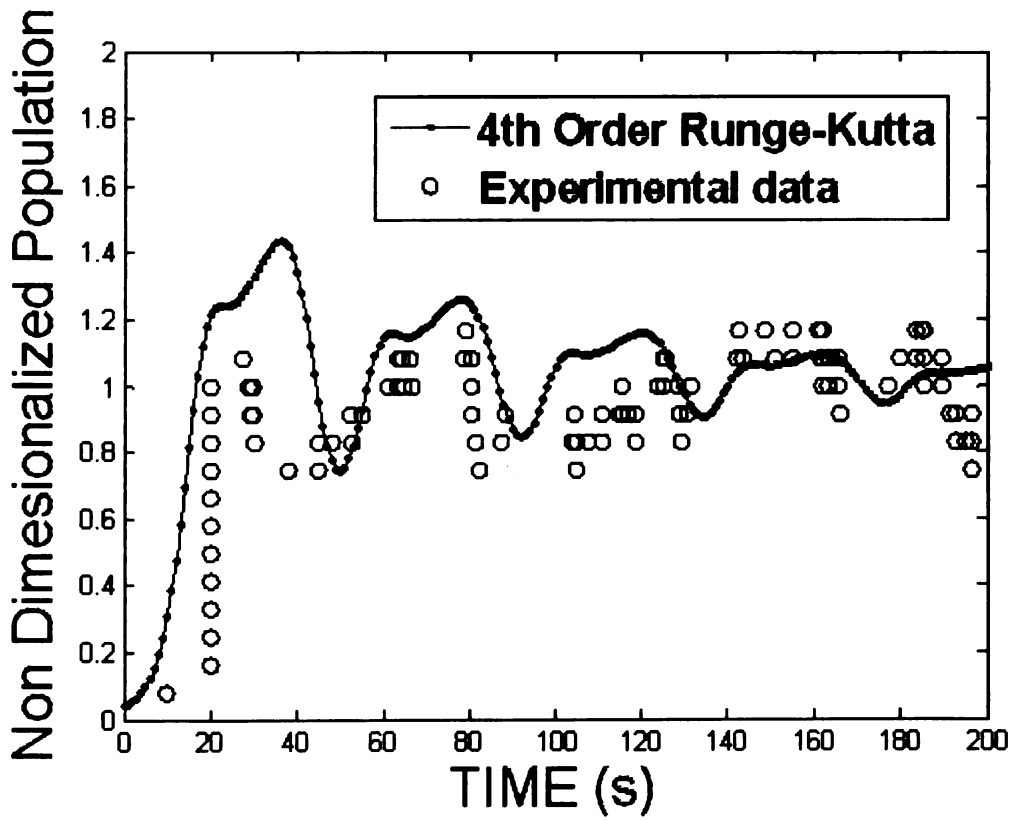

Figure 78. Experimental data with its numerical solutions.

7.8 Carrying Capacity and Time Lag

In this section the two parameters that affect the population model were studied by taking into account the physics of the flamelet. In [9], this study was done utilizing the results from the NASA microgravity facility. The results were compared with the results obtained from the MSU microgravity facility. The two parameters were carrying capacity, κ, and time lag, τ. Earlier in this chapter, the carrying capacity and time lag were estimated

to fit the population model with the experimental data. However, in this section the two parameters were studied further in terms of the oxygen supply, and flamelet lifetime for the carrying capacity, and time lag, respectively.

The carrying capacity, k, was defined in terms of the oxygen supply and the oxygen consumed per flamelet. Using the mass conservation equation, the oxygen mass flow rate was determined involving the inlet area, density at ambient temperature and the final air velocity. Whereas the mass flow rate of oxygen consumed per flamelet was determined using Equation (13) stated in Chapter 5. With these two properties, the carrying capacity can be expressed as:

$$\kappa = \frac{\dot{m}_{O_2}}{\dot{m}_{O_2 flamelet}}. \tag{31}$$

In Chapter 5, there were four ways to predict the oxygen consumption rate. However, only two of the equations gave reasonable results. These are Equations (6) and (7). Equations (8) and (9) on the other hand did not give reasonable results, therefore they were ignored. Since the results of Equation (7) always gave about the same with the results of Equation (6), therefore in the following Table 14 only the carrying capacity using the oxygen consumption rate of Equation (6) will be presented. Table 14 lists the average carrying capacity for various final air velocities for normal and inverted positions of the test facility with tunnel heights of 3, 4, and 5 mm

The values of the carrying capacity for the experiments in the normal position of the test facility are ranging from 8 to 19. This range is reasonable compared to the value of carrying capacity that was evaluated at NASA, which is 12. The values of the carrying

capacity in the inverted position, though, are arbitrary. There is a possibility that the gravitational effect plays a role in the inverted position experiments, therefore the methods to calculate oxygen consumption rate and the carrying capacity may not be accurate.

Table 14. Average carrying capacity

Position	Tunnel Height (mm)	Air Velocity (cm/s)	Carrying Capacity (κ)
Normal	3	2.5	13
		5.5	19
		10.0	12
	4	2.5	8
		3.0	11
		3.5	9
		4.0	11
		5.0	12
	5	2.5	10
Inverted	3	3.5	33
		4.5	33
		5.1	14
	4	2.5	16
		3.0	25
		3.5	14
	5	2.5	18
		3.5	1

The time lag, τ, was evaluated in terms of the flamelet lifetime, spread rate and the lateral angle of bifurcation. The time lag, τ, then can be expressed as in Equation (32). Here 2r is the flamelet diameter, V_f is the flamelet spread rate and γ is the lateral angle of bifurcation. The results that were presented earlier in this thesis such as the flamelet lateral

$$\tau = \frac{2 \cdot r}{V_f \cdot \tan(\gamma)} \tag{32}$$

bifurcation angle, flamelet spread rate and the flamelet diameter can be found in Chapters 4, 5 and 6, respectively. With these measurable properties, the time lag can be calculated

and the results can be found in Table 15, that shows the average time lag of experiments in the normal and inverted positions of the test facility for tunnel heights of 3, 4, and 5 mm with various final air velocities.

Table 15. Average time lag

Position	Tunnel Height (mm)	Air Velocity (cm/s)	Time Lag, τ, (s)
Normal	3	2.5	64
		5.5	83
		10.0	87
	4	2.5	56
		3.0	58
		3.5	71
		4.0	74
		5.0	49
	5	2.5	58
		3.5	29
Inverted	3	3.5	59
		4.5	77
		5.1	107
	4	2.5	77
		3.0	63
		3.5	65
	5	2.5	122
		3.5	80

The average time lag, for the experiments in the normal position is ranges from 29s to 87s. The average time lag generally increases as the final air velocity increases. However, the experiments in the inverted position show a reverse characteristic. Generally the time lag decreases as the final air velocity increases. The values are ranging from 59s to 122s. Compared to the results in [9], the time lag that was studied ranges from 24s to 37s for an experiment with 5 mm tunnel height in the normal position. The time lag values presented in Table 15 are about 2 to 3 times longer.

7.9 Intrinsic per Capita Growth Rate

The intrinsic per capita growth rate, r_o, for steady population growth with limiting resources (in this case oxygen) can be found by taking the difference between the bifurcation rate and the extinction rate divided by the total number of population [9]. For example, consider the bifurcation and extinction rates, and the average population of test t-40-25c, which values are 0.136 bifurcation/s and 0.124 extinction/s, and 10, respectively. The intrinsic per capita growth rate is then (0.136 bifurcation/s-0.124 extinction/s)÷10 flamelets = 0.00119/s. This small number (~0) suggests that when the population approaches steady state, the growth becomes slower because of the competition for the resources.

The intrinsic per capita growth rate, r_o, without limiting resources, can be determined based on the fractal number, flamelet spread rate, and the average flamelet lifetime [9]. The three properties were composed into the power law equation. Thus it can be expressed into Equation (33):

$$r_o \propto (f-1)\cdot\left(\frac{U_\infty \cdot V_f \cdot t_L}{2\cdot D}\right)^n . \tag{33}$$

In [9], the fractal numbers, f, were measured using the box-counting method and the values are typically 1.7 ± 0.1 for fingering patterns. For a uniform flame-front, the fractal number is 2, and for a no-branch fingering pattern, the fractal number is typically 1. The term $U_\infty/2D$ is the characteristic length scale of the diffusive gas-phase Stokes flow. The value of D is 1.6 cm^2/s. The exponent, n, of the power law relation is 0.6, which was obtained from the fingering smolder study.

CHAPTER 8
FLAMMABILITY MAP AND MODIFICATION TO THE APPARATUS

8.1 Flammability Map

The flammability map for the MSU microgravity facility (SMFT) was established by running numerous experiments with various test conditions. The results from the SMFT were combined with the results from NASA's microgravity facility. The following Figure 79 (was generated at NASA) shows the agreement between the two sources. Overall, the results from MSU and NASA agree well. In the middle of the plot, there are four data

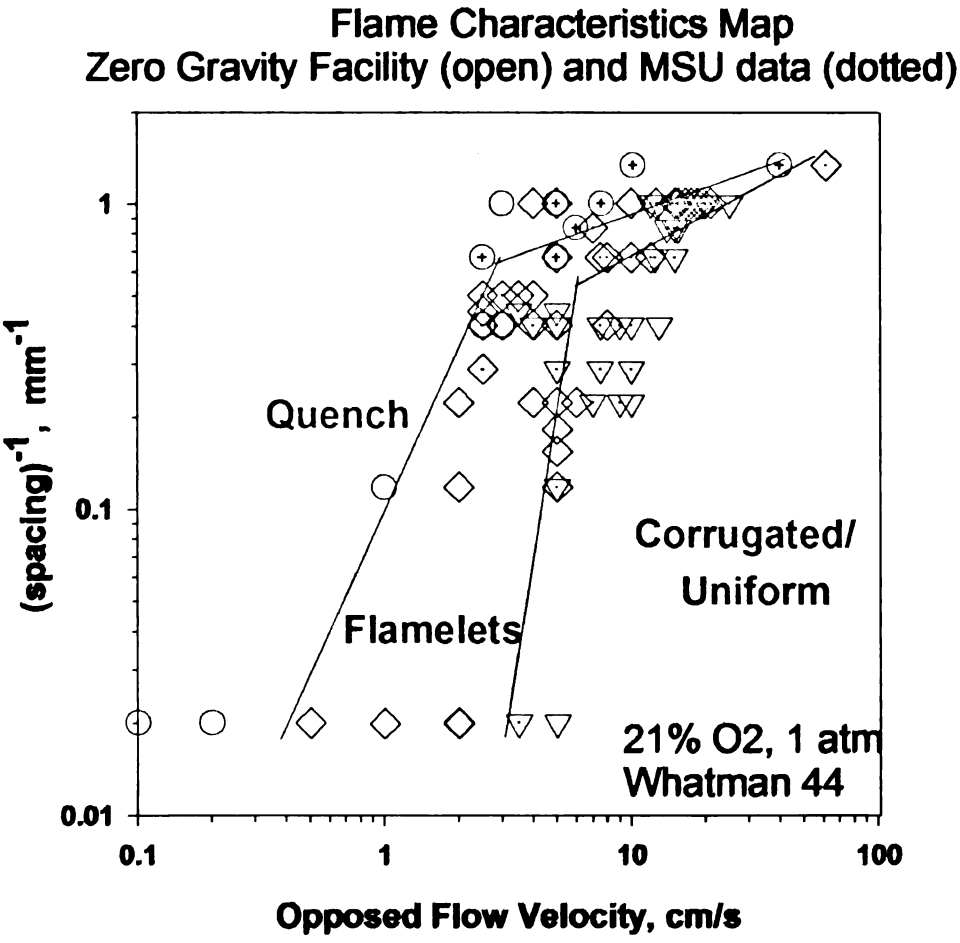

Figure 79. Flammability Map.

points (of the Corrugated/Uniform) that fall in the flamelet region. These peculiar data were carefully checked and a few more experiments were performed to ensure that they were not supposed to be in the flamelet region.

8.2 Modification on the SMFT

When burning sample paper, humidity is a factor that may have affects on the final results. To reduce this variable factor, NASA dries off the sample paper prior to the experiments. As a preliminary step to reduce this factor from the system, a dehumidifier was added into the airflow system. The dehumidifier was located after the filter before the pressure regulator. A diagram of the new airflow system can be found in Figure 80, and a picture of the dehumidifier can be found in Figure 81.

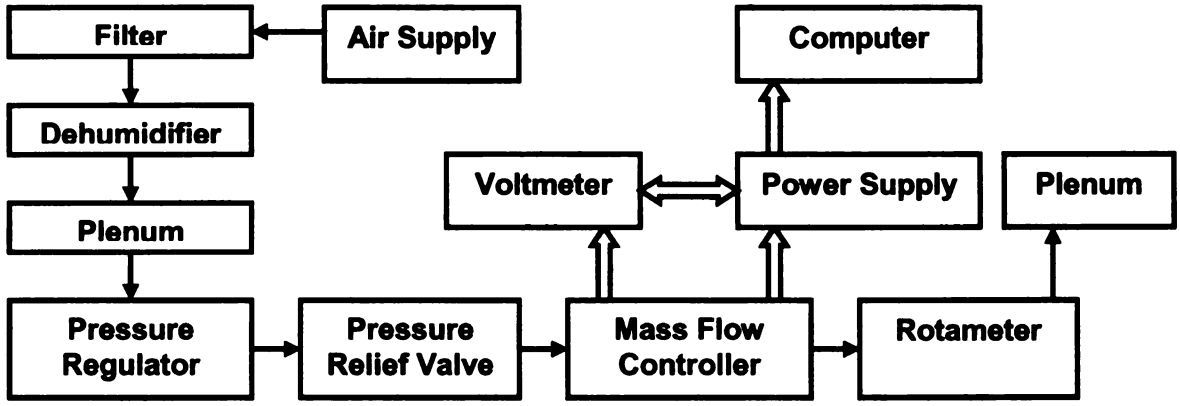

Figure 80. Diagram of the new airflow system with dehumidifier.

The dehumidifier has two filters on one side, and two desiccant tanks on the topside. When the pressurized wet air comes in from the filter to one of the tanks, the desiccant materials (consist of molecular sieve, alumina, and silica gel) in the tank absorbs the water vapor. Then some portion of the dry air flows through a purge orifice to the

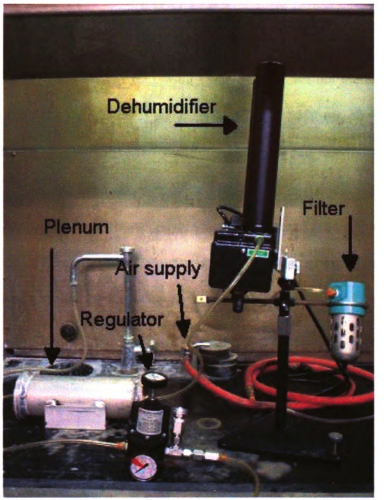

Figure 81. New airflow system with dehumidifier.

plenum, and the remaining portion flow to the other tank at near atmospheric pressure to reabsorb the water vapor and then exit to the atmosphere. After 30 seconds of one cycle, the first tank will regenerate itself. Then the pressurized wet air flows into the other tank. The second tank does the same process for 30 seconds then the wet air will flow back to the first cycle. The dry air that comes out of the tanks has pressure change caused by the different cycle. Therefore, to avoid unsteady pressure that goes into the test section tunnel a plenum is located after the dehumidifier before the pressure regulator.

CHAPTER 9
CONCLUSION AND FUTURE WORK

Overall this flamelet study went well. Most of the results studied in this thesis show similarity with the results studied at NASA. In addition, the results for the experiments in the normal and inverted positions are close but not the same. This can happen because of the different geometrical shape of the test section and the different conditions of the top and bottom plates. Also, this may happen because gravity plays a role in the behavior of the flamelets in the inverted position. When running an experiment, it can be visually observed that the flamelets in the inverted position are dimmer, weaker and always pulsing.

The flamelet population study using the experimental data from the MSU microgravity facility shows good agreement with the study that was performed at NASA. This study verifies that 50% ± 3% of the flamelet must be productive (mothers) for flamelet to reach steady state. In an evenly spaced experiment, flamelets propagate with a nearly constant rate. This corresponds with the 1:1 agreement between the bifurcation and the extinction rates. Between the results in the normal and inverted positions of the apparatus, the average cumulative number of flamelet population is higher when the apparatus is right side up than it is on the other side. The average cumulative number of flamelet population shows an increasing when there is more oxygen that flows into the system (i.e. by increasing the tunnel height or the air velocity).

The cumulative number of flamelet population shows an oscillating behavior. A first-order deferential equation was developed to simulate this oscillating behavior. The major factors that influence the equation in order to fit the experimental results are the

value of the time lag (τ), the initial condition, and the two perturbation features of ω and ε. Overall the preliminary step to study the flamelet population shows good progress and some of the factors studied show similar results with the study performed at NASA.

The results of the flamelet lateral angle of bifurcation study show that generally when the tunnel height increases the bifurcation angle also increases. The flamelet bifurcation angle of experiments in the normal position generally is higher than that in the inverted position.

With the help of TRACKER and SPOTLIGHT, the burned area measurement was done. The burned are study shows that when the apparatus is right side up, flamelets consumed about 40% to 70% of the fuel whereas when the apparatus is up side down, flamelet consumed about 20% to 50% of the fuel sample. The flame spread rate is proportional to the air velocity. The flamelet spread rate increases as the air velocity increases. This agrees with the results that were performed by NASA. The oxygen consumption rates were predicted and the results were used to calculate the global stoichiometric ratio. The global stoichiometric ratio shows that the combustion reaction for the burning cellulosic paper is fuel rich combustion.

For future work, it is desired for a longer as well as wider test section area for a larger sample paper for better statistical analysis. Therefore a modification to the apparatus is necessary. The current test section and the heat sink should be replaced with a more flat surface of test section and heat sink to obtain better experiments and fingering pattern.

In this thesis, the oxygen consumption rate was predicted. For more accurate oxygen consumption rate, it is desired to install a device that can capture the product gases and measure the oxygen level. Another study that can be done in the future is to measure

the sample surface temperature, and the development of the population analysis using the logistic model.

APPENDIX A

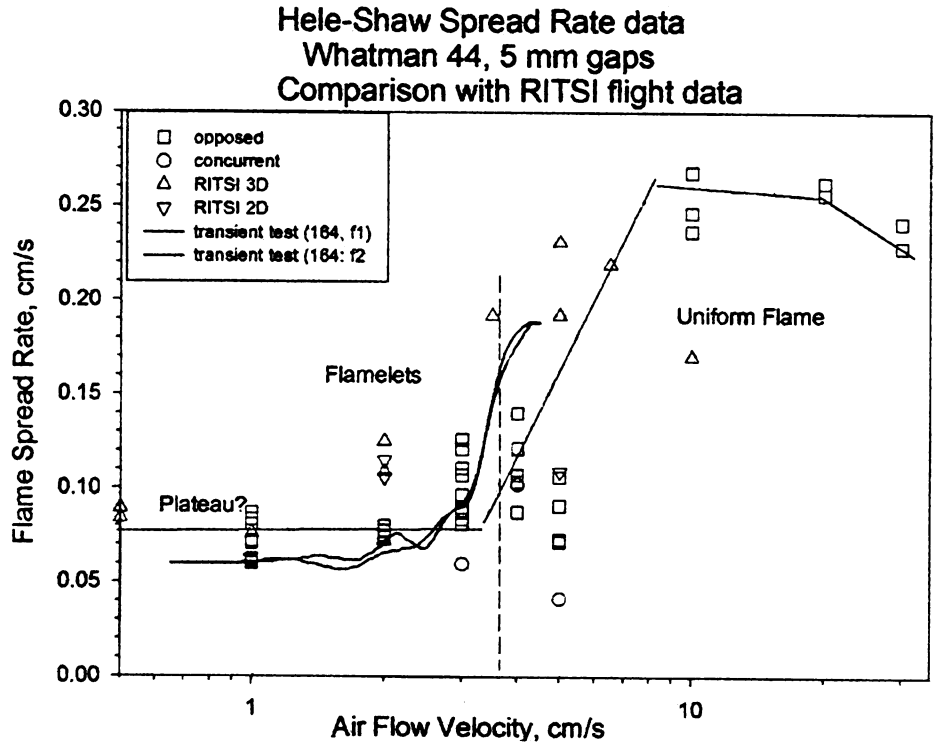

Figure A1. Flame spread rate [9].

From Equation (6):

$$\dot{O}_2 = \frac{dA}{dt} \cdot \rho_F \cdot 6 \cdot \frac{32}{162}$$

$$\frac{kg_{O_2}}{s} = \frac{m^2}{s} \cdot \frac{kg_F}{m^2} \cdot \#_{\cdot} \frac{\frac{kg_{O_2}}{kmol}}{\frac{kg_F}{kmol}}$$

From Equation (7):

$$\dot{O}_2 = \frac{\frac{dA}{dt} \cdot q_F \cdot \rho_F}{q_{O_2}}$$

$$\frac{kg_{O_2}}{s} = \frac{\frac{m^2}{s} \cdot \frac{kJ}{kg_F} \frac{kg_F}{m^2}}{\frac{kJ}{kg_{O_2}}}$$

From Equation (8):

$$\dot{O}_2 = \frac{\frac{dA}{dt} \cdot C_{PF} \cdot \rho_F \cdot (T_s - T_o)}{q_F} \cdot 6 \cdot \frac{32}{132}$$

$$\frac{kg_{O_2}}{s} = \frac{\frac{m^2}{s} \cdot \frac{kJ}{kg_F \cdot K} \frac{kg_F}{m^2} \cdot K}{\frac{kJ}{kg_F}} \#. \frac{\frac{kg_{O_2}}{kmol}}{\frac{kg_F}{kmol}}$$

From Equation (9):

$$\dot{O}_2 = \frac{\frac{dA}{dt} \cdot C_{PF} \cdot \rho_F \cdot (T_s - T_o)}{q_{O_2}}$$

$$\frac{kg_{O_2}}{s} = \frac{\frac{m^2}{s} \cdot \frac{kJ}{kg_F \cdot K} \frac{kg_F}{m^2} \cdot K}{\frac{kJ}{kg_{O_2}}}$$

From Equation (10):

$$\dot{O}_2 = \frac{\frac{dA}{dt} \cdot q_F \cdot \rho_F}{q_F} \cdot 6 \cdot \frac{32}{162}$$

$$\frac{kg_{O_2}}{s} = \frac{\frac{m^2}{s} \cdot \frac{kJ}{kg_F} \cdot \frac{kg_F}{m^2}}{\frac{kJ}{kg_F}} \cdot \#. \frac{\frac{kg_{O_2}}{kmol}}{\frac{kg_F}{kmol}}$$

APPENDIX B

```
clear
clc

%Inputs for all 3 methods:
lag=1.2;   %Time lag 'tau'
finalt=50;  %Final time

%=============================================================%

% EULER METHOD %

%Inputs for Euler Method:
delta=0.001;   %Increment time step.  When finalt/delta=# of data points
y(1)=1/10;  %Initial condition for population
ti(1)=0;     %Initial condition for time
k=1;         %Time counter for the equation
w=0;    %Frequency 'omega'
eps=0;    %Perturbation 'epsilon'

%Begin LINEAR loop
for t=[delta:delta:lag]; %Time interval for the linear loop
   y(k+1)=y(k)+(delta*((1+eps*sin(delta*w*(k+1)))*y(k)*(1-y(k)))); %The equation
   ti(k+1)=t; %Time counter
   k=k+1; %Data point counter
end %End of LINEAR loop

%This loop runs the non-linear part of the equation
%Also calculations for peaks, valleys and their corresponding time in the oscillation
p=1;       %Initial time counter for peak
v=1;       %Initial time counter for valley
c=1;       %Initial time counter for settling time 'ts'
ts=0;      %Initial condition for settling time
startts=0;  %Initial condition for a helper counter
period=0;   %Initial condition for period
ln(1)=0;    %Initial condition for log decrement
sumln=0;    %Initial condition for average log decrement

%Begin NON-LINEAR loop
for t=[lag+delta:delta:finalt]; %Time interval for the non-linear loop
   y(k+1)=y(k)+(delta*((1+eps*sin(delta*w*(k+1)))*y(k)*(1-y(k-lag/delta)))); %The
equation
   ti(k+1)=t; %Time counter
   k=k+1; %Data point counter
```

```
   %Begin SETTLING TIME loop
   if startts==1; %Counter
      if y(k)<(0.02*(peak(1)-1)+1); %Define settling time boundary 1.  Value after '>' sign
is variable
         if y(k-1)>(0.02*(peak(1)-1)+1); %Define settling time boundary 2.  Value after '>'
sign is variable
            tspossible(c)=k*delta; %All possible settling time value. Point at curve that
crosses with the boundary
            c=c+1; %Counter
         end
      end
   end %End of SETTLING TIME loop

   %Begin PEAK loop
   if y(k)<y(k-1); %Define peak boundary 1
      if y(k-1)>y(k-2); %Define peak boundary 2
         peak(p)=y(k-1); %Peak
         peakt(p)=(k-1); %Peak corresponding time
         startts=1; %Counter

         %Begin period, frequency, and log decrement loop calculations.
         if p>1; %Define a boundary
            period(p-1)=(peakt(p)-peakt(p-1))*delta; %Period
            freq(p-1)=1/period(p-1); %Frequency
            ln(p)=log(peak(p-1)/peak(p)); %Log decrement
            sumln=ln(p)+sumln; %Sum log decrement to calculate factor 'd' for damping
ratio
         end %End of period, frequency, and log decrement loop
         p=p+1; %Counter
      end
   end %End of PEAK loop

   %Begin VALLEY loop
   if y(k)>y(k-1); %Define valley boundary 1
      if y(k-1)<y(k-2); %Define valley boundary 2
         valley(v)=y(k-1); %Valley
         valleyt(v)=(k-1); %Valley corresponding time
         v=v+1; %Counter
      end
   end %End of VALLEY loop
end %End of NON-LINEAR loop

peak              %Display the value of peak
peakt=peakt*delta     %Display the corresponding peak time
valley            %Display the value of valley
valleyt=valleyt*delta  %Display the corresponding valley time
```

```
period              %Display all period values
freq                %Display the corresponding frequency of the period
ts=max(tspossible)     %Display settling time
tspossible          %Display all the time when the curve crosses the settling time (2%) line
ln                  %Display log decrement for all two consecutive peaks
d=(sumln/(p-1))        %Display the average value of factor 'd' in calculating the damping
ratio 'zeta'
zeta=d/(2*pi)          %Display damping ratio 'zeta'


%=============================================================%

% MODIFIED EULER METHOD %

%Inputs for Modified Euler Method:
delta2=0.001; %Increment time step.  When finalt/delta=# of data points
y2(1)=1/10;  %Initial condition for population
ti2(1)=0;    %Initial condition for time
k2=1;        %Time counter for the equation

%Begin LINEAR loop
for t2=[delta2:delta2:lag]; %Time interval for the linear loop
   n1=delta2*(y2(k2)*(1-y2(k2))); %Define first root of the equation
   n2=delta2*((y2(k2)*(1-y2(k2)))+n1); %Define second root of the equation
   y2(k2+1)=y2(k2)+(0.5*(n1+n2)); %The equation
   ti2(k2+1)=t2; %Time counter
   k2=k2+1; %Data point counter
end %End of LINEAR loop

%This loop runs the non-linear part of the equation
%Also calculations for peaks, valleys and their corresponding time in the oscillation
p2=1;        %Initial time counter for peak
v2=1;        %Initial time counter for valley
c2=1;        %Initial time counter for settling time 'ts'
ts2=0;       %Initial condition for settling time
startts2=0;  %Initial condition for a helper counter
period2=0;   %Initial condition for period
ln2(1)=0;    %Initial condition for log decrement
sumln2=0;    %Initial condition for average log decrement

%Begin NON-LINEAR loop
for t2=[lag+delta2:delta2:finalt]; %Time interval for the non-linear loop
   n1=delta2*(y2(k2)*(1-y2(k2-lag/delta2))); %Define first root of the equation
   n2=delta2*((y2(k2)*(1-y2(k2-lag/delta2)))+n1); %Define second root of the equation
   y2(k2+1)=y2(k2)+(0.5*(n1+n2)); %The equation
   ti2(k2+1)=t2; %Time counter
```

```
   k2=k2+1; %Data point counter

   %Begin SETTLING TIME loop
   if startts2==1; %Counter
      if y2(k2)<(0.02*(peak2(1)-1)+1); %Define settling time boundary 1.  Value after '>'
sign is variable
         if y2(k2-1)>(0.02*(peak2(1)-1)+1); %Define settling time boundary 2.  Value after
'>' sign is variable
            tspossible2(c2)=k2*delta2; %All possible settling time value. Point at curve that
crosses with the boundary
            c2=c2+1; %Counter
         end
      end
   end %End of SETTLING TIME loop

   %Begin PEAK loop
   if y2(k2)<y2(k2-1); %Define peak boundary 1
      if y2(k2-1)>y2(k2-2); %Define peak boundary 2
         peak2(p2)=y2(k2-1); %Peak
         peakt2(p2)=(k2-1); %Peak corresponding time
         startts2=1; %Counter

         %Begin period, frequency, and log decrement loop calculations
         if p2>1; %Define a boundary
            period2(p2-1)=(peakt2(p2)-peakt2(p2-1))*delta2; %Period
            freq2(p2-1)=1/period2(p2-1); %Frequency
            ln2(p2)=log(peak2(p2-1)/peak2(p2)); %Log decrement
            sumln2=ln2(p2)+sumln2; %Sum log decrement to calculate factor 'd' for
damping ratio
         end %End of period, frequency, and log decrement loop
         p2=p2+1; %Counter
      end
   end %End of PEAK loop

   %Begin VALLEY loop
   if y2(k2)>y2(k2-1); %Define valley boundary 1
      if y2(k2-1)<y2(k2-2); %Define valley boundary 2
         valley2(v2)=y2(k2-1); %Valley
         valleyt2(v2)=(k2-1); %Valley corresponding time
         v2=v2+1; %Counter
      end
   end %End of VALLEY loop
end %End of NON-LINEAR equation loop

peak2                %Display the value of peak
peakt2=peakt2*delta2     %Display the corresponding peak time
```

```
valley2                 %Display the value of valley
valleyt2=valleyt2*delta2    %Display the corresponding valley time
period2                 %Display all period values
freq2                   %Display the corresponding frequency of the period
ts2=max(tspossible2)        %Display settling time
tspossible2             %Display all the time when the curve crosses the settling time (2%)
line
ln2                     %Display log decrement for all two consecutive peaks
d2=(sumln2/(p2-1))          %Display the average value of factor 'd' in calculating the
damping ratio 'zeta'
zeta2=d2/(2*pi)             %Display damping ratio 'zeta'

%=============================================================%

% FOURTH ORDER RUNGE-KUTTA METHOD %

%Inputs for Fourth Order Runge-Kutta Method:
delta3=0.001; %Increment time step.  When finalt/delta=# of data points
y3(1)=1/10;  %Initial condition for population
ti3(1)=0;    %Initial condition for time
k3=1;        %Time counter for the equation
w3=0;        %Frequency 'omega'
eps3=0;      %Epsilon 'perturbation'

%Begin LINEAR loop
for t3=[delta3:delta3:lag]; %Time interval for the linear loop
  r1=delta3*(((1+eps3*sin(delta3*w3*(k3+1)))*y3(k3)*(1-y3(k3)))); %Define first root of
the equation
   r2=delta3*(((1+eps3*sin(delta3*w3*(k3+1)))*y3(k3)*(1-y3(k3)))+(0.5*r1)); %Define
second root of the equation
  r3=delta3*(((1+eps3*sin(delta3*w3*(k3+1)))*y3(k3)*(1-y3(k3)))+(0.5*r2)); %Define
third root of the equation
   r4=delta3*(((1+eps3*sin(delta3*w3*(k3+1)))*y3(k3)*(1-y3(k3)))+r3); %Define fourth
root of the equation
   y3(k3+1)=y3(k3)+(1/6*(r1+2*r2+2*r3+r4)); %The equation
   ti3(k3+1)=t3; %Time counter
   k3=k3+1; %Data point counter
end %End of LINEAR loop

%This loop runs the non-linear part of the equation
%Also calculations for peaks, valleys and their corresponding time in the oscillation
p3=1;        %Initial time counter for peak
v3=1;        %Initial time counter for valley
c3=1;        %Initial time counter for settling time 'ts'
ts3=0;       %Initial condition for settling time
startts3=0;  %Initial condition for a helper counter
```

```
period3=0;  %Initial condition for period
ln3(1)=0;   %Initial condition for log decrement
sumln3=0;   %Initial condition for average log decrement

%Begin NON-LINEAR loop
for t3=[lag+delta3:delta3:finalt]; %Time interval for the non-linear loop
  r1=delta3*((1+eps3*sin(delta3*w3*(k3+1)))*y3(k3)*(1-y3(k3-lag3/delta3))); %Define
first root of the equation
  r2=delta3*(((1+eps3*sin(delta3*w3*(k3+1)))*y3(k3)*(1-y3(k3-lag3/delta3)))+(0.5*r1));
%Define second root of the equation
  r3=delta3*(((1+eps3*sin(delta3*w3*(k3+1)))*y3(k3)*(1-y3(k3-lag3/delta3)))+(0.5*r2));
%Define third root of the equation
  r4=delta3*(((1+eps3*sin(delta3*w3*(k3+1)))*y3(k3)*(1-y3(k3-lag3/delta3)))+r3);
%Define fourth root of the equation
  y3(k3+1)=y3(k3)+(1/6*(r1+2*r2+2*r3+r4)); %The equation
  ti3(k3+1)=t3; %Time counter
  k3=k3+1; %Data point counter

  %Begin SETTLING TIME loop
  if startts3==1; %Counter
    if y3(k3)<(0.02*(peak3(1)-1)+1); %Define settling time boundary 1.  Value after '>'
sign is variable
      if y3(k3-1)>(0.02*(peak3(1)-1)+1); %Define settling time boundary 2.  Value after
'>' sign is variable
        tspossible3(c3)=k3*delta3; %All possible settling time value. Point at curve that
crosses with the boundary
        c3=c3+1; %Counter
      end
    end
  end %End of SETTLING TIME loop

  %Begin PEAK loop
  if y3(k3)<y3(k3-1); %Define peak boundary 1
    if y3(k3-1)>y3(k3-2); %Define peak boundary 2
      peak3(p3)=y3(k3-1); %Peak
      peakt3(p3)=(k3-1); %Peak corresponding time
      startts3=1; %Counter

      %Begin period, frequency, and log decrement loop calculations
      if p3>1; %Define a boundary
        period3(p3-1)=(peakt3(p3)-peakt3(p3-1))*delta3; %Period
        freq3(p3-1)=1/period3(p3-1); %Frequency
        ln3(p3)=log(peak3(p3-1)/peak3(p3)); %Log decrement
        sumln3=ln3(p3)+sumln3; %Sum log decrement to calculate factor 'd' for
damping ratio
      end %End of period, frequency, and log decrement loop
```

```
        p3=p3+1; %Counter
      end
   end %End of PEAK loop

   %Begin VALLEY loop
   if y3(k3)>y3(k3-1); %Define valley boundary 1
      if y3(k3-1)<y3(k3-2); %Define valley boundary 2
         valley3(v3)=y3(k3-1); %Valley
         valleyt3(v3)=(k3-1); %Valley corresponding time
         v3=v3+1; %Counter
      end
   end %End of VALLEY loop
end

peak3                  %Display the value of peak
peakt3=peakt3*delta3       %Display the corresponding peak time
valley3                %Display the value of valley
valleyt3=valleyt3*delta3   %Display the corresponding valley time
period3                %Display all period values
freq3                  %Display the corresponding frequency of the period
ts3=max(tspossible3)       %Display settling time
tspossible3            %Display all the time when the curve crosses the settling time (2%)
line
ln3                    %Display log decrement for all two consecutive peaks
d3=(sumln3/(p3-1))         %Display the average value of factor 'd' in calculating the
damping ratio 'zeta'
zeta3=d3/(2*pi)            %Display damping ratio 'zeta'

%=============================================================%

% ERROR CALCULATION %

%note: y(k)--Euler, y2(k2)--Modified Euler, y3(k3)--4th Runge-Kutta

errorsum=0; %Counter
for j=[1:k2-1]; %Interval
   pterror=(y(j)-y2(j))^2; %Squared term
   errorsum=errorsum+pterror; %Norm error, summation term
end
error=errorsum^0.5 %Error between euler and modified euler

errorsum2=0; %Counter
for j2=[1:k3-1]; %Interval
   pterror2=(y2(j2)-y3(j2))^2; %Squared term
   errorsum2=errorsum2+pterror2; %Norm error, summation term
end
```

```
error2=errorsum2^0.5 %Error between modified euler and 4th RK

errorsum3=0; %Counter
for j3=[1:k3-1]; %Interval
   pterror3=(y(j3)-y3(j3))^2; %Squared term
   errorsum3=errorsum3+pterror3; %Norm error, summation term
end
error3=errorsum3^0.5 %Error between euler and 4th RK

%==========================================================%

% PLOTTING and DOWNLOAD EXCEL EXPERIMENTAL DATA %

t4=[0:finalt];
y4=1.02;

hold on
subplot(2,1,2); plot(ti,y,'b+',ti2,y2,'ro',ti3,y3,'g.',t4,y4,'.-k') %Graph
xlabel('TIME (S)','fontsize',18)
ylabel('Non-Dimensional Population','fontsize',18) %Plot and axes' labels
axis([0 20 0 1.7]) %Axis range
legend('Euler','Modified Euler','4 RungeKutta') %Show legend
```

BIBLIOGRAPHY

1. Ball, P., 1999, "The Self-Made Tapestry: Pattern Formation in Nature," Oxford University Press.

2. Greenberg, Michael D., 1998, "Advanced Engineering Mathematics," Second ed., Prentice Hall Inc., New Jersey.

3. O'Keefe Controls Co. Form OK-253.

4. Olson, Sandra L., Ferkul P., and T'ien, J.S., 1988, "Near-Limit Flame Spread Over a This Solid Fuel in Microgravity," *Twenty-Second Symposium (International) on Combustion*/The Combustion Institute, pp. 1213-1222.

5. Olson, Sandra L., 1991, "Mechanisms of Microgravity Flame Spread Over a Thin Solid Fuel: Oxygen and Opposed Flow Effects," *Combustion Science and Technology*, Vol. 76, pp. 233-249.

6. Olson, Sandra L., T'ien J.S., 2000, "Buoyant Low Stretch Diffusion Flames Beneath Cylindrical PMMA Samples," *Combustion and Flame*, Vol. 121, pp. 439-452.

7. Olson, Sandra L., Kashiwagi, T., Fujita, O., Kikuchi, M., Ito, K., 2001, "Experimental Observations of Spot Radiative Ignition and Subsequent Three-Dimensional Flame Spread Over Thin Cellulose Fuels," *Combustion and Flame*, Vol. 125, pp. 852-864.

8. Olson, Sandra L, April 2005, "Sub-Critical Rayleigh Number ($<Ra_c$) Apparatus for Materials Flammability Screening," draft.

9. Olson, Sandra L., Miller, F.J., and Wichman, I.S., 2005, "Characterizing Fingering Flamelets Using the Logistic Model," draft.

10. Oravecz, Lisa M., 2001, "Instabilities of Spreading Diffusion Flames in Microgravity and the Design and Construction of a Hele-Shaw Apparatus that Produces Flames in the Near Extinction Limit Regime Under Simulated Low Gravity Conditions," M.S. Thesis, Michigan State University.

11. Palm, William J. III, 2001, "Introduction to MATLAB 6 for Engineers," First ed., McGraw-Hill Higher Education, New York.

12. Tanaya, Stefanus A., 2004, "Examination of a Simulated Micro-Gravity Device for Evaluating Flame Instability Transitions and Flame Spread Over Thins Cellulosic Fuels," M.S. Thesis, Michigan State University.

13. Turns, Stephen R, 2000, "An Introduction to Combustion Concepts and Applications", 2nd edition, McGraw-Hill.

14. Wichman, I.S., 1992, "Theory of Opposed-Flow Flame Spread," *Prog. Energy Combustion Science*, Vol. 18, pp.553-593.

15. Wichman, I.S., 2003, "Notes on Theory of Flamelet Formation," Department of Mechanical Engineering, Michigan State University, draft.